5-2001

Examination of gas transport through polysiloxane open cell foams: effects of compression upon model flow, permeation parameters, and cell morphology

Rosanne Anderson Smith
University of Tennessee

To the Graduate Council:

I am submitting herewith a dissertation written by Rosanne Anderson Smith entitled "Examination of gas transport through polysiloxane open cell foams: effects of compression upon model flow, permeation parameters, and cell morphology." I have examined the final electronic copy of this dissertation for form and content and recommend that it be accepted in partial fulfillment of the requirements for the degree of Doctor of Philosophy, with a major in Polymer Engineering.

Paul J. Philips, Major Professor

We have read this dissertation and recommend its acceptance:

Roberto S. Benson, Mark Dadmun, Kevin M. Kit

Accepted for the Council:

Carolyn R. Hodges

Vice Provost and Dean of the Graduate School

(Original signatures are on file with official student records.)

To the Graduate Council:

I am submitting herewith a dissertation written by Rosanne A. Smith entitled "Examination of Gas Transport Through Polysiloxane Open Cell Foams: Effects of Compression Upon Model Flow, Permeation Parameters, and Cell Morphology." I have examined the final copy of this dissertation for form and content and recommend that it be accepted in partial fulfillment of the requirements for the degree of Doctor of Philosophy, with a major in Polymer Engineering.

Paul J. Phillips, Major Professor

We have read this dissertation
and recommend its acceptance:

Roberto S. Benson

Mark Dadmun

Kevin M. Kit

Accepted for the Council:

Interim Vice Provost and
Dean of The Graduate School

EXAMINATION OF GAS TRANSPORT THROUGH POLYSILOXANE OPEN CELL FOAMS: EFFECTS OF COMPRESSION UPON MODEL FLOW, PERMEATION PARAMETERS, AND CELL MORPHOLOGY

A Dissertation

Presented for the Doctor of Philosophy Degree

University of Tennessee, Knoxville

Rosanne Anderson Smith

May 2001

DEDICATION

This work is dedicated to my parents, Barbara and Fred Anderson,

my siblings Ruth, David, and Kristin,

my children, Jared and Corey, and

especially to my husband James.

It is also dedicated to the many

relatives and ancestors

of the

Anderson, Spearman, and Smith families.

ACKNOWLEDGMENTS

I wish to thank the members of my family, for their understanding and patience with my perpetual status as a student! To James Smith, Jared Smith, and Corey Smith: thank you forever for your love, support, and trust. I love you.

To Dr. John Leckey of Y-12 and Dr. John Kirkpatrick of the Oak Ridge National Laboratory, a huge thank you for initiating this project, and your confidence in me. I acknowledge the Technology Development Division staff at the Y-12 Complex for their research direction, equipment, and facilities, and financial support from the Department of Energy (Contract #DE-AC05-00R22800). I also thank the many Y-12 managers who supported and encouraged my doctoral work: Jeff Bostock, Bill Thompson, Dave Beck, Fred Jones, Dr. John Koger, and Charlene Edwards, to name only a few.

I express gratitude and appreciation to my University of Tennessee advisor, Dr. Paul Phillips, and my committee members Dr. Roberto Benson, Dr. Kevin Kit, and Dr. Mark Dadmun. To fellow graduate students in the Materials Science and Engineering Department, and office staff Carla Lawrence and Sandra Maples, thank you for making this experience fun as well as educational.

To my talented sisters Rebecca Jackson, Gloria Mencer, Rosa Thomas, and the Oak Ridge Alumnae of Delta Sigma Theta Sorority, Inc., your friendship can never be replaced.

ABSTRACT

A study to test a model for gas flow through a polymer foam system was conducted. The goal was to quantitatively relate polymer foam compression and gas pressure drop across the specimen, to the gas flow through the foam. Foam cell morphology was studied to assess adequacy of the model to accommodate material characteristics.

X-ray tomographic images were collected for polydimethylsiloxane (PDMS) foam material under various levels of compression. The intent was to implement a systematic analysis method of correlating some aspect of these images to the cell morphology in order to enhance understanding of the material characteristics. It was shown that x-ray tomography is a useful nondestructive method for understanding the compressive behavior of a mechanically loaded polymer foam. As a general trend, the experimentally obtained x-ray attenuation coefficient could be correlated with the effective density of the polymer foam, approaching values for the polymer resin as foam compression increased. Mechanical properties of the cellular polymer could also be elucidated.

Experimental data was collected for several gas flow rates in the free molecular flow regime, for foam compressions ranging from 0 to 40%. For each experiment, data for temperature, incoming pressure (p_{in}), and pressure drop (Δp) were compiled and used to calculate foam permeability. Permeability demonstrated a linear dependence on the gas flow rate, but an exponential dependence upon the degree of compression.

Logarithmic plots of steady-state pressure drop, Δp, and time required to reach steady-state, t_{ss}, provided more information about gas flow through the foam. Regression analysis was used to predict flow behavior at higher compressions.

A model correction must be included for the percolation behavior displayed by the foam material under study, since flow is occluded at a compression of 33% (0.22 porosity). This decrease in flow at a critical porosity is a disruption of the original model equations, which did not allow for the critical percolation threshold. Additionally, a term that characterizes permeation through the solid polymer can describe flow behavior at compressions where open cell flow paths are blocked.

TABLE OF CONTENTS

LIST OF FIGURES

LIST OF TABLES

1. INTRODUCTION

A study was conducted that was designed to test a model for gas flow through a polymer foam system. The goal was to quantitatively relate polymer foam compression, and gas pressure difference to the gas flow through the foam. The model was compared to others developed for characterization of permeation through nonfoam polymers and general foam constructs. Foam cell morphology was studied in order to assess adequacy of the model with respect to structural features.

1.1 Overview

Gas moves transversely through a polymer foam sheet, at a relatively high incoming pressure, such as 1 atm (equivalent to 760 Torr or 1.01×10^5 Pa) or a very low pressure, down to 10^{-5} atm (.0076 Torr or 1.01 Pa). The foam, an open-cell polydimethylsiloxane (PDMS) containing silica filler, is in varying states of uniform compression which will effectively reduce its porosity. A mathematical characterization of gas transport as a function of pressure and foam porosity has been devised by Kirkpatrick. This model characterizes the mechanisms for gas transport as they vary with thermodynamic conditions [39]. The purpose of the project was to experimentally replicate this range of states in order to a) test the validity of the mathematical model, b) determine values of the variable/constant **k**, the permeation constant for the material at various levels of

porosity and gas pressure, and c) determine the values for porosity and pressure at which gas transport mechanisms change flow regime.

These flow regimes comprise two types of gas transport which were to be modeled in this study:

- ***laminar viscous flow***, or high gas pressure through polymer foam
- ***free molecular flow***, or low gas pressure through polymer foam

Diffusion or low gas pressure flow through polymer foam which is filled with static gas is yet another regime and was not a part of this project.

The polymer foam was characterized as a standard cellular solid in order to understand its structure under compression. A method of visualizing the cell morphology was used to ascertain foam characteristics, and changes therein as the compression occurs. Two-dimensional x-ray images as applied to the field of stereology were used to quantify features of the polymer foam, and these were correlated to assumptions used for the gas transport model. Images from polymer cells at various stages of compression provided features that correlated void structure changes to the gas transport data. As well, these images were applied to standard foam characterization practices as defined in the literature.

1.2 Methodology

There has long been an interest in the movement of small molecules through polymer systems, as the many uses of plastics, for food storage, separation membranes, medical devices, and other applications became apparent. Polymers are essentially employed as gas and liquid barriers, making the solubility, diffusivity, and permeability of small molecules through polymeric structures topics of high interest.

A method of visualizing the polymer cell morphology was used to ascertain void volume and shape changes at various compression levels; these findings and data were applied to assumptions used for the model.

Gas Transport Methodology: PDMS foam material is used in industrial applications and has a cellular structure. Many studies are on-going to fully understand the means of transverse gas transport through the material, particularly when the foam is compressed. This project used two circular plates to control compression of a sheet of PDMS foam, such that the degree of compression could be determined with great precision. Standard leaks were used to flow a known volume of gas (and mass flow rate) at some pressure between plates, in the molecular flow regime; a gas tank and flow controller were to be used for the pressures required for laminar viscous flow. Measurements were taken of the upstream gas pressure and the pressure differential ($\Delta p = p_{in} - p_{out}$), as a function of time and compression, as the gas moved through the polymer matrix. Variables were pressure of the upstream, or incoming test gas (p_{in}); pressure drop (Δp) temperature (T); input flow

volume (mass) and rate (dm/dt); porosity of the uncompressed foam (n_o); porosity of the compressed foam (n_1); and tortuosity (T).

The model also relates **k**, the material permeability, to Γ (also known as P), the chemical or noncellular polymer permeability, for the regimes cited above. The values of **k** derived from Γ were compared to those calculated from the above model, in an effort to reconcile the macroscopic and the microscopic assumptions. One hypothesis is that the value **k** should approach that of the solid polymer as the foam is compressed, causing a reduced void volume.

Transition Considerations: This project encompassed a wide ranging scale of sizes. When one considers the gas pressure of 760 Torr (1 atmosphere) down to .0076 Torr, one must consider macroscopic flow properties on the high pressure end, and molecule-wall collision properties on the other.

The material characteristics ranged broadly as well, with 0.50 - 0.70 mm diameter voids serving as a flow channel in the uncompressed foam, versus the much smaller-sized voids resulting from high compressions. One might also consider microscopic voids and intermolecular free volumes, which provide the siloxane resin with high permeability, even in its resin form. For comparison purpose, a typical foam void volume is of the order of

$1.6x10^{-12}$ m^3, versus the traditional polymeric free volume, which is considered "large" in siloxane elastomers at room temperature (150 $Å^3$, or $1.5x10^{-28}$ m^3) [79].

Of interest in this research was the determination of where the transition between macroscopic and microscopic lies – at what compression level does cellular PDMS approximate its constitutive resin? At what incipient gas pressure do molecule-polymer interactions overcome the flow dynamics? A goal was to determine the transition points for both foam compression and gas pressure, where the gas transport mechanism changes from laminar viscous flow to free molecular flow.

Foam Visualization Methodology: X-ray energy is often used to discern crystalline structure using the diffractive properties of the polymeric motif. However, this can also be applied to amorphous materials, which scatter x-rays according to the electron density of its atomic constituents. Each element has a characteristic x-ray attenuation coefficient μ/ρ, which is dependent upon the x-ray (photon) energy, the atomic mass unit and the cross-section for interaction with a photon, such that the mass attenuation for a mixture of i elements can be determined by:

$$\frac{\mu}{\rho} = \sum_i w_i \left(\mu/\rho\right)_i \qquad (1.1$$

and w_i denotes the weight fraction of i component [34].

The intensity of scattered rays can be detected and measured by tomography, which enables the x-ray impingement to be rotated about the specimen. In this manner, scattered intensity as a function of location can be used to form a reconstructed "image" of the specimen at various planes through the sample for a three-dimensional characterization.

Tomographic scans were compiled for this porous polysiloxane material at several compressive levels, and images through the sample thickness were used to ascertain the void volume changes and uniformity of such from uniaxial compression. This data provided insight to tortuosity assumptions used in the model presented for gas flow characteristics. It was found that a greater resolution must be achieved, in order to characterize the siloxane foam structure and cell shape as is typical for cellular materials. Structural details include cell shape, symmetry, cell edge thickness, cell face thickness, edge and face connectivity, and principal cell dimensions, and are further described by Gibson, et.al. [30].

2. BACKGROUND AND LITERATURE REVIEW

Diffusion of substances through polymeric materials has long been of interest in various fields. Cellular polymers which serve as insulation have heat transport properties arising from the gas which moves through the pores. The medical industry conducts thousands of studies to ensure that medications embedded in polymeric membranes are transmitted to the patient in a timely manner, and that polymers for contact lens allow oxygen to permeate to the human eye. Polymer membranes are put to use as selective filters, keeping some molecules out and allowing other in. Mass use of soft drink bottles (wherein polyethylene terephthalate retains liquid and CO_2 gas) and low-density polyethylene food wrap (an O_2 barrier) are constant reminders that polymers serve a multitude of flow-related functions with each application. Polymers serve as o-rings, seals, and gaskets, again emphasizing knowledge of diffusion characteristics and the mechanisms wherein small molecules are absorbed and move through a macromolecular system. A simple concept of diffusion terms it "...a process which leads to an equalization of concentration within a single phase" [35].

The selected model for this study [39] assumes a gas flow through an open-cell polymer foam in a manner that depends upon the foam compression and pressure drop, Δp, the difference between the incoming and outgoing gas pressures.

Because permeability is the combination of 1) absorption of a molecule onto the polymer, 2) diffusion of the molecule through the host material due to a concentration or pressure gradient, and 3) elimination of the molecule from the system, there are numerous mechanisms which can thermodynamically influence any of these steps. In the present research, all assumptions and experiments were under isothermal room temperature conditions, thereby eliminating at least one variable.

The project presented here was one to experimentally verify a mathematical model for gas flow and determine values for permeability, **k**, of a system comprising polydimethylsiloxane foam of 0.615 g/cm^3 nominal density with a single inert gas flowing through. This polymeric foam was placed into a compressive state during use, which is typical for foam products, hence data was also be taken to verify assumptions concerning the compression dependent portions of the model.

A cellular polymer has properties arising from the foam cell structure, which in turn come from the gas content and the polymer material itself. Polydimethylsiloxane is an amorphous, or non-crystalline polymer at room temperature. The concept of there being a structure in an amorphous polymer holds interest; this "species" is described as a "bowl of entangled spaghetti," where each spaghetti strand is an extra-long or macromolecule. Structure is imposed due to with nuclei and surrounding electronic structure, along with interactions with neighboring chains and small molecules which happen to venture into the three-dimensional maze. This amorphous structure features "free volume," or space

between the molecular strands, the amount of which dictates how much rotational, vibrational, and translational motion can be undergone by the interacting molecules. The structure of the molecule (stiff or flexible), the temperature of the system, and the number of small molecule interlopers all play a part in the degree of movement. Thus this structure renders the physical properties which are of the most immediate concern to any user of the polymer and of the polymer foam. Physical properties of amorphous polymers are closely tied to the glass transition temperature, T_g, a temperature at which all molecular motion ceases. The T_g is a material property that defines where and when the material can be put to use.

The microscopic properties of the cellular polymer are based upon the polymer matrix itself; the macroscopic foam structure plays a major role in its mechanical behavior. In part, this project explored "transition" conditions during which the foam moves from its cellular nature to that of the polymer molecule itself: at what level of compression did "free volume holes" become more important than foam void cells because the cellular volume had so diminished in size? Or, at what inlet gas pressure did gas molecule-wall-collisions overcome the laminar flow mechanism for the mode of diffusion?

2.1 Poly(dimethylsiloxane) (PDMS) Properties

The amorphous polymer poly(dimethyl siloxane) or PDMS, in this study contains a finely divided fumed silicon dioxide filler. The PDMS is foamed by means of a leachable urea filler, into a 0.040 inch (0.10 cm) thickness open-cell foam of nominal density 0.615

g/cm^3 [44, 74]. This foam is used while under static compression. PDMS has a set of two crystalline melting points at T_{m1} of -43 °C (230K) and T_{m2} of -37 °C (236K), a glass transition temperature T_g of -123°C (150K) and a crystallization temperature T_c of -50°C (223K). All experiments in this study were carried out at an ambient temperature of approximately 27 °C (300K) where PDMS is in an amorphous, rubbery state [42].

Polydimethyl siloxanes (PDMS), $[-Si(CH_3)_2O-]_n$ are substituted siloxane chains, with the formula:

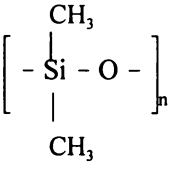

Methyl groups are small, but even where R substitution groups are bulky, the siloxane chain remains more flexible than many hydrocarbon chains. This dynamic flexibility arises from the relatively long Si - O bond length, 1.64Å (vs. the C - C bond, 1.53Å), which reduces steric interference and "intramolecular congestion." Additionally, the oxygen atoms cannot be substituted while in the chain, and the Si - O - Si bond angle is approximately 143 degrees, much wider than the tetrahedral bond angle of 110 degrees seen in most organic polymers [21]. The polysiloxane chains have little or no intermolecular interaction, easily sliding past one another, remaining liquid unless lightly crosslinked. The PDMS in this experiment has a small vinyl content which serves to provide crosslinking sites. The presence of the oxygen atoms has an attractive, rather than repulsive effect upon substituent R groups that may become conformationally near

the chain (as in the pentane effect in carbon chains) [29]. All of these factors cause siloxane chains to have increased dynamic and equilibrium flexibility, with a very low glass transition temperature ($T_g \approx$ -123°C) and low melting temperature. The quantity T - T_g is known as a predictor of mechanical properties, with the polymer remaining rubbery above the and glassy below it. Silicones maintain their properties over a wide temperature range, making them useful polymers in broad applications.

PDMS resin is highly permeable to gases and vapors, and has a permeability coefficient for hydrogen gas, **P**, of 348 x 10^{-13} (cm^3 at STP) cm/cm^2 s Pa), as compared to 31 x 10^{-13} for polypropylene and 7.4 x 10^{-13} for polyethylene [59]. Another material property of interest is **D**, the diffusion coefficient, where the amount of diffusant moving through the material per unit time is called flux, J_x:

$$J_x = -D\,(\delta c/\delta t) \qquad (2.1$$

and $(\delta c/\delta t)$ is the concentration gradient. Diffusion in amorphous polymers can be visualized as small bodies making their way through the spaces between entwined chains. There needs to be a space of distance h for unimpeded diffusion; changes in h will affect the kinetics involved [52]. A certain amount of energy was needed to distort the molecule and make space for the diffusing molecule to pass; this activation energy, E_d, has been compared to the γ-relaxation of certain types of polymer chains, the molecular mechanism causing creep and stress relaxation. The energetics of diffusion and permeation are

temperature-dependent Arrhenius type relationships where $P = P_o e^{(-Ep/RT)}$ and $E_{permeation} = E_{diffusion} + E_{solution}$. $E_{solution}$ is actually the thermodynamic quantity H_s, the heat of solution [59]. The activation energy is that needed for polymer chains to move sufficiently that a space large enough to accommodate a gas molecule is formed [75]. This kinetic energy is dependent upon the type of polymer structural units and the gas cross-section.

2.1.1 Fumed Silicon Dioxide Filler

Improved strength, obtained by limiting or reducing the molecular mobility of the siloxane chain, is realized by blending in of filler particulates. In the present case, this filler also serves to retain water, which is thought to have structural functionality for this material. Filled polydimethylsiloxane can be thought of as a composite which comprises a polymer phase and a fumed silica inorganic phase.

Fillers are fine particulates which alter an elastomer's properties; they increase the elastic modulus as well as the tensile strength by increasing the energy required to tear the elastomer apart. Similar to the view of polymer solution theory where the excluded volume of random coil polymers acts as a hydrodynamic sphere, the filler particle is surrounded by an elastic medium (the solvent) which has a modulus (viscosity) which is altered according to the volume fraction of filler, v_f. The Young's Modulus is then $E = E_o (1 + 2.5\ v_f + 14.1\ v_f^2)$ where E_o is the modulus with no filler present [28]. This equation assumes that the filler particles are spherical and that Hooke's Law is in effect over the range of elongation. Therefore, the equation for stress can be used:

$$\sigma = \sigma_o (1 + 2.5\ v_f + 14.1\ v_f^2). \quad (2.2$$

These equations do not consider the additional strength rendered if there is chemical bonding between the polysiloxane matrix and the filler particles, which well known to occur in the PDMS-silica system [1, 2, 12, 79]. The particle size now becomes a consideration and a very small diameter particulate (≈ 250Å) becomes optimal, due to the increased surface area in contact with the polymer. The Cab-o-Sil particles constituting the major filler constituent (25.6 wt% of the PDMS in this study) have particle diameters of between 200 - 300Å [14].

This filler mechanism has been compared to crosslinking in that the chains now have fixed points or junctions and segments with limited mobility. This is also similar to crystalline polymers, wherein the regular lattice structures are regions where molecular movement is inhibited. When interfacial bonding is taken into account, the equation for modulus becomes, where f is a shape factor for the particle [68]:

$$E = E_o (1 + 0.67f\ v_f + 1.62\ f^2 v_f^2). \quad (2.3$$

Struik [73] observed that the adherence of polymer chains to the filler particle surface limits its segmental mobility, thereby altering its properties. He asserts that the chains away from the particles will behave like an unfilled rubber; this is an "undisturbed region", while the "disturbed region" will show a broadened and higher glass transition temperature range. Therefore, one would expect the material under study to reach a T_g (and therefore, begin the aging process) at a higher temperature than the typical PDMS.

This is not the case for this polymer, which has a T_g independent of filler content and molar mass crosslinks [21], although the transition peak of the filled polymer is substantially broadened [3].

Another potential impact of filler content within the PDMS is its effect upon permeability to gases. Nielsen [57] discusses the filler particle as a blockage around which gas molecules must flow, and the fact that the filler is not permeable. This latter point brings about a volume fraction dependency where ϕ_P represents the volume fraction of polymer. The new diffusion path is described by the tortuosity factor, which is

$$\tau = \frac{\text{distance a molecule must travel}}{\text{thickness of material}} \qquad (2.4$$

In a polydimethylsiloxane polymer, silica filler particles also have the effect of crosslinks, as the PDMS actually attaches to the SiO_2; this decreases the flexibility of the chain, thereby reducing diffusivity [13]. It remains to be determined how the tortuosity of the path encountered by a gas particle around the silica cross-link compares to the tortuosity of the open-celled path modeled by Kirkpatrick (Section 2.2.2). This path is described as a bundle of tubes which turn and curve, thereby hindering the gas particle flow. The microscopic tortuosity is seemingly a separate entity which would be unaffected by the foam compression.

2.1.2 Void Volume and Free Volume in PDMS

For clarification, it should be noted that the void volume is due to the macropores that are in the less-than-millimeter size range. This volume is due to the open cells residing in the foam, and is distinctly different from any microscopic voids, or polymer free volume, the space between macromolecules. The size scale of the latter is in the angstroms (10^{-10} m). Because polydimethylsiloxane at room temperature is an elastomer far above its T_g, an effort was made to estimate the amount of free volume using group contributions to volume. This semi-empirical method assumes that the molecular units (groups) comprising a macromolecule have additive properties. When applied to molar volume, calculation for PDMS resulted in 71 cm^3/mol at room temperature, as compared to the measured volume of 62 cm^3/mol. This was explored, and experimental data utilized for the foam as its cells were compressed. It should be noted that Pethrick's theoretical volume includes a term R = 25 cm^3/mol for "residual volume" [60].

2.2 Gas Transport Models

A compelling motivation for interest in the permeation properties of a polymer is that the movement of small probe molecules provides much information about the molecular structure of the polymer. As previously discussed, permeation requires successive physical processes. First, the permeant must be adsorbed into the polymer at some location or "hole"; secondly, the permeant must jump from one hole to another. The presence of these holes in a polymer comprises the free volume, or intermolecular spaces in the macromolecular structures. A rubbery polymer such as polydimethylsiloxane has

free volume predicated by molecular chain size, flexibility, and chemistry. The last aspect controls interactions which may occur between the diffusing species and the polymer itself. There is also a thermodynamic dependency upon temperature and pressure which inherently dictates the polymer morphology and hence, whether the diffusant has sufficient energy to overcome the barrier to movement from location to another [71].

System features that define gas transport properties in a polymer also define behavior in physical relaxation phenomena (movement of polymer chains as a function of time or stress) and dielectric relaxation - movement of dipoles. As stated by Rogers, "the processes of mass and momentum transport in polymers have mutual dependence on the presence of void and defect structures and on the nature of polymer chain segmental motions" [64]. We find the same story in structure as it influences the T_m and T_g.

Just as chain flexibility has been correlated to the T_g by way of the free volume, past studies have correlated elements of translation and rotational energy to diffusion constants. For example, studies of saturated vs. unsaturated polymers demonstrate that the unsaturation improves polymer chain ease of rotation, and hence provides larger volumes through which diffusants can move [4].

The extensive chain flexibility of PDMS is such that the presence of methyl side groups does not have the effect found by van Amerongen in his study of elastomers. In his

determination of the diffusivity of N_2 and O_2 through polybutadiene, polyisoprene, and poly-2,3-dimethylbutadiene, the value of D was 1.1 x 10^{-6}, 0.94x10^{-6}, and 0.30x10^{-6} cm^2/s, respectively. Not surprisingly, the glass transition of these three structures is -80 °C, -72 °C, and -33 °C, respectively [76].

In other words, only at much lower temperatures is movement restricted in an unsaturated polymer that has no methyl side groups. There is perhaps an improved diffusivity because of the local rigidity at the site of double bonds, which decreases packing at that site [4]. Similarly, the PDMS chain flexibility is so substantial, despite cross-linking and filler influences, its free volume causes a minimal energy of activation for diffusant movement as described by the D for diffusivity of N_2 and O_2 through PDMS (with 10% filler): 8.5 x 10^{-6} cm^2/s and 12.0 x 10^{-6} cm^2/s, respectively [59].

2.2.1 Theorems of Polymer Permeation and Diffusion

The basic and general rule of diffusion, which is the movement of one material through another, is the relationship derived by Einstein for the frictional drag on a moving particle: $D = kT/f$, where k is Boltzmann's constant, T is the temperature, and f is the frictional force per unit velocity on the diffusant [4]. This provides a starting point for theorems and models explaining why certain types of matter pass through others, and especially the rate of this movement. Due to the nature of the research described herein, this section will focus on the diffusion of gas particles through a polymeric medium, thereby excluding work related to permeation through polymers of hydrocarbon

molecules and fluids. By definition, this indicates a diffusivity D that is constant and independent of concentration effects, and thereby assumes the applicability of Fick's Law.

2.2.1.1 Fick's Law

Fick's Law broadly applies to diffusion across a medium, and is described by the equation discussed before:

$$J = -D\frac{dc}{dx}, \tag{2.5}$$

where x is distance through a medium, D is a diffusivity constant and c is the concentration of the diffusing species, which varies in a concentration gradient throughout the medium. J is the diffusion flux through the medium.

Fick's second law describes the change in concentration with time:

$$\frac{dc}{dt} = D\left(\frac{d^2c}{dx^2} + \frac{d^2c}{dy^2} + \frac{d^2c}{dz^2}\right). \tag{2.6}$$

However, the design of the current work was concerned only with unidirectional flow, so Eqn 2.6 above will simplify to:

$$\frac{\partial c}{\partial t} = D\frac{\partial^2 c}{\partial x^2} \tag{2.7}$$

This equation makes it apparent that a plot of concentration vs. distance can render a great deal of information about the concentration at a particular point in time, and state whether the concentration is increasing or decreasing at the certain part of the curve. As time proceeds, the diffusion reaches a steady state at which $\delta c/\delta t$ goes to zero [23].

Where the diffusivity constant D is dependent upon c, Fick's second law becomes:

$$\frac{\partial c}{\partial t} = \frac{\partial D(c)(\partial c / \partial x)}{\partial x}. \qquad (2.8$$

However, in the case of permanent gases at low pressures (less than 1 atmosphere), D is independent of concentration, time, and distance.

Once steady-state has been reached, J becomes constant and Eqn 2.5 can be described as:

$$J = -D\frac{c_1 - c_0}{l}, \qquad (2.9$$

where l is the total material thickness and c_1 and c_0 are the concentrations of permeant at the high and low sides of the specimen, respectively [19].

2.2.1.2 Henry's Law

In an open-cell foam, the diffusive properties are dominated by Henry's Law, which states that the concentration of gas in the polymer is directly dependent upon the partial pressure of the gas:

$$c = Sp, \qquad (2.10$$

where S is the solubility of gas molecules in the solid, p is the partial pressure, and c, the concentration. Since permeation, P, comprises the two steps of absorption or dissolving of the gas in the polymer (S), the diffusion of the solved particles (D), the following equation applies:

$$P = DS. \qquad (2.11$$

In the open cell foam, there is relatively little interaction between the gas and the polymer molecules, and the permeation is relative to flow properties of the gas. However, as the foam is compressed or as the pressure of the incoming gas is lessened, polymer structure becomes more central to diffusion and the permeation constant. This is a situation where the permeant gas molecules experience influence from wall collisions, increasing the importance of gas-material interaction considerations.

The mean free path is defined as the average distance traversed by a molecule between collisions. The gas pressure can be low enough that "...the mean free path becomes comparable with the dimension of the containing vessel (and) the flow properties of the gas become markedly different" [24]. Herein lies the crux of this research problem, to vary the gas pressure or alter the containing vessel dimensions (or both) in order to determine where the flow properties change.

In the case of extremely high foam compression or very low gas pressure, we can examine the diffusion expressions derived for the solid PDMS polymer, which itself is highly porous due to the flexible chain structure, as earlier noted in Section 2.1. In fact, at room temperature, the activation energy for a H_2 molecule diffusing through PDMS (with 10% filler) is 9.3 kJ/mol, much lower than H_2 through polybutadiene (21.3 kJ/mol), polyvinylchloride (34.5 kJ/mol), or polyvinylacetate (21.6 kJ/mol) [59].

Silicone rubber is generally 10 - 20 times as permeable to gases as carbon-based polymers [45]. As an elastomer at room temperature, PDMS falls into the category of polymer which containing a large fraction hole free volume. For this reason, one should expect that diffusion coefficients of the solid PDMS polymer would not be a strong function of pressure [27].

2.2.1.3 Daynes Model

Daynes [25] designed experiments to determine permeability through rubber and established permeation through a rubber membrane as two separate processes, absorption and diffusion, where:

$$J = DS\frac{p_1 - p_0}{\ell}, \qquad (2.12$$

with J the flux, or quantity of gas passing through membrane of thickness ℓ per unit time; D is the diffusion coefficient of the gas in the polymer, S is the absorption (or solubility)

coefficient, and $p_1 - p_0$ is the pressure drop from one side of the membrane to the other. This is the essence of later work in the area of diffusion and permeability.

The relationship above allows measurement of the permeability P through a membrane of area A and thickness ℓ according to Fick's Law at a steady state:

$$P = \frac{J\ell}{A\Delta p}. \qquad (2.13$$

Daynes then derives an expression for the time it takes to reach steady state flow, and plots time vs. gas concentration. The slope of the straight line, which is steady-state flux J, is interpolated to the x-axis. The distance from zero is described as the time lag λ, where:

$$D = \frac{\ell^2}{6\lambda}. \qquad (2.14$$

Therefore the diffusion coefficient and the absorption coefficient can both be determined by conducting a flow experiment measuring pressures and time.

Rogers [64] presents diffusion theory in more common terms used today, which were nevertheless derived from the work of Daynes and others. This reference uses the following variables:

J - permeation rate; diffusion flow; flux, or penetrant passing through unit time

Q - total amount of permeant which has passed through area A during time t

$$J = Q/At. \quad (2.15$$

The rate of change of J is proportional to the rate of change of the pressure or concentration with time: $\delta J/\delta x = \delta c/\delta t$ across a thickness ℓ of material. At steady state, J is constant, since $\delta c/\delta t$ is zero. J is also proportional to the concentration gradient and the diffusion constant D, according to Fick's Law: $J = -D(\delta c/\delta x)$. Since D is a constant, integration again gives the relationship: $J = D(c_1 - c_2)/\ell$ with the equilibrium concentrations proportional to gas pressures by the solubility constant S, where $c = Sp$. The solubility coefficient is described by Henry's Law such that S is indeed constant, so we have $J = DS\frac{(p_1 - p_2)}{\ell}$ and consequently, DS can be described as the permeation constant P , or permeability where:

$$P = \frac{\Delta Q/\Delta t}{A(p_1 - p_2)}. \quad (2.16$$

Data for solubility, diffusivity, and permeation constants for hydrogen and nitrogen gases through a rubbery PDMS solid is given in Table 2.1[1] [59].

Solubility constant data for gases through silicone rubber is also given by Van Krevelen [78] for a temperature of 298K in units of $10^{-5}cm^3$ (STP)/cm^3-Pa; for N_2 gas, S is 0.081

[1]All tables can be found in Appendix B.

and for H_2, S is 0.047. D, the diffusivity, is given for H_2 through silicone rubber (7.5×10^{-5} cm^2/s) and for N_2, the diffusivity is 1.5×10^{-5} cm^2/s.

2.2.1.4 Knudsen's Law

As a gas flows through a constricted passage, or capillary, it demonstrates Poiseuille flow, meaning that there is a static layer of gas molecules along the wall of the capillary, with a velocity gradient maximized at the center. The viscous drag between layers produces what is called Stokesian diffusion [72]. As gas pressure is reduced such that its mean free path is greater than the capillary, gas viscosity is less important as the gas particles collide with walls, a diffusion type called Knudsen flow [18]. However, this type flow is sometimes considered intermediate between laminar viscous flow and molecular flow, hence it is sometimes called transition flow [56].

Flow is controlled by molecular motions and the probability that molecules will hit and pass through holes:

$$F = wn\sqrt{\frac{8k_BT}{\pi m}}, \qquad (2.17$$

where w is a probability factor, n is the number of molecules per volume, m is the molecular mass, k_B is Boltzmann's constant, and the square root term is equivalent to v, the molecular speed [49]. Knudsen's constant, the value of which delineates flow type, will be discussed later in this paper with regard to experimental results and flow regime.

2.2.1.5 Langmuir Mode

The Langmuir Theory for surface adsorption dictates a greater affiinity between diffusant molecules and the polymer at low pressures. At higher pressures, absorption sites become saturated, causing S, the solubility coefficient to be reduced [64]. This is more likely to occur in filled PDMS with a polar molecule, such as water, absorbing onto silica filler sites. Neutral gases like H_2 and N_2 should tend toward Henry's Law behavior, or a constant value of S over the entire pressure range up to the 1 atm (760 Torr) maximum. It is noted that permanent gases such as hydrogen and nitrogen lack strong interactions with polymers, have small solubilities, and demonstrate ideal behavior. However, Langmuir behavior will be kept in mind, since certain gases can still absorb onto non-wetted silica filler sites; it is still unlikely that this will occur at the low pressures being considered in this study [64].

2.2.1.6 Dual-Mode Sorption Model

The dual-mode sorption model is generally applied to glassy polymers, and classifies the gas absorbed into two populations. One type is present within the polymer and free to diffuse as normally described. The other population comprises gas molecules trapped within preexisting closed voids as the polymer temperature had been reduced below the T_g. Both sets of gas molecules must be in equilibrium with the other [27]. This model would not seem to apply in the case of an elastomeric PDMS, which is at room temperature, far above its T_g. However, the idea of two gas types is one to be considered with regard to comparisons of the macroscopic open cells of 0.70 mm diameter size range

versus the microscopic closed cells observed to reside in the polymer matrix (see Figure 2.1, the optical micrograph[2]).

2.2.1.7 Darcy's Law

Darcy's Law states that the flow rate is proportional to the pressure gradient [18], similar to Poiseuille's Law for laminar liquid flow. This model is a classic study of liquid flow through a porous media. Where Q is the volume flow per second across cross-sectional area A, and h_1 - h_2 the pressure drop across a filter of length L,

$$Q = \mathrm{K} A \frac{h_1 - h_2}{L}, \qquad (2.18$$

with K a proportionality constant called the hydraulic conductivity [8]. Flow-through-porous-media models equate the material to a solid with parallel tubes embedded. Flow equations are then designed for these thin capillary-like tubes. This approximation has found broad applications in describing flow through geological formations, catalyst beds, biological systems, and foam materials.

2.2.1.7 Flow Through Polymer Foam

A polymer can be conceptualized as a heterogeneous material, and flow through such materials is modeled by Barrer [6]. Where a solid amorphous polymer is filled with inorganic particles, the shape of the particles is considered. In the case of PDMS filled

---

[2]All figures can be found in Appendix A.

with fumed silica, Raleigh adapted Maxwell's equations for electrical conduction through a dilute suspension of spherical particles, where ε is the mean dielectric permeability:

$$\left(\frac{\varepsilon}{\varepsilon_B} - 1\right) = 3v_A\left[\frac{\varepsilon_A + 2\varepsilon_B}{\varepsilon_A - \varepsilon_B} - v_A + \frac{\alpha(\varepsilon_A - \varepsilon_B)v_A^{10/3}}{\varepsilon_A + \left(4\varepsilon_B/3\right)} + \ldots\right]^{-1} . \qquad (2.18$$

and ε_B and ε_A the permeabilities of the matrix phase and dispersed phase, respectively. Similarly, we can describe Phase A as voids dispersed in Phase B (polymer), with the void shape approximated as spherical. The model described by Equation 2.18 assumes that the dispersion comprises identical spheres distributed in a cubic lattice, with the coefficient α assuming different values for simple, face-centered, and body-centered cubic geometries [6]. The Maxwell model is also usefully applied to the concept of percolation.

2.2.2 Kirkpatrick Model

For the purposes of this model, the cellular polymer material is considered to be a "porous medium domain" and a number of assumptions must be made about an extremely complex material for the purpose of simplification [9]. Flow through a porous system involves state variables that are a function of both time and space. Bear describes a set of requirements for the systematic development of a conceptual model.

i Boundary configuration and conditions

ii Initial conditions

iii Dimensions of the problem (1-D, 2-D, or 3-D)

iv Materials involved and their relevant properties

v Temperature of the system

vi Material interfaces

vii Processes occurring within the boundary

viii State variables for these processes.

The driving motivation for this study was to amass a set of measurements which both calibrate the model and determine the value of specific parameters. It was also desirable to use data from the polymer phase of the system to improve upon the accuracy of the model by correcting and fine-tuning the materials-related assumptions.

This specifically applied to the experimental results as were compared to model results. Ideally, the cellular polymer characterization would have produced a set of coefficients which could then be integrated into the mathematical model. The result would be a decrease in the uncertainty of the conceptual model described in the following sections. This description is organized from a conceptual standpoint as outlined by Bear. The reader is referred to the original work of Kirkpatrick [39] for the derivation of the constitutive relationships; however, assumptions are explained in detail.

Material Assumptions: The foam is assumed to behave as a set of cylinders bundled together in a tube of radius r_t, where there are N_t tubes located in an area of height h and width w (see Figure 2.2). The tubes have the length $L/\sqrt{T}$ where T is the tortuosity factor tau, frequently used to describe the "tortuous" path a flow must take to divert itself around various obstructions in its path. Just as described by Eqn. 2.4 for diffusive flow around filler particles, obstructions include crystalline areas or even copolymer blocks in a polymer. In the current case, the tubular flow through random pores in the medium will not be in a straight line. The value of T is assumed to be independent of pore size or shape, and therefore independent of permeability [18]. For the purpose of the current study, tau is given the value 0.67 and symbolized with a capital greek T to distinguish it from temperature T, which is usually paired with R (as in RT) in this model [39].

2.2.2.1 Free Molecular Flow Regime

Free molecular flow is described as the state where the mean free path of the gas molecules is larger than the hole diameter of flow. In this case there is more likelihood that molecules will collide with matrix material walls than into other gas molecules, thus eliminating the term for gas viscosity from consideration. Flow in this regime is independent of gas pressure.

2.2.2.1.1 Uncompressed Foam

The cellular polydimethylsiloxane sheet is considered "uncompressed foam" in its unloaded state. The cells are modeled as interconnected spherical voids through which

gas flows in a direction parallel to the sheet thickness. The permeability of the foam was experimentally determined by measurement of gas flow changes through the sheet specimen. In general, the mass flow dm/dt is a function of the gas pressure. For purposes of the current work, closed solution equations are now given for the case of radial flow outward through a disk-shaped specimen.

2.2.2.1.2 Foam Under Compression

Disk: The effective permeability k_{1free} for compressed foam of effective porosity n_1 in this regime is described by:

$$k_{1free} = k_0 \left[\frac{n_1}{n_0}\right]^3 \left[\frac{1 - n_0}{1 - n_1}\right]^2, \qquad (2.19$$

where k_o is the permeability of the foam in an uncompressed state with original porosity n_0 and the compressed porosity n_1. The effective diffusivity D_{keff} is given by the following equation:

$$D_{keff} = \frac{16}{3}\sqrt{\frac{k_{1free} n_1 \mathcal{T} RT}{\pi}}. \qquad (2.20$$

The mass flow at extremely low pressures can be written, for a disk-shaped specimen, as:

$$\left(dm/dt\right) \ln\frac{r_{in}}{r_{out}} = \frac{2\pi h}{RT} D_{keff}(p_{in} - p_{out}) \ln\left(\frac{r_{out}}{r_{out}}\right). \qquad (2.21$$

D_{keff} is plotted in Figures 2.3 and 2.4 using equation 2.21 with small and large pressure drops assumed, respectively (see Appendix A). This theoretical model includes actual specimen radii and a mass flow rate of 3.9E-5 cm^3/s. The permeability model is shown for free molecular flow and various foam compressions in Figures 2.5 and 2.6.

2.2.2.2 Laminar Viscous Flow Regime

The regime of continuum, or laminar viscous flow is similar to that of a fluid, in that the gas particles will interact with one another to a much greater degree than cell walls. The particles, or gas molecules, have mean free paths that are small as compared to the void diameter.

2.2.2.2.1 Uncompressed Foam

The gas viscosity, μ, is now a consideration in the flow behavior, and it is determined that:

$$\left(\frac{dm/dt}{area}\right)_{viscous_{n=n0}} = -\frac{N_t}{2RT}\frac{1}{hw}\frac{r_t^4}{8\mu}\frac{\partial P^2}{L}\sqrt{T}, \qquad (2.22$$

where expressions for N_t, the number of tubes per unit area and r_t, the tube radius, are

$$\frac{N_t}{hw} = \frac{n_0^2 T^{3/2}}{8\pi k_0} \text{ and } r_t = \sqrt{\frac{8k_0}{n_0 T}}. \qquad (2.23$$

2.2.2.2.2 Foam Under Compression

Mass flow dependencies on the square of the pressure drop as well as porosities are expressed by:

$$\left(\frac{dm/dt}{area}\right)_{viscous_{n=n_1}} = -\frac{\partial P^2}{2RT}\frac{k_0}{\mu L}\left[\frac{n_1}{n_0}\right]^4\left[\frac{1-n_0}{1-n_1}\right]^3. \qquad (2.24$$

Again, considering the specific radial flow outward from a disk, the mass flow dm/dt can be expressed as:

$$dm/dt = \frac{2\pi \bar{\rho} hk}{\mu}(p_{in} - p_{out})\ln\frac{r_{out}}{r_{in}} \quad . \qquad (2.25$$

The permeability according to Eqn. 2.25, is plotted in Figure 2.9, demonstrating flow behavior in the laminar viscous flow regime.

2.2.2.3 General Expression for Disk Under Compression

A straightforward expression for total mass flow will cover the entire pressure range of interest, and covers the sum of the mass flow equations for each regime:

$$\dot{m} = \frac{2\pi h k_o \Delta p p_{avg}}{\mu \ln\left(r_{in}/r_{out}\right)RT}\left(\frac{n_0}{n_1}\right)^4\left(\frac{1-n_1}{1-n_0}\right)^3 + \frac{16}{3}\sqrt{\frac{k_o n_1 T}{\pi RT}}\frac{\pi h \Delta p}{\ln\left(r_{in}/r_{out}\right)}\left(\frac{n_0}{n_1}\right)^{3/2}\left(\frac{1-n_1}{1-n_0}\right) \qquad (2.26$$

Total Flow = Laminar Viscous Flow (LVF) + Free Molecular Flow (FMF).

From the relationships shown here, it is apparent that at high pressures, the mass flow is dominated by the LVF portion, while at small pressures, the FMF portion is larger. Similarly, as compression is increased, the laminar viscous flow portion of the equation gains significance. Transition between regimes can be stated to occur when the two portions of the total flow equation are set equal to one another, or when LVF = FMF. Rearranging the terms of such an equation makes it possible to solve for values of porosity, n_1 or average pressure, p_{avg} at the regime transition point. Rearranging the terms of such an equation makes it possible to solve for values of porosity, n_1 or average pressure, p_{avg} at the regime transition point. These expressions are independent of specimen size and Δp:

$$p_{avg} = \frac{8\mu}{3}\sqrt{\frac{n_1 T R T_1}{k\pi}}\left(\frac{n_o}{n_1}\right)^{2.5}\left(\frac{1-n_1}{1-n_o}\right)^2, \qquad (2.27$$

and

$$n_1 = \frac{\left\{\frac{8\mu}{3p_{avg}}\sqrt{\frac{TRT}{k\pi}}\left(\frac{n_o^{1.25}}{(1-n_o)^2}\right)\right\}^{1/2}}{1+\left\{\frac{8\mu}{3p_{avg}}\sqrt{\frac{TRT}{k\pi}}\left(\frac{n_o^{1.25}}{(1-n_o)^2}\right)\right\}^{1/2}}. \qquad (2.28$$

It should be noted that this model assumes that the diffusivity, solubility, and permeability of permanent gases in the polymer matrix are orders of magnitude smaller than the flows being considered.

2.2.3 Permeability

The permeability, k, in the Kirkpatrick model has an equivalence to the "chemical" permeability as established for polymer membranes and other materials. To convert k (units of m^2) to the traditional permeability, P, which has the units of Barrers (10^{-10} cm^3(STP)-cm/cm^2-sec-cmHg), the following are provided for free molecular flow and laminar viscous flow, respectively:

$$P_{fmf} = \sqrt{nTk_{1free}/(1.0283\text{x}10^{-11})TM} \qquad (2.29$$

$$P_{lvf} = \frac{k_{lvf} p_{avg}}{\mu T(2.782\text{x}10^{-5})} \qquad (2.30$$

Permeation data given in this paper will generally be reported in Barrers for comparison with literature values for polysiloxanes.

2.2.4 Percolation

In addition to the focus on a transition between flow regimes, we might also be concerned with a percolation transition. In the "bundle of tubes" model, flow is governed by tubes that are continuous across the assumed flow path. At smaller compressions and

maximum porosity, the data confirm an available pathway for gas flow. The steady-state pressure drop obtained experimentally for compressions of 0 to 30% can be used in the model flow equations, to calculate an ever-decreased permeability coefficient, k. Indeed, this number approaches the value for solid resin permeability, P. At 35% compression, flow is so reduced as to cause p_{in} and Δp to increase to even higher values. Prior to a transition between free molecular and laminar viscous flows, we can consider a transition through percolation.

Sax and Ottino describe polymer blend morphology as a combination of geometrical and topological factors [67]. While the open cell descriptions have described geometry, there is still the topological aspect, which dictates connectedness. Transport, or percolation can only occur if the void volume in the cellular PDMS remains interconnected throughout the volume. As compression is increased, the foam cells collapse in upon each other, thereby isolating the remaining void spaces from others. While most polymer permeation studies consider flow in the normal direction through a thin membrane, the current study involves transverse flow through a distance of material. When the existing void spaces are no longer interconnected, apparently between 30 and 35% compression, flow can no longer take place. In fact, this "critical percolation" value is well known to occur at 32% accessible volume in some systems [67]. In others, it is known to occur at a 20% void fraction. This critical value is dependent upon the coordination number, which describes the interconnectedness of the cells.

2.3 Cellular Foam

The material under study is a polymeric foam of nominal density of 0.615 g/cm^3, formed using a poly(dimethylsiloxane) or silicone polymer filled with finely divided fumed silicon dioxide. This material was foamed by peroxide and urea, then washed with water to remove the urea. Also called a cellular plastic, the polymer foam comprises of a mass of fine gas bubbles (gas phase) dispersed in a solid plastic phase (matrix) and is classified as an open-cell foam. These PDMS foams are soft and flexible, and are used for their cushioning properties [17]. The silica filler substantially enhances the mechanical strength of the siloxane polymer, as previously discussed in some detail.

The structure of foams can be likened to a network of struts, which each bear a compressive load, causing a bending response. This provides the linear elastic properties, which can be predicted and modeled, based upon assumptions concerning:

- length and breadth of the strut
- material of which strut is composed
- ratio of material contained in the struts versus the vertices

An understanding of the cellular structure brings about an understanding of mechanical behavior, and possibly the capability to predict such.

2.3.1 Characterization of Cellular Materials

The cell geometry affects the responses of the foam when in use under compressive loads, and as the gas moves through it. A knowledge of foam variables, which include density,

porosity, cell geometry, and gas phase composition, enable one to model the material and its properties. It also brings the gas transport model some values for variables which in fact are materials properties: diffusivity and permeation constant.

There are numerous possibilities for visualization and subsequent characterization of macroscopic polymer foam cells.

2.3.1.1 Imaging Models

As far back as the 1800s, scientists have made efforts to extrapolate three-dimensional information from their two-dimensional vision. According to Kampf [37], Delesse, Rosiwal, and Glagoleff put forth models for estimating the volume of a dispersed phase, by determining the area of that phase within a specimen cross-section. They estimate that the volume will be directly proportional to the measured area, as shown in Eqn 2.31.

$$\frac{F_i}{F} = \frac{L_i}{L} = \frac{V_i}{V} = \frac{P_i}{P}, \qquad (2.31$$

where $\mathbf{V_i}$, $\mathbf{F_i}$, $\mathbf{L_i}$ and $\mathbf{P_i}$ are the volume fraction, the component fraction, the length fraction, and the fraction of intersection points on a grid, respectively, of component i within a total volume **V**, two-dimensional length **L**, and overall points **P**. Figure 2.7 is an example of this concept with cross-sectional lengths of the void phase (or any heterogeneous phase) measured against total length [37].

Thus, it was proposed that two-dimensional projections can be used during compression to determine what is happening to the void structure itself. The goal was to develop a systematic method to correlate the x-ray tomography images to the foam cell morphology.

The foam characterization methods typically used attempt to define specific cell parameters, including diameter, open or closed, shape, symmetry, edge and face connectivity, cell edge and face thickness, and anisotropic features. The foam density, ρ^*, and the relative foam density, ρ^*/ρ, are closely related to cell size and amount of material residing in the cell walls, edges, and vertices [30]. The three-dimensional geometry of a foam structure relates to the mechanical properties of the foam; cellular materials are expected to provide compressive strength with little weight.

2.3.1.1.1 Imaging Methods

The charge then became one of obtaining useful two-dimensional images that could have areal, lineal, or point measurements made of specimens at known stages of compression. Optical microscopy worked best with thin specimens; the 0.040 inch specimens were somewhat opaque to transmission of optical light, but did allow excellent visualization of two-dimensional cell shapes, as seen in Figure 2.1.

Confocal microscopy was reviewed, however, improved light reflection from the cell interior walls was needed. There is an area for future experimentation with penetrant liquid coatings which allow improved light reflection.

Scanning electron images were obtained of the surface region of the cellular polysiloxane, as can be observed in Figure 2.8. While only cell openings at the surface could be seen, the circular shape of such openings was easily noted, an indication of the spherical shape of the voids. Transmission electron microscopy can be considered once a technique to obtain extremely thin specimens is determined. The test material is extremely flexible and soft, making thin sectioning difficult.

In the current study, x-ray tomography (discussed in Section 2.3.2) provided the optimum means of three-dimensional imaging of PDMS foam cells, in the uncompressed state and in various stages of mechanical compression. The images of .615 g/cc density (48% porous) foam sections (Figure 2.9) were used to characterize the initial specimen geometry, and track changes thereof caused during compression. Imaging software was used to obtain profile plots of the grayscale intensities across specimen plane images. Noting that the overall intensity range correlates with the degree of compression, one can relate the total silicon reflectance to its concentration in the image. For example, an uncompressed specimen provided a much larger darkness to brightness range, since the polymer shows a high reflectance of x-rays and the voids have absolutely none.

Another aspect of the compression is the mechanical load required, and the information rendered about the polymer. At high compressions, the value of a mechanical parameter such as the compressive modulus could approach the value determined for the solid version of the polymer. This parallels the diffusion hypothesis, and both are rooted in

free volume space. Some effort was taken to consider this aspect, due to the availability of data to related porosity in the cellular polymer to the free-volume of a fully compressed foam. It is also interesting to determine the relationship between compressed foam and solid polymer diffusion paths and mechanisms -- how does morphology predict permeability? Diffusional energy barriers might be compared to mechanical energies applied.

2.3.1.2 Linear Elastic Properties in a Polymer Foam

The force required to load foam and cause compression will depend upon the storage modulus, E, of the polymer itself. Since the cells are open, it can be assumed that all of the polymeric material resides in the vertices at the junctions and corners of adjoining voids. A parameter ϕ describes the fraction of material in the cell wall; $\phi = 1$ for a totally open-cell foam, and $\phi = 0$ for a totally closed cell foam [31]. The polysiloxane foam under study is highly open-celled, but does have substantial material in cell walls, as can be seen in optical micrographs (Figure 2.1). Foams containing minimal cell wall material have thin struts and appear almost skeletal [55].

The relative density ρ^*/ρ_s is defined as the ratio of the foam density (designated as ρ^*) to the polymer density, ρ. In the present case, this variable changes at each compression and can be calculated, as shown in Table 3.3. According to a model set forth by Gibson and Ashby [30], we then determine the foam elastic modulus E^* as:

$$\frac{E^*}{E} \cong \phi^2\left(\frac{\rho^*}{\rho}\right)^2 + (1-\phi)\left(\frac{\rho^*}{\rho}\right) \qquad (2.32$$

with the first term of the equation describing the strut portion of the cells; it would be prudent to retain some portion of the second term, however, due to the presence of material in the cell walls.

Another model was derived based upon an assumption of the struts being straight lines of length l and cross-sectional area A, and the vertices as balls having a diameter of D. The resulting relationship for a foam which has a Poisson's Ratio of ν_f is:

$$\frac{E^*}{E} = \frac{1}{5}\left(1 - \frac{2\nu_f}{3}\right)\frac{3\left(D/\ell\right)^2}{\left(1+\left(D/\ell\right)\right)}\left(\frac{nA}{\pi D^2}\right) \qquad (2.33$$

[77]. This model will not likely provide a good simulation of the polydimethylsiloxane foam, but the results of this model could be tabulated for comparison purposes.

The tetrahedral geometry forms the basis of a model proposed by Kraynik and Warren [41], which also assumes a very regular periodicity in foam structure. The Young's modulus for such a foam is:

$$\frac{E^*}{E} = \frac{33\sqrt{3}}{5}\left(\frac{\rho^*}{\rho}\right)^2\left(\frac{q^2}{A}\right) \qquad (2.34$$

where q^2/A represents a shape parameter for the strut cross-section; a circular cross-section gives rise to a $q^2/A = 1/4\pi$.

A model devised by Van Der Burg, et. al. [77] seeks to bring the random factor back into structural assumptions for the foam. They use the Voronoi tesselation geometry, which simulates the random formations of bubbles in detergent solutions. They use a generalized function of ρ^*/ρ and find that Kraynik and Warren's model is a good fit when the relative foam density is less than 0.03.

$$\frac{E^*}{E} = C\left(\frac{\rho^*}{\rho}\right)^n \qquad (2.35$$

They found that the disorder of the cellular structure has an effect on the mechanical properties, as does the recognition that the "struts" will bend during compression. In their simulation, they found increases in both Young's modulus and Poisson's Ratio as the degree of disorder increased. Their conclusion is that the presence of disorder increases the effective unit cell length, such that the unit cells contain shorter-length struts within their boundaries. The unit cells, then, are strengthened by the end-to-end presence of the struts, which transmit loads.

The x-ray tomographic data was incorporated into the models, along with previously obtained measurements, in order to provide further physical property information about the material. This also served as an examination of the various models described above.

2.3.2 X-ray Tomography

Computed x-ray tomography is a method used in the fields of medicine, biology, and geology, due to its noninvasive and nondestructive capability to obtain two-dimensional and three-dimensional images of complex structures. This method reconstructs x-ray detector signals from various paths through the specimen, comparing them to the initial beam intensity. For each incident beam I_o, passing through a sample of thickness x, an outgoing beam I_1 has been attenuated by the quantity μx, where μ is the attenuation coefficient, or energy absorption amount for the atoms contained in that thin layer Δx. Integrating over the entire x distance, each path generates an unknown value of μ:

$$\frac{I_o}{I_1} = \exp\{-\int_x \mu(x)dx\}, \qquad (2.36$$

The detectors are located in a circular array around the specimen. Precision motion translation stages provide rotation and translational movement along a z-axis, such that each point in the specimen receives x-rays across several paths. A large matrix of intensity equations are then solved for unknown values of μ, using a reconstruction algorithm called filtered back-projection [58]. This is an image reconstruction program which calculates linear attenuation coefficient values which in turn correspond with

specific elements and their spatial locations in the specimen. Consecutive slices of 35 μm resolution slices are constructed, resulting in a 3-D image which maps the set of x-ray linear coefficients.

3. RESEARCH OBJECTIVES AND RESULTS

The overarching purpose of this research was to improve the knowledge of silicone foam material permeation characteristics, particularly in conjunction with mechanical compressive forces.

3.1. Research Objectives

The objectives of this research were to:

a) Verify and validate a theoretical model for gas flow through a cellular polydimethylsiloxane (PDMS) material of 48.3% initial porosity in two flow regimes.

b) Experimentally determine the gas pressure range where flow behavior transitions from one flow regime to another. This is plotted according to theoretical models in Figure 3.1.

c) Determine the uniaxial compression range where flow behavior transitions from one regime to another. This was plotted according to theoretical models in Figure 3.2.

d) Determine the value of the permeation constant, k, a material property; compare its value to that for its nonporous analogue, P, a PDMS solid resin. This was plotted according to theoretical models in Figures 2.5 and 2.6.

e) Experimentally characterize the physical effect of compression upon cellular PDMS, such that the data can be integrated into the above gas flow model equations.

f) Ascertain PDMS foam material properties that will affect gas flow behavior and incorporate this knowledge to improve assumptions given for the theoretical model.

Polydimethylsiloxane (PDMS) was chosen as the experimental cellular material because of its use in applications where long-term energy absorption and cushioning are required. To the extent that hydrogen gas is the simplest diffusant for the predictive theoretical model, an experimental study of this gas and matrix material system was developed.

3.1.1 Research Activities

i. It was proposed that PDMS foam specimens be enclosed in a vacuum chamber in such a manner that a controlled and measured flow of gas can be released to flow through the specimen while it is compressed by some known amount. This system allowed direct measurement of the pressure of gas entering the specimen chamber (upstream), and the differential pressure drop between the pressure at the entry and exit of the specimen chamber. The exit pressure (downstream) was then easily calculated, and as expected, remained near zero due to the vacuum. The model equation for mass flow rate was plotted according to theoretical values of k and Δp, along with the experimentally determined porosity data for n_1. Actual data for Δp was then substituted in the equation to observe the actual mass flow behavior at various incoming gas pressures and foam

compressions. New permeation constants were derived as deemed necessary by experimental results.

ii. It was also proposed that the x-ray attenuation coefficient of the silicone foam be observed as specimens are compressed to known amounts. This has been done, enabling dimensional measurements using experimental images. The degree of compression was also correlated with the measured x-ray attenuation at each stage; since attenuation requires photon interaction with some element or mixture of elements. The presence of voids in a higher-Z silicon polymeric matrix provided an excellent phase contrast. Data collected for a oblong specimen shape are summarized in Table 3.1.

iii. It was proposed to merge experimental data from x-ray tomography into the gas flow data such that polymer foam material effects can be assessed. For example, true porosity numbers for n_1 can be calculated using tomographic dimensional images of specimen size changed caused by compression. The character of the porous media is quantified by the tortuosity, assumed to be constant in the gas flow model. If tortuosity could be tied to some statistical or stochastic aspect of the x-ray images, the gas flow path could perhaps be better quantified.

iv. Finally, it was proposed to modify the gas flow model as experimentally indicated in the free molecular flow and the laminar viscous flow regimes, and elucidate any transition regimes delineated by these data-based efforts.

3.1.2 Research Hypotheses

Based upon knowledge of the theoretical model, model calculations for flow through cellular PDMS, and an extensive literature review, the following hypotheses are set forth:

- A specific range of pressures and mechanical compressions were determined wherein the mechanism of gas flow transitions from one proposed flow regime to another. More specifically, a single crossover transition value for pressure and compression was identified.
- Polymer foam permeabilities decreased with increasing compression, such that its value approached that of the solid polymer.
- The tortuosity, tau, was taken assumed to be a constant value of 0.67 for purposes of the theoretical model. It was hypothesized that its value can vary such that model results are improved.
- Direct, nondestructive, and nonintrusive examination of cellular PDMS x-ray attenuation provided three-dimensional macroscopic characterization data. Such stochastic data was used directly in the gas flow model.

3.2 Experimental

This study focused upon the model devised by Kirkpatrick [39], with experiments designed to emulate the gas flow model from low to high pressures in the range 10^{-6} atm to 1 atm. The cellular polymer specimens had porosities forced from high to low (48.3% to 7.10% void space per unit volume) by compression of various amounts. Compressive loads were determined using dimensional changes as measured in tomographic images,

along with modulus data collected from other work. The x-ray attenuation coefficients as measured for the cellular material at various compressions were compared to calculated values. At each compression, material data was correlated to gas flow behavior and the permeation constant derived from that behavior.

3.2.1 Specimens

Polydimethylsiloxane foams of nominal density 0.615 g/cm^3 (48.3% porosity) were obtained from the Honeywell/Allied Signal Kansas City Plant. The polymer matrix consists of 67.6 weight percent polysiloxane gumstock and 25.6 percent silica fillers and a small amount of processing aid (ethoxy endblocked silicone oil). The polysiloxane comprises a mixture of 90.3% dimethylsiloxane, 9.0% diphenyl siloxane, and less than 1% of methylvinyl siloxane. The weight average molecular weights range from 400,000 - 700,000 with an approximate crosslink density of 28.6 kDal [44, 50]. The filled polymer was foamed by a reaction of urea and peroxide catalyst, followed by a hot water wash to remove the urea once open-walled voids are formed [15, 50, 53, 62].

Large sheets of 0.615 g/cm^3 density foam were provided by the manufacturer, Kansas City/Honeywell, along with smaller specimens of the precursor resin and a polydimethylsiloxane foam of 0.42 g/cm^3 nominal density. (The latter was used as preliminary test material for examining the feasibility of using microscopic and tomographic images.) Specimens were stamped from the 0.0394 inch (0.001 m) thickness sheet into PDMS foam disks with an outer diameter of 1.53 in (0.0389 m) and a

center hole diameter of 0.156 in (0.00465 m). A circular die press was designed and fabricated to minimize variation of specimen shape, size, and edges.

Each sample was placed in the gas flow chamber at room temperature and ambient pressure. A typical specimen and the specimen chamber are shown in Figure 3.3. After enclosure in the set up, each specimen was allowed to evacuate for a period of at least two hours in order to ensure that air is removed from the specimen and the chamber, reaching a satisfactory level of vacuum (high vacuum pressure, $p_{HV} \cong 10^{-6}$ Torr).

The shims used for specimen compression were composed of stainless steel sheet, and were fabricated in thicknesses of 0.001, 0.002, 0.004, 0.010, 0.015, and 0.020 inches. These were used in the appropriate combination to accomplish the desired compression of the 0.0394 inch height foam specimen. The inset specimen surface was of a depth of 0.022 inch, necessitating the placement of four (4) 0.017 inch shims between the sealing ring and chamber top, thus ensuring an accurate specimen gap.

3.2.2 Equipment and Apparatus

A diagram of the flow system is shown in Figure 3.4 and Appendix E. Incoming gas pressure was measured at the entry to the specimen holder using an MKS Model 690 absolute pressure manometer. The pressure differential ($pressure_{in}$ - $pressure_{out}$) was directly measured using an MKS Model 698 differential pressure manometer (Figures 3.5 and 3.8). Both manometers had their output sent to an MKS type 670B high accuracy

signal conditioner, which in turn sent data to an Omega Model 320-B data logger. The external specimen chamber temperature was tracked using a chromel-alumel thermocouple which is connected to the datalogger.

The vacuum system included a roughing pump and a high-vacuum diffusion pump to achieve lowest pressures. Downstream pressure was monitored in-situ by a Hastings gage and another MKS Model 690 manometer connected to a signal conditioner. This data was read only as a system check, and was not recorded.

There were three configurational system changes that required it to be opened to atmospheric pressure:

A) Changing the upstream portion of the system wherein flows from calibrated standard leak(s) are replaced.

B) Changing the manometers selection as required by the pressure ranges under study.

C) Changing the compression shims or a specimen.

Such changes were minimized, as pumpdown time for the system could range up to a full day. Similar experiments were grouped together in order to cause the least change and disruption to the system. For example, all 20% compression experiments were done in sequence and during the same time frame, hence only requiring one specimen chamber opening.

The specimen chamber (Figures 3.6 and 3.8) comprised a stainless steel housing in which the specimen lay upon a conflat flange with a hole in its center. This was the point of gas entry to the specimen. Gas was directed radially by the presence of a stainless steel flange on top of the specimen assembly, which was screwed down in four locations. Gas exiting from the outer diameter of the specimen was pulled upward into a concave vacuum housing, which sealed the entire assembly by knife edge against a copper gasket. The chamber was evacuated by means of stainless steel tubing and the gas was pumped up out of the chamber.

The Omega data logger allowed for systematic collection and storage of experimental data as it was generated. This could be downloaded into a spreadsheet or ASCII file for further calculations, but was typically downloaded into a newly created spreadsheet file.

3.2.3 Experimental Procedure

A gas flow experimental datasheet (Figure 3.7) was designed for systematic recording of data and observations. For each experiment, the date, time, leak serial number and compression conditions were noted. An eight-character filename was created which included codes foam compression and specific leaks being used, which were identified with "M-numbers":

❑❑ ***M*** ❑❑❑ ❑❑❑

% compression last three digits of first leak last three digits of second leak

This procedure is also described in Appendix E, which includes a diagram that identifies system components and their location, including valves and pressure manometers. The system was initally be pumped down through high vacuum with all system valves (#2,3,4, and 6) open. Valves 5 and 7 were closed. (Note: Valve #1 was eliminated when the system was altered to accommodate two leaks simultaneously.) Valves are identified in the system schematic sketch in Figure 3.8.

Hyperware files were set up with a network program written to delineate probe and net measurements; frequency of data collection; scaling of 10 Volt output on the baratrons; and any data processing required or desired for output, such as adding two outputs, etc.

The Hyperware program was set up to collect and record data, as well as display it in tabular form during the test. Data was collected and stored in a temporary Hypertrack file on the datalogger memory, as well a data file in Excel file format as described above. This was a necessary back-up, as the probe file could potentially overload with data during long runs where frequent probes were taken. The probe file and spreadsheet files are given the same filename, but with *.prb and *.xls extensions, respectively.

The datalogger remained physically connected to the computer system (Figure 3.9), however, it could be graphically connected or disconnected using Hyperware icons. In order to conduct a new experiment, the datalogger was disconnected during programming

of the net and the probe. It was then connected and the Hypernet program uploaded, thereby replacing old data.

Immediately before a run, values from the electronics readouts were written down on datasheets in order to note p_{in}, Δp, rough pump pressure, and ion gage/high vacuum level. Valve #2 was closed and valve #7 opened in order to pump off the overpressure which built inside the leak chamber once it is closed; this was tracked by observing the p_{in} gage. Valve #2 remained closed so that there is no flow into the specimen chamber until the computer probe could be initiated. This was only started after the p_{in} is down, indicating that the leak overpressure is pumped away. Valve #3 was closed in order for the differential baratron to measure the pressure drop across the specimen chamber. Leak valves were opened. To start test measurements, the following steps were taken:

- Click twice on ENABLE to start datalogger;
- Go to probe window and click on green flag to start data collection;
- Once a baseline datapoint has been recorded, close valve #7 and open valve #2 to allow gas flow into the specimen inner radius;
- Observe that datapoints continue to appear in tabular form, with increasing p_{in} and Δp seen on both the computer and the baratron gages;
- Allow test to continue until steady-state is reached, that is, both p_{in} and Δp are stable and unchanging;
- Stop test by clicking on probe red sign, only after recording gage values for p_{in}, Δp, rough pump, and high vacuum;

- Close valve #2 to discontinue flow into the system;
- Close leak valve(s) to stop gas flow;
- Open valve #7 to pump off gas and valve #3 to equilibrate differential baratron;
- Go to Excel program and open file for test just completed, which resides on hard drive Hyperware program;.
- Save spreadsheet on floppy disk for future processing and analysis.

As noted previously, it may be necessary to retrieve data in ASCII form directly from the datalogger. Therefore, it is prudent to check and ensure that a good spreadsheet datafile is actually collected and saved on a backup floppy disk BEFORE starting a new test.

Changing over of leaks (gas source) required only a limited system exposure by closing valve #2, which isolated that portion of the system. However, changing the specimen or adding compression shims required a great deal of system exposure and a longer pumpdown time (overnight). All system reconfigurations require that valves leading to pumps be closed.

Replacement leak or leaks were attached to the system using nickel seals, after closing valve #2. This side of the system (valve #7) was opened to the rough pump and allowed to pump down for about 30 minutes. The p_{in} gage was checked and to determine whether the system could be opened up to the high vacuum. At that time, valve #2 was opened and the ion gage checked to ensure for minimal perturbation, although the pressure would typically increase slightly. Pumping would continue for two hours prior to the next test.

It was necessary to change out the baratrons after the specimen compression was increased due to the increased pressures incurred. Both the p_{in} and Δp baratrons were attached using nickel gaskets, and were be calibrated prior to use. Once they were attached to system and the system was pumped down, the 670 electronics were reprogrammed such that the 10V maximum readout matched the maximum capacity of the baratron being used. The 670 was then be calibrated and zeroed in order to provide accurate data. The Hyperware net program was also be checked, and sometimes upgraded or altered such that the net program in place translated the incoming voltages according to the measurement scale in use.

3.2.3.1 Free Molecular Flow Conditions

For the free molecular measurements, very low inlet gas pressures were sufficient, and standard leaks with various gases were used as the source. The inlet pressure p_{in} and the pressure differential Δp (p_{in} - p_{out}) were measured by MKS Instruments Type 690A absolute pressure manometer, and MKS Instruments Type 698A differential pressure manometer, respectively. Three full-scale ranges were selected, according to calculated pressures expected. Incoming mass flow was calculated from the calibrated standard leak designations.

3.2.3.2 Viscous Laminar Flow Conditions

For continuum flow, a gas bottle was to be used in concert with an MKS Instruments Model 1179 mass flow controller. Again, measurements of pressure p_{in} and the pressure

differential Δp were to be accomplished using the MKS Instruments manometers of the appropriate full-scale range. Incoming mass flow was to be controlled such that the pressure p_{in} can be obtained for 760 Torr maximum. However, as will be discussed, unexpected experimental results led to additional studies in the free molecular regime, in order to better understand percolation phenomena.

3.2.4 X-Ray Tomography

Three-dimensional x-ray tomographic equipment comprising the Oak Ridge National Laboratory (ORNL) MicroCAT system was used to examine the foam structure (Figure 3.10). The MicroCAT, developed for imaging mice, used 40 kV x-rays from a 75W tungsten anode source, with a MedOptics Phosphor screen/CCD array detector. Impinging x-rays were of energy 20keV, as determined experimentally, by filtering source radiation through a 0.5 mm Al sheet. The system was controlled using Windows NT. An image slice resolution of 35 μm was used; future improvements in resolution will improve the capability to characterize cell wall shapes by possibly an order of magnitude [58]. However, each slice through the thickness of the specimen provided a map of density variation within that slice. By a layering of the slice, a three-dimensional representation of features throughout a specimen could be obtained.

Scion Image software was used to process and analyze the image data, and for direct polymer cell geometry measurements using two-dimensional cross-section plane images were analyzed. This provided statistical averages using foam x-ray attenuation

coefficients for a) quantification of features for original foam specimens, and b) changes as they were compressed.

A transparent lucite specimen holder with inside dimensions of 0.5 inch (1.27 cm) width by 1.5 inch (3.81 cm) length, 0.5 inch (1.27) height and 0.125 inch (0.317 cm) wall thickness was fabricated, through which the foam structure could be observed to a resolution of 70 nm. Lucite shims of various thicknesses were then used to obtain compressions of 10%, 20%, 30%, 40%, 50%, and 60%. Three-dimensional images were built at each of these compressive states by obtaining two-dimensional slices of 70 nm resolution. For each compressive level, some 200 slices were collected from each of the x, y, and z planes, thus requiring 600 sets of data for each compression (4200 total sets of 2-D data). A schematic sketch of the specimen holder and specimen shape is provided with Table 3.1. A stage constructed of balsa wood, a material nearly transparent to x-rays, supported the specimen and specimen holder.

3.3 Results

3.3.1 X-Ray Tomography Experiments

3.3.1.1 Data and Results

Raw attenuation data was collected for 3 μm slices through the specimen, in x, y, and z planes. This data comprised the x-ray density in grayscale levels, at each grid point through the specimen volume, and Table 3.1 provides a summary of data collected for

slices located at 10%, 25%, 50%, 75%, and 90% lengthwise through the specimen. The grayscale indication quantified the relative area of voids across a selected specimen cross-sectional area. As was seen in Figure 2.9, the average intensity of grayscale correlates with the polymer mass present, and therefore with the amount of compression. The brightest image areas occured where void space is present, with the darkest areas located at the polymer matrix is densest. For the uncompressed specimen, the grayscale range was the largest, with an average 200 points between the highest and lowest level of brightness of the image, with the lowest level of brightness being zero (total void space). With the most compressed specimen (60%), the brightness range was no more than 60; the minimum brightness never falls below 98, indicating that some polymer density is present across the entire image. The magnitude of the grayscale peaks typified the amount of attenuation, and therefore the amount of material residing in that slice of the specimen. The frequency of these peaks could be associated with the transition from void to polymer.

An image tool called the Fast Fourier Transform (FFT) was applied to a representative image for each compression level. Certainly, if the FFT transforms the two-dimensional grayscale space data to the frequency domain, general conclusions can be made. A general principle is that compression in the time or space domain causes signal expansion in the frequency domain, so one would expect to see smoother peaks in the FFT for 0% compression than those for the 60% compression. This can be observed somewhat in the Figure 3.11, but more analysis is definitely needed of this aspect. Another FFT tool in

ScionImage software applies color to the image. Figure 3.12 shows an image wherein the intensity of the yellow halo fades with compression, certainly representative of the diminishing void space. These are interesting observations, but further work is needed to quantify the application of these and other imaging tools.

The images themselves were used for direct calculation of foam density, and therefore porosity, as a function of compression. This information is summarized in Table 3.2.

Grayscale data was converted to CT numbers, achieving quantification of the x-ray interaction with the specimen. The CT number, an accepted standard in biological applications, is reported in Hounsfield Units (HU) and is an indicator of the specimen's electron density. One of the specific set of CT numbers has a scale from -1000 HU for air to +1000 HU for bone [81]. The number is based upon the linear x-ray coefficient value, μ, of the specimen as compared to that of water, μ_{H2O}:

$$\textbf{CT number} = \left(\frac{\mu - \mu_{H2O}}{\mu_{H2O}} \right) x1000 \qquad (3.1$$

where μ is the linear x-ray attenuation coefficient of the material as a function of x-ray energy. For this work, the raw attenuation data was initially converted to CT numbers. At an x-ray energy of 22.5 keV, $\mu_{H20} = 0.7\ cm^{-1}$.

CT numbers obtained from specimen center slices of area 64 pixel x 64 pixel were plotted as a function of pixel number across the width of the specimen. As in grayscale charts, the fluctuations represented void depth, with the largest appearing in the zero percent compressed specimen; CT number fluctuations decreased as the amount of compression increases, again, due to reduced void space. The average CT number was plotted for each center specimen plane and each compression in Figure 3.13, demonstrating the correlation of compression with surface area available for scattering.

At the highest compression, the CT curve seemed to approach some limiting value, which would be assumed to be the CT value for solid resin PDMS. In order to determine this limiting value, mass attenuation coefficient data from the National Institute of Standards and Technology as a function of x-ray energy was utilized [34]. Although the incipient x-ray energy was 20 keV, the absorption of lower energy rays by the specimen caused a slight increase in attenuated x-ray energies, or x-ray hardening. Therefore, the μ/ρ for elemental silicon, oxygen, carbon, and hydrogen were interpolated to an x-ray energy of 22.5 keV. Based upon the relative masses of each element present in the polydimethylsiloxane polymer (containing 25 volume percent of fumed silica filler), a resin μ/ρ value could be obtained:

$$\frac{\mu}{\rho} = \sum w_i \left(\mu / \rho \right)_i \quad . \qquad (3.2$$

Based upon calculations of the polydimethylsiloxane specimen constituents, the elemental content comprises 38.5 weight % Si, 28.7 weight % O, 26.6 weight % C, and 6.2 weight % H. Using these elemental weight fractions at x-ray energy 22.5 keV, it was found that

$$\left(\frac{\mu}{\rho}\right)_{foam} = w_{Si}\left(\frac{\mu}{\rho}\right)_{Si} + w_{O}\left(\frac{\mu}{\rho}\right)_{O} + w_{C}\left(\frac{\mu}{\rho}\right)_{C} + w_{H}\left(\frac{\mu}{\rho}\right)_{H} = 1.79 \text{ cm}^2/\text{g} \qquad (3.3$$

for the polymer solid.

One then uses the density for PDMS resin, 1.19 g/cm^3 [16], to determine that the value of linear attenuation coefficient μ is 1.93 cm^{-1}.

It was chosen to convert the CT data into the x-ray attenuation form more familiar to materials engineers, and the average experimental CT data is presented as μ/ρ data in Table 3.3. The maximum attenuation coefficient would be attained for the solid polymer, hence this theoretical value is included. The increasingly compressed foam presented μ/ρ values which approach that of the resin. Figure 3.14 demonstrates a specimen fairly uniform in elemental composition, as μ/ρ at various positions along the length give results within ±5% at all compressions [70].

3.3.1.1.2 Discussion

The process of elemental calculations for the solid polymer assumed a homogeneous specimen, as in a resin with absolutely no void space. Considering the elastomeric character of polydimethylsiloxane at room temperature, some 150 degrees above its glass transition point, a quantity of microscopic intermolecular volume might be expected; the quantitative effect upon the attenuation coefficient should be examined. The difference between the limiting value for compressed foam vs. the calculated value for a solid could perhaps be correlated to the free volume quantity.

Figure 3.15 plots both empirical foam density and attenuation coefficient as a function of compression. Straight line fits were made through both, producing nearly parallel functions. These were extrapolated to the 100% compression point for a comparison to the theoretical values. The projected empirical density is 1.21 g/cm^3 (vs. actual density of 1.19 g/cm^3, as verified by density gradient column results). The projected x-ray attenuation coefficient μ/ρ is 1.62 cm^2/g (μ = 1.93 cm^{-1}), versus the calculated (from the elements) value of 1.769 cm^2/g, resulting in a μ of 2.105 cm^{-1}.

The density value obtained using the empirical x-ray attenuation data extrapolated to 100% compressed is much smaller (14.5%) than one would expect from the theoretical solid, i.e. "void-less" polymer. This seems to indicate the presence of less polymer mass per volume than expected, which would be the case if a solid polymer could have its molecules fit together absolutely; reality requires free volume space for thermal motions

and vibrations. A calculation of free volume based upon molecular volume was done in order to estimate the elastomeric free volume expected at room temperature. This exercise used molar volumes of organic groups based on group contributions at room temperature [60], as mentioned in Section 2.1.2. In the case of the silicon contribution, data was adapted from a compilation for crystalline minerals [80].

The results of the calculation using group contribution rendered a PDMS resin volume of 71 cm^3/mol which is 14% greater than the actual volume, and included a residual volume term R of 24 cm^3/mol. However, it should be noted that this calculation did not include the 26% silica filler content of this material.

It is interesting that the foam density calculations using the x-ray data seemed to derive the expected result for the solid polymer (within 2%). This would direct a discerning eye upon the elemental calculations as compared to the empirical. Again, a denser polymer would be expected using the molecular space only. Pethrick and Van Krevelen use a value called R, the "residual volume," which has a value of 24 cm^3/mol as a catch-all for accommodation of volume required for a polymer chain movements [60, 78]. Figure 3.16 and Table 3.3 summarize various foam characteristics as compression is increased.

3.3.1.2 Application of Tomography Data to Mechanical Property Determinations

Polymeric foams offer mechanical properties based upon a light weight, and polymer density, modulus, and compressive strength [30]. These attributes are prescribed by the

matrix polymer along with the cellular geometric structure. Recognizing that the compressions in the current study require a certain loading level, the data obtained was used for mechanical property calculations.

Compression of a foam is described by the polymer modulus, E, foam modulus, E_f, compressive strain, ε, and a dimensionless function of strain that describes strut buckling, $\Psi(\varepsilon)$. The compressive stress is expressed as

$$\sigma = E_f \varepsilon \Psi(\varepsilon) . \qquad (3.4$$

E_f has a dependency on cellular structure related E and to the fraction of polymer, φ, residing in the foam. (It should be noted that the term φ is equivalent to the relative density, ρ^*/ρ, as described by Gibson and Ashby [30].) For sphere-shaped cells,

$$E_f = \frac{\varphi E}{12}\left(2 + 7\varphi + 3\varphi^2\right) = CE \quad . \qquad (3.5$$

It is appropriate that E_f approach E as φ goes to 1. The value of E for this particular PDMS polymer is given as 275 psi [20] and an empirical value for flexible polyurethane foams is used allowing a strut buckling factor $\Psi(\varepsilon) \cong \varphi^{0.28}$ [65].

Applying these relationships and above data to the PDMS cellular polymer, Table 3.4 summarizes the results of calculations made in order to obtain the foam modulus, stress, and compressive load at each compression. It would be fruitful to improve the strut buckling factor assumption, as one would expect polydimethylsiloxane to behave

differently than flexible polyurethane. The effect of filler particle and filler particle clusters, which may have dimensions similar to the foam struts, should also be considered.

A comparison was made of the mechanical data calculated using tomographic data, and actual compression tests of this material done at Lawrence Livermore National Laboratory [26]. Specimens of 1 mm thickness were compressed between two platens and stress-strain measurements taken through the "lock-up" of the cells. This terminology was applied to the fact that no lateral expansion could occur in a sample so thin; all compression was applied to cellular yielding until the 49% void space was consumed. The material locked into the solid resin, as seen in the discontinuity at $\varepsilon = 0.5$ in Figure 3.17.

Comparisons between the stress levels reached in the compression test and the tomographic calculations render nearly identical results up through the 0.4 strain level. However, it should be recalled that the tomographic studies used a block of PDMS foam which could expand into the z-direction, as seen in Figure 2.9. This difference is apparent in the mechanical data as calculated (Figure 3.18), which shows a continuous stress increase through the 60% compression. However, this effect is clearly due to the deformation allowed in the tomography compressions.

This difference in volumetric behavior is significant when considering the specimen volumes accessible to gas flow in the experimental compressive tests. As the flow specimens are also 1 mm specimens which are completely compressed, void volumes were recalculated allowing for no radial expansion, and used in the permeability calculations.

3.3.1.3 Conclusions

It was shown that x-ray tomography is a useful nondestructive method for understanding the compressive behavior of a loaded polymer foam. As a general trend, the experimentally obtained x-ray attenuation coefficient could be correlated with the effective density of the polymer foam, ρ^*/ρ, where ρ^* is the density of the original foam, and ρ is the resin (nonfoam) polymer density.

An added advantage of this method is that in-situ dimensional specimen measurements could be done during application of the compressive force. The data acquired was used to characterize certain mechanical properties of the cellular polysiloxane material [70].

Another aspect of the x-ray images relates to the flow behavior of gas at particular compressive levels. As will be seen in the next section, the permeability of the foam dropped suddenly between 30% and 35% compressions. The 2-D tomographs were examined in detail for some clue as to the morphology change which could cause this

change. Of the image analysis tools immediately available, one using a 20 color scale across the foam images rendered the most visible impact (Figure 3.10). Allowing blue to represent the lowest μ values (void), and yellow the highest (solid polymer), the images between 20 and 30 percent show a notable difference in the amount of yellow suddenly appearing.

There are certainly methods and tools to quantify these changes, and this is certainly an area of fruitful study [55]. In the present case, two aspects should be emphasized:

- The physical material changes cause the interaction with the gas flow to become altered such that the model must be extended, with percolation theorems being pursued;
- The image information for the tomographic specimens is transferable to permeation features of the flow specimens. We must recognize that morphology changes will occur *earlier (or at lower compressions)* in the actual flow specimens, again due to the thin shape of the flow test specimen and its constrainment during compression.

3.3.2 Gas Flow Experiments

The purpose of the gas flow experiments was to obtain a value for equilibrium, or steady-state pressure drop, Δp. The typical experiment resulted in the system behavior shown in Figure 3.19, where Δp ("PdropTor") and p_{in} ("PinTorr") are seen to increase steady with

time. This is the approach to steady-state where the gas radially fills the specimen voids and begins to exit the specimen from the outer edges. Eventually, the pressure values equilibrate, or reach a constant value, which is the steady-state. At this time, the pressure is sufficient to maintain diffusion through the specimen wherein the gas leaving the sample is equal to the volume going in.

At the lowest foam compressions, the cells are open and provide minimal resistance to flow; in these cases, the Δp is relatively low and the time to reach steady-state, t_{ss}, is short. At larger foam compressions, the cells or voids become restricted and delay gas transport throughout the specimen. This causes the system to engender higher pressure values at steady-state, and a lengthier time to reach that point.

Aside from foam compression, the other controlled experimental variable was mass flow rate, the amount of gas per unit time allowed to enter the specimen. It was found that the lower the mass flow rate, the more quickly steady-state pressures were reached, and at lower values.

Gas flow experiments were done in two phases. The first used a single volumetric flow rate of 3.9×10^{-5} cm^3/s, using a calibrated hydrogen "leak" source, and measured the pressure drop Δp through foam compressions of 5, 10, 15, 20, 25, 30, and 35%. There

resulted a drastic increase in Δp at the 35% level, such that higher compressions were eliminated from consideration with the current specimen size.

The second experimental phase of gas flow experiments used a series of 13 volumetric gas flows through four specimen conditions: blank (no specimen), 10%, 20%, and 30% compressions. Some data was obtained for 25% and 33% compressions in order to test the span of permeability drop. A 40% compressed specimen of reduced outer radial size is currently being tested. At this point, the Δp has continually increased in a linear manner, and has not reached a steady state value. The most recent reading for Δp was 650 Torr.

A third set of experiments flowed a variety of gases through a 5% compressed specimen in order to understand how gas properties [11] might affect permeability. These gases included hydrogen, deuterium, nitrogen, carbon monoxide, oxygen, argon, helium, and neon. Unfortunately, no correlations of Δp to gas properties, including molecular cross-section, gas viscosity, Reynolds number, mass flow rate, gas density, or interaction parameter could be made from this study. None of these results are presented herein. It is likely that repeating this experimental series with a more highly compressed foam will generate a more compelling outcome since the molecular gas size ranges near the size of the material passages.

In all tests, the incoming pressure, the pressure drop across the specimen, and the temperature were measured as a function of time. These were reported in Torr units. Data probe intervals were set for longer times in the high compression tests due to the length of time required to reach a steady-state.

3.3.2.1 Data and Results of Constant Flow Rate Experiments

Experimental data was been collected for a hydrogen flow rate of 3.9×10^{-5} cm^3/s, or in the free molecular flow regime, for compressions of 0, 10, 15, 20, 25, and 30%. For each of these experiments, data was recorded for temperature, incoming pressure (p_{in}), and pressure drop (Δp), as shown in the sample datasheet (Figure 3.7). The data gathered from this study is tabulated in Table 3.5. Curves of Δp as a function of time have been superimposed on a single chart (Figure 3.20); time for Δp to reach a steady-state value (t_{ss}) can be compared for various compressions. Three compressive states were chosen for comparison which all have data based upon the same sampling rate of 12 outputs/minute (every 5 seconds). The equilibrium Δp value massively increases as the foam is compressed. Figure 3.21 presents the Δp plateau values logarithmically. The t_{ss} is presented in this manner in Figure 3.22.

Steady-state Δp values were used in the Kirkpatrick model equations to determine effective diffusivity, D_{keff}, and permeation constants, k_{1free} and k_o, for free molecular flow of hydrogen through compressed PDMS foam. Results of these calculations are presented in Table 3.6. A spreadsheet was used to program the model equations; the

variables listing for this program is included in Appendix D. While MATLAB software by Mathworks was used mainly to process theoretical equations, the form of the experimental data lent itself to Microsoft Excel spreadsheet analysis quite readily. In fact, the Omega datalogger software, Hyperware, could specifically format and save its output as an early version *.xls spreadsheet, eliminating a large number of uploading and downloading steps. As a part of this research, programming for model flow was been done in MATLAB (Appendix D), and a sample output shown as Figures 2.3 through 2.6. Ease of tracking programming steps, hence debugging, is a great strength of MATLAB. However, the large number of experiments, data, and graphical output led the researcher to use Excel on a routine working basis.

3.3.2.1.1 Discussion

Due to the large incremental increase in Δp, smaller compressive steps were explored as the project proceeded. Since there was no x-ray tomography data for these "in-between" compressions (15%, 25%, etc.), specimen height was interpolated using data for the measured points. Using these numbers, the specimen porosity and density were estimated.

There were large increases in the pressure across the foam specimen as it is compressed, due to morphological response of the foam. Further studies are required to gain knowledge about the flow mechanisms, including additional experiments at higher

compressions, and a variety of flow gases, in order for the effect of molecular weight and gas viscosity can be demonstrated as relate to the model.

The first set of experiments was halted at the 35% compression, which resulted in a p_{in} of more than 114 Torr (the maximum baratron range) and Δp of approximately 118 Torr, after 342,000 seconds (95 hours). The rise in both p_{in} and Δp was linear, with no curvature toward a steady state value. Another approach was to reduce the distance required for gas flow to take place, i.e. reduce the specimen outer radius. This is being pursued at present. A test done for the 33% compression was completed, with the equilibrium value of Δp being approximately 25 Torr, as seen in Figure 3.23. This experiment was stopped after 171,000 seconds (2 days).

While the foam itself demonstrated linear changes due to compression, the flow-related parameters showed exponential change. Logarithmic plots of Δp and t_{ss} (Figures 3.21 and 3.22, respectively), provided more information about diffusion through the polymer, and regression analysis was done to predict flow behavior at even higher compressions. As well as being useful for comparing to theoretical Kirkpatrick equations, this was also useful for knowing approximately how long each experiment would take. Time to reach steady-state Δp values drastically increased with each compression. The sudden and abrupt change in magnitude of Δp was startling, although not a total surprise, as this value increased a great deal at each 5% compression increment. However, the mechanical compression on the foam was a much more significant variable than the flow rates under

study. That is, the change in void volume in the foam impacted permeability much more than mass flow of gas.

A linear fit of $\ln(t_{ss})$ vs. porosity projected that the 35% compression experiment being attempted would require 7 days to reach steady-state, with the second-order polynomial fit of ln (Δp) vs. porosity showing a Δp of 138 Torr. This seemed to confirm that there was a problem with the last experiment, which had reached a non-steady state Δp value of at least 118 Torr in a time of 95 hours (less than 4 days).

Experiments for 0% and 30% compression were repeated with the $3x10^{-5}$ cm^3/s flow rate, to gain improved knowledge about conducting the procedure. Since the 0% experiment was the very first to be conducted, it could be improved; review of the curve for time vs. Δp gave the researcher some doubt as to whether steady-state had actually been reached. An additional compression of 5% was done for completeness of data. Once again, the porosity was interpolated for this level of compression.

Reducing experimental results to common terms continued to be a problem if one wished to graphically compare the approach to steady state. For example, time to steady-state Δp curves cannot be directly compared where sampling rates were not identical, without further data reduction.

3.3.2.2 Data and Results of Variable Flow Rate Experiments

Data was collected for four specimen states, including an empty specimen holder (blank), and the 10%, 20%, and 30% foam compressions. For each, steady-state Δp was obtained for the following volumetric gas flows, all in cm^3/s: 1.40×10^{-6}, 2.48×10^{-6}, 3.98×10^{-6}, 6.46×10^{-6}, 1.67×10^{-5}, 2.27×10^{-5}, 2.48×10^{-5}, 2.82×10^{-5}, 3.90×10^{-5}, 4.30×10^{-5}, 5.57×10^{-5}, 6.38×10^{-5}, 6.67×10^{-5}. Each of these have also been converted to molar flow rates using the average experimental temperature, for use in calculations. This data is summarized in Tables 3.6 through 3.8.

For each compression, there was a linear response of Δp when plotted against the mass flow rate, with particular clarity in the cases of 10% and 30 % compressions. Figures 3.24 through 3.26 comprise plots of Δp plateau values as a function of mass flow rate. In the case of the 20% compression case, the data showed extreme variability, apparently due to wide temperature fluctuations in the laboratory. While these excursions may have occurred during the 10% compressions, the time-to-steady-state was within a time frame (30 minutes) over which the temperature was relatively stable. The 30% compressions called for much longer testing periods, but this appeared to level the effect of T changes on steady-state Δp. In the 20% compression experiments, the Δp clearly moved up and down with the overnight temperature. Coincidentally, this was the approximate time frame -- about 10 hours -- for 20% compression tests to reach and maintain equilibrium (see Figure 3.27 as an example). Using the Excel correlation analysis tool, it was possible to find the correlation between pressure and temperature data sets. High

correlations were found between T and Δp; p_{in} did not exhibit as much sensitivity to temperature. A method of normalizing for temperature is being sought. Factors such as $T/T_{average}$ or T/T_{min} are not of sufficient magnitude to assist in finding a "true" Δp value.

The data for flow through an empty specimen container (shown in Figure 3.26) provided confirmation that the system resistance to flow is quite low.

In order to test for regime change, p_{avg} was plotted against the conductance, which is the ratio of mass flow rate to pressure drop. If one looks at the Kirkpatrick equations, it is apparent that

$$\frac{\dot{m}}{\Delta p} = \frac{2\bar{p}\pi hk}{\mu}\ln\left(\frac{r_i}{r_0}\right) \qquad (3.6$$

for the laminar viscous flow, and

$$\frac{\dot{m}}{\Delta p} = \frac{32\pi h}{3RT}\ln\left(\frac{r_i}{r_o}\right)\sqrt{\frac{kn_1 \mathbf{T} \mathrm{RT}}{\pi}} \qquad (3.7$$

in the free molecular regime, indicating that a slope independent of pressure is expected for free molecular flow. For the 30% compression, this is the case for the larger mass flow rates. At the lowest three dm/dt ranging in the 10^{-6} cm^3/s area, there is a definite pressure dependence. This corresponds to the laminar viscous flow portion of the model.

The 20% compression data demonstrated too much variability to assess the slope, but the 10% data clearly shows the same trend: an initial increase in slope, then leveling out to a constant slope deeming independence from pressure. Conductance data is shown in Figures 3.28 - 3.31. Permeability is calculated as a function of pressure drop for the 10%, 20%, and 30% compression series, and is plotted in Figures 3.32 - 3.34.

3.3.2.2.1 Discussion

The intent of this research was to perform isothermal studies of gas flow through a foam which is uniformly and isostatically compressed. However, laboratory conditions included a temperature which varies with the weather and other situations. A temperature averaged over the course of each experiment was generally used in calculations. It should be noted that the temperature ranges being discussed here rarely exceeded a +/-2°C range, or about 4 degrees total.

An example of temperature correlation is now discussed for the 20% compressed foam with a 6.72×10^{-5} cm^3/s flow rate. Data was compared for temperature and Δp data obtained between 2,036 seconds (apparent start of steady-state) and 39,726 seconds. The correlation between these two variables is 96.4%, while the correlation between T and p_{in} is 54.2%. This same correlation was made for a 30% compressed foam and it was found that Δp and p_{in} correlate more strongly (98.2%) than do Δp and T (48.0%), or p_{in} and T (52.9%).

It would appear that the more compressed the specimen, the less temperature variations influence the flow; the less compressed (and more open passages) the specimen, the more temperature can affect the flow as represented by the pressure drop across the specimen. This relates again to the volume within the specimen through which the gas must flow.

Consider the total system volume to be the sum of the volumes in the system piping and specimen chamber, or $V_{total} = V_{incoming\ piping} + V_{specimen} + V_{exit\ piping}$. Since gas reaching the outer radius of the specimen is pumped off, the volume $V_{exit\ piping}$ is constant and zero. The incoming volume comprises piping from the gas source to the entry at the internal specimen radius. This volume is constant, as well. Finally, the volume inside the specimen impacts the gas most effectively and will vary most with temperature.

When compression is small, void space is available for gas to easily flow toward the outer radius of the sample, essentially in continuum with $V_{exit\ piping}$. Therefore, thermal expansions of gas or media do not have a measurable effect

When compression is maximized, void space is greatly decreased and the specimen volume available for gas flow is small: it is essentially polymer free volume (intermolecular space). As a result, the gas is essentially confined to the $V_{incoming\ piping}$. This means that the thermally expanding or contracting gas will not reach steady-state, but continue increasing its pressure at the specimen entry surface. Then, a large Δp and

p_{in} is observed, as well as a delayed steady-state. Any temperature effects are minimal in comparison, hence a lower correlation results between Δp and T.

Apparently, the 20% compression is midway between these two extremes, allowing gas contraction and expansion, or more significantly, polymer contraction and expansion, to closely track temperature changes. From a materials standpoint, the coefficient of thermal expansion, α, for polydimethylsiloxane is 12.0×10^{-4}/K [79], comparatively large (typical polymers have an α in the 4.8×10^{-4}/K range. This exceeds that of stainless steel, of which the chamber and shims are composed ($\alpha = 1.8 \times 10^{-5}$/K). Polymer matrix expansion and contraction will also affect the compressed cell morphology, which is complex because of the interconnectedness of the compressed open cells.

Another aspect of this problem is addressed by Lundstrom [46], who addresses the interaction of a "perturbed diameter" for a gas, and its interaction with the polymer matrix. He discusses intermolecular forces between the gas molecule and the polymer, as apply to linear displacements which can be "visualized as the distance across an open volume within the polymer matrix." This is of particular interest since he is presenting a means of determining free volume distribution within a polymer by using the diffusivity of inert gases. His study incorporates high temperature gas diameters to ascertain a function which is characteristic of the diffusive space within the polymer. The current study assumes no intermolecular forces of this type.

3.3.2.3 Knudsen Flow and The Regime Quandary

Knudsen flow, or free molecular flow, occurs in a porous material when the distance between molecular collisions is much greater than the pore diameter:

$$K_n = \frac{\ell}{d} = \frac{\text{mean free path}}{\text{pore diameter}}. \qquad (3.8$$

The pore, or void diameter is typically 0.7 mm or $7x10^{-4}$ m, as seen in optical micrographs in this case. The mean free path is calculated from the equation $\ell = \frac{k_b T}{\sqrt{2}\pi\sigma^2 p}$, where k_B is Boltzmann's constant, p is the pressure, and σ is the diameter of the gas molecule (σ_{H2} = 0.2827 nm). When K_n is a large number, the gas flow is dominated by molecular interactions with pore walls, and the flow is termed "Knudsen," or free molecular. Conversely, a small K_n indicates that gas molecules interact more with themselves and flow will be in the laminar viscous flow regime [23, 40].

When compression of the polysiloxane foam occurs, the pore diameter decreases and will increase K_n. However, the material characteristics are also being altered away from even containing pores, to being a solid elastomer: the system begins to depart from the porous model.

Using calculated values from experimental data tend to verify this behavior. When plotting P derived from k_{free} vs. Δp, permeability decreases with pressure drop across the

specimen. However, P derived from k_{lv} is seen to increase as Δp rises. This was shown to be characteristic of H_2 permeation in a polysiloxane polymer, although a solid one [10].

Let us now be more specific in noting that each new foam compression brings about a new average pore diameter. Ignoring distortion away from spherical, these were calculated based upon the original number of pores estimated in the uncompressed specimen. For each compression, a new total void space can be determined. The space is then allocated to the (unchanging) number of pores present, as if compression were uniform through the specimen volume. Assuming decreased pore diameter with each compression, a new K_n is determined. The results are summarized in the void volume calculations in Table 3.9.

It can be seen that as both compression and pressure increase, the K_n increases from a number that was never large, in a further departure from the free molecular flow regime. However, flow through this particular 48.3% porosity foam showed clear free molecular character. A similar study is reported by Satterfield [66], who noted the effect of pore radius upon the Knudsen to ordinary diffusion transition. Regardless, the permeations calculated are dominated by free molecular flow and seem to remain in that regime across the major spectrum of flow rates and compressions studied here.

Oddly enough, at the lowest mass flow rates, the flow behavior mimicked laminar viscous flow and demonstrated a conductance that was dependent on pressure. However, this was

found to be an experimental system error rather than a flow-through-the-material characteristic [40].

3.3.2.4 Flow Term for Solid Resin

Mason and Maulinauskas propose that in addition to the Knudsen flow term (free molecular flow in Kirkpatrick's model) and the laminar viscous flow term, we include a diffusion term to account for "transport of matter in an adsorbed layer" [49]. Again, this flow is treated independently of the others, and considered to have a concentration gradient across the polymer. Mason states that this adsorbed layer of gas does not have an interaction with the actual gas phase other than maintaining equilibrium. The total flux, or mass flow becomes:

$$\dot{m}_{total} = \dot{m}_{fmf} + \dot{m}_{lvf} + \dot{m}_{diff} \qquad (3.9$$

where the last term represents mass flow through the polymer resin itself. In an uncompressed foam, the 48.3% void space undoubtedly governs the flow behavior. However, at any point some fraction of gas particles will encounter a material barrier, whether it is the vertex or partial wall of an open cell. This fraction increases as the foam is compressed and the available void space reduced.

The diffusion through polymers is often approached in terms of the polymer free volume space available for permeant movement. This free volume is dispersed throughout the specimen volume, with "free volume holes" the path through which the gas molecule

must travel. The size of the hole must be compared to the cross-sectional diameter of the traveling particles, in order to ascertain the energy barrier, and hence, the ease of diffusion. This is expressed as an temperature-dependent Arrhenius relationship where

$$D(T) = D_o e^{-E_D/RT} \quad . \tag{3.10}$$

In fact, this relationship holds with solubility and permeability, as well [74], with

$$S(T) = S_o e^{-\Delta H_S/RT} , \tag{3.11}$$

and

$$P(T) = P_o e^{-E_P/RT} , \tag{3.12}$$

describing the interaction between the gas and polymer. E_D is the energy of diffusion, ΔH_S, the molar enthalpy of sorption, and E_P, the energy of permeation. The pre-exponential parameters can be found in the literature for specific polymer-gas systems.

The energy required for permeation and diffusion of permanent gases in unfilled silicone polymer is relatively small, due to the small size of such gases and the relatively large intermolecular spaces, or free volume, between the siloxane chains. It should be noted that the molecular cross-section or diameter of hydrogen is 2.82Å. However, movement of gas molecules by diffusion is much more sporadic than the "flow" through the foam's accessible space. Diffusion through a polymer requires a localized energy at the site of movement, where a segment of polymer chain moves in cooperation with the gas particle [63]. The temperature barrier described in the above equations is indicative of mobility requirements. Although the research described here was done at room temperature,

PDMS has highly mobile chains. However, the distance of movement involves a bulkier polymer than the typical membrane, hence diffusive chain cooperation is much slower.

All this aside, should we even need concern ourselves with permeation and diffusion of hydrogen through the seemingly "solid" polymer? Since permanent gases follow Henry's Law, or c = Sp how much dependence does S have on pressure (p_{in})? If no gas is absorbed by the PDMS matrix, then none can be permeate through it. This is posited by the solution to the diffusion equation for a solid resin set forth by Leckey [43]. If S is strongly pressure dependent, then perhaps at very small pressures, no adsorption, and therefore, no permeation will occur at all. The solution to the differential equation describing diffusion through a solid polymer specimen of the geometry in this research leads to a conclusion that the mass flow rates being applied would not suffice to cause sorption into the polymer. However, with time and increased pressure, some gas would begin to enter the polymer and exit from the outer radius. The Leckey model provides a mass flow term:

$$\dot{m}_{diff} \leq \frac{2\pi Dh\beta P}{\ln\left(r_o/r_i\right)}, \tag{3.13}$$

where β is a solubility term [43]. This model can be tested and incorporated into the model as the polymer diffusion term.

3.3.2.5 Applicability of Percolation Theory

An abrupt change in flow behavior occurs in this foam between the 25 and 30% compressive state. At this point, the porosity is reduced to approximately 0.30 (where porosity is defined as the ratio of void volume to specimen volume); this appears to be the critical stage at which an accessible flow path is cut off. The percolation theory might be used to characterize the abrupt rise in pressure drop required to achieve diffusion through compressed foam, as well as the concomitant abrupt decrease in permeability this indicates.

The critical stage mentioned above is known as a critical percolation threshold, p_c. At lower levels of compression, the porosity or percolation path is larger and there is an open flow path from the inner specimen radius to outside radius -- permeability is high. When the porosity goes below p_c (occurring at higher compressions), the accessible volume is diminished, thereby dramatically decreasing perrmeability.

At large compressions, there may still be "microdomains" of open cells, but these are isolated and unavailable as a percolation path. For a two-dimensional situation, an example model is shown in Figure 3.35 for 20 flow sites in a 4 by 5 matrix. In this illustration, flow is taking place from left to right. At the initial foam porosity of 0.483, about 50% of sites are open to flow and 50% are closed, resulting in the effective diffusivity and permeability determined for 0% compressed foam. As compression increases, fewer open flow sites exist, ultimately reducing flow paths through the

specimen. This model is quite simplistic, but serves to illustrate the percolation concept [32]. It also confirms the lack of a flow path when the foam is 30% compressed; porosity has fallen below the critical percolation value. This is shown experimentally in the plot of permeability as a function of foam porosity (Figure 3.36).

In the Effective Medium Approximation (EMT) method, one could state that the critical percolation value, p_c, occurs at a porosity or accessible volume of 25 - 35%. This corresponds to a p_c occurring for cells having a coordination number of 8 and a body-centered cubic geometry [67]. Through a somewhat indirect means, this is an additional clue to the cellular morphology and structure of polysiloxane open cell foam.

Another aspect of the percolation theorem equates porosity to the tortuosity. Sax and Ottino [69] express tortuosity for a heterogeneous composite material that contains a high permeability component and an impermeable component:

$$\tau = \frac{\phi_m}{D_{eff} S_{eff} / D_m S_m}, \qquad (3.14$$

where ϕ_m is the volume fraction of impermeable material, and D_{eff} and D_m are the diffusivity of the permeant in composite and impermeable material, respectively. S_{eff} and S_m are the similar solubility values. Recalling that the permanent gases permeating through polysiloxanes follow Fick's Law, we can then write for the current system:

$$T = \frac{\phi_{polymer} P_{polymer}}{P_{foam}} \quad , \qquad (3.15$$

where $P_{polymer}$ is the reference value for permeability of the gas through a solid polymer. Now values for $\phi_{polymer}$ and P_{foam} are variables dependent on compression, bringing about a variation in the tortuosity. Rather than being a constant, as assumed in the Kirkpatrick model, T could be set as a function of porosity, n_1. If this is the case, at very large compressions, $P_{polymer}$ approaches P_{foam}, and $\phi_{polymer}$ approaches 1; tortuosity then approaches the value 1, meaning that flow paths straighten out.

3.3.2.6 Conclusions

This gas flow measurement system worked well for the low compression-low gas pressure case, and provided data for laminar viscous and free molecular flow. The data followed a pattern which allowed prediction of behavior at higher compressions. The Kirkpatrick model seemed to apply in the laminar viscous flow regime for the system and conditions under study.

In the case of reducing specimen radii, one cannot directly contrast the magnitudes of Δp without factoring in this new distance across which the drop is being measured. For this purpose, a means of normalizing Δp data using $\ln(r_i/r_o)$ was used to predict the Δp for a smaller specimen outside radius. This was done by putting the diffusive flow equation into the form:

$$A(c) = \frac{\dot{m}}{\Delta p} \ln\left(\frac{r_o}{r_i}\right), \qquad (3.16$$

or $$B(c) = \frac{\dot{m}}{\Delta pp} \ln\left(\frac{r_o}{r_i}\right), \qquad (3.17$$

where A(c) is some function of compression that represents the remaining terms in the free molecular flow portion of Eqn. 2.26, and B(c) is a function of compression representing the laminar viscous flow portion..

4. SUMMARY

4.1 Results

The research was completed as proposed, although findings were made far before the full extent of foam compressions and gas flow rates were reached. PDMS foam specimens were subjected to flow tests using hydrogen gas and various foam compressions. Permeability as a function of compression and gas flow was determined. Extensive data was obtained for compressions ranging from 0 to 35% in 5% increments for a single gas flow; extensive data was obtained for compressions ranging from 0 to 30% in 10% increments for thirteen gas flows. Results provided verification of the Kirkpatrick model within certain parameters, and led to model modifications to account for percolation effects and solid polymer diffusion. The two latter diffusion mechanisms interfere with the bundle of tubes assumption of uninterrupted flow at compressions up to 60%.

Conductances in the gas flow range studied showed a pressure dependence at the lowest three mass flow rates (dm/dt in the 10^{-6} cm^3/s range), but all higher flow rates brought about conductance values that were independent of pressure. This would seem to indicate a transition from laminar viscous flow at lower dm/dt values into a free molecular flow regime. However, calculations of the Knudsen constant for this polymer-permeant system show K_n values of one or greater, which indicate free molecular flow dominance at the mass flow rates studied. The largest calculated K_n values occur for the lowest

pressures, which are also the lowest dm/dt values -- indicative of free molecular flow regime.

X-ray attenuation was used to characterize foam changes due to compression, and mechanical properties were ascertained. The resolution was not sufficient to quantify tortuosity, but the stochastic data could be correlated to a percolation critical volume of void space. The distinct contrast provided by a silicon-based polymer rendered excellent images of the morphological response to foam compression. The image data was used in concurrence with theoretical models for foam mechanical properties. The calculated results agreed surprisingly well with experimental compression data for the same foam, to the extent that the specimen configuration changed the response.

4.2 Future Directions

Gas flow experiments should be continued for higher foam compressions using a smaller specimen outer radius. This should enable testing to be completed in a reasonable time frame, and at measurable Δp values. A variety of gases can be flowed through a highly compressed volume of the foam in order to obtain more information about the polymer structure with respect to various gas properties. This interaction is an intriguing one, since one can then correlate a property or combination of properties to permeation results. Gases which are condensable or reactive can also be used to discover how the Langmuir mode of absorption affects diffusion and permeation behavior.

Another stage would be to widely broaden the range of flow rates being studied to learn how much flow response is altered by this variable. It would also be instructive to repeat the current study for a more porous polydimethylsiloxane foam in order to attain definitive free molecular flow vs. laminar viscous parameters. In the case of a 60% porous foam, it may be possible to achieve appropriate pressures needed for such; however, it should be remembered that the pore diameters will also be larger. This foam morphology would also provide additional accessible flow paths for percolation studies.

Further examination of the percolation mechanism would be useful, and is applicable to all polysiloxane foam porosities. A study of compressive effects on various foams could allow determination of the critical percolation value of each foam type, offering additional cell morphology characteristics for each. MicroCAT resolution improvements are another key to more detailed cellular structure elucidation before and during compression. It is also possible that higher resolutions can be achieved by using a higher flux x-ray source, such as a synchrotron [38].

Another application for the x-ray tomography would be a method of visually observing permeation of a gas as the polysiloxane foam is compressed. This would be possible using a tracer gas, or some gas capable of refracting x-rays. Actual flow paths and percolation mechanisms could be observed.

Future plans would include microtome sectioning at liquid nitrogen temperatures to obtain a minimally damaged set of specimens. Transmission electron microscopy (TEM) images would provide detailed two-dimensional images to better elucidate the structure of microvoids of the order of nanometer scale. These are a separate class of voids than those considered in other imaging methods, and are probably of closed-cell structure. They certainly contribute to the degree of porosity in these materials, but most likely do not enhance the permeability of the foam [65].

The open cell structure might be further observed by flooding foam specimens under various compressions with a monomer. One could then polymerize the monomer at room temperature and obtain solid sections for studies using optical microscopy. This method of pervading the deformed voids would effectively "freeze" in the compressed morphology for detailed study.

4.3 Conclusions

The Kirkpatrick model works well at foam compressions up the 30% range, at which the bundle of tubes approximation breaks down due to tube discontinuities. Under the experimental conditions of this study, all flow occurs in the molecular flow regime. There is then a transitional flow mechanism through a percolation regime, which leads to the traditional diffusion through a solid polymer. A solid polymer, or resin, contains only fractional free volume and a minimal amount of void volume, resulting in a permeability near zero as compared with an open cell foam.

As long as the critical percolation point was not exceeded, gas flow studies of compressed foam demonstrated a permeability which is linearly dependent upon mass flow rate. These studies also demonstrated a permeability which is exponentially dependent upon the degree of compression. The abrupt drop in diffusivity of this random heterogeneous material was readily tied to flow path blockage as the open cells collapsed with compression.

Mechanical properties could be calculated from x-ray tomography data used to characterize the foam at various compressions. Grayscale images could ultimately be correlated with x-ray attenuation from the foam, and therefore the elemental composition at each compressive level. There is a great deal of potential for detailed cellular characterization of this and other silicon-based polymer foams.

Further study of the tomographic images is providing improved correlation of material properties with the flow behavior. Examples of foam images shown in Figure 3.38 clearly show compression effects on morphology, wherein voids are deformed parallel to the load direction. These images are "stacks" of image slices taken of the specimen cross-section through its length. In Figure 3.39, the Fast Fourier Transform (FFT) images for 20%, 40%, and 60% compressions will be explored for quantitative void-to-void distance and size information.

LIST OF REFERENCES

LIST OF REFERENCES

1. Aranguren, M. I., Morphology and Rheology of Silica Reinforced Silicone Rubbers, Dissertation for the Univ. of Minnesota, March, 1990.

2. Aranguren, M. I., Mora, E., Macosko, C. W., and Saam, J., Rubber Chem. and Technology, Vol. 67, 5, 820, 1994.

3. Arrighi, V., Higgins, J. S., Burgess,A. N., and Floudas, G., Polymer, Vol 39, 25, 6369, 1998.

4. Auerbach, I., Miller, W. R., Kuryla, W. C., and Gehman, S. D., J. Polym. Sci., Vol. 28, 129, 1958.

5. Baird, D. G., and Collias, D. I., Polymer Processing Principles and Design, Butterworth-Heinemann (Boston), 1995.

6. Barrer, R. M., *Diffusion and Permeation in Heterogeneous Media*, in Diffusion in Polymers, Crank, J., and Park, G. S., Ed., Academic Press (London), 1968.

7. Barrer, R. M. and Chio, H. T., J. Polym. Sci.: Part C, No. 10, 111, 1965.

8. Bear, J., Dynamics of Fluids in Porous Media, American Elsevier (New York), 1972.

9. Bear, J. and Bachmat, Y., Introduction to Modeling of Transport Phenomena in Porous Media (Theory and Applications of Transport in Porous Media, Vol 4), Kluwer Academic, (Dordrecht), 1991.

10. Bhide, B. D., Stern, S. A., J. Appl. Polym. Sci., 42, 2397, 1991.

11. Braker, W. and Mossman, W. L., Matheson Gas Data Book, 6th Edition, Matheson (New Jersey), 1980.

12. Breiner, J. M., Mark, J. E., and Beaucage, G. J. Polym. Sci: Part B: Polym. Phys., Vol. 37, 1421 (1999)

13. Briscoe, B. J., Savvas, T., and Kelly, C. T. Rubber Chem. and Technology, Vol. 67, 3, 384, 1997.

14. Cabot Corporation website address http://www.cabot-corp.com/cabosil/cabosil.nsf/.

15. Cady, W. E., Jessop, E. S., and McKinley, B. M., Evaluation of the Use of HiSil 233 in Silicone Elastomers and Cellular Silicones, Lawrence Livermore National Laboratory Report UCRL-53298, 1982.

16. Cady, W. E., Jessop, E. S., and McKinley, B. M., Property of Cellular Silicone from High Vinyl Silicone Gums as a Function of Porosity, Lawrence Livermore National Laboratory Report UCRL-53366, 1982.

17. Canadian Building Digest, CBD-166: Plastic Foams, website http://www.nrc.ca/irc/cbd/cbd166e.html, National Research Council of Canada, (Montreal), 1974.

18. Carman, P. C., Flow of Gases Through Porous Media, Academic Press (New York), 1956.

19. Chainey, M. *Transport Phenomena in Polymer Films (Chapter 11),* in Handbook of Polymer Science and Technology, Volume 4: Composites and Specialty Applications, Chereminsinoff, N. P., Ed., Marcel Dekker (New York), 1989.

20. Chien, A. T., Felter, T., LeMay, J. D., Balooch, M., J. Mat. Sci., Vol. 15, 4, 838, 2000.

21. Clarson, S. J. and Semlyn, J. A., Ed., Siloxane Polymers, Prentice Hall (New Jersey), 1993.

22. Cochrane, H., and Lin, C. S., Rubber Chem. and Technology, Vol. 66, 48, 1993.

23. Cussler, E. L. Diffusion: Mass Transfer in Fluid Systems, Cambridge University Press (Cambridge), 1984.

24. Daniels, F., and Alberty, R. A. Physical Chemistry, 4th Ed., Wiley (New York), 1975.

25. Daynes, H. A., The Process of Diffusion Through a Rubber Membrane, Proc. Roy. Soc. (London), A97, 286, 1920.

26. DeTeresa, S., Informal communications, Lawrence Livermore National Laboratory, 2001.

27. Duda, J. L. and Zielinski, J. M., *Free-Volume Theory*, in Diffusion in Polymers, Neogi, P., Ed., Marcel Dekker (New York), 1996.

28. Flory, P. J. Principles of Polymer Chemistry, Cornell University Press (Ithaca, 1953).

29. Fried, J. R., Polymer Science and Technology, Prentice Hall (New Jersey), 1995.

30. Gibson, L. J., and Ashby, M. F., Cellular Solids: Structure and Properties, 2nd Ed., Cambridge Univ. Press (Cambridge), 1997.

31. Goods, S. H., Neuschwanger, and C. L., Whinnery, L. L., Mechanical Properties of a Structural Polyurethane Foam and the Effect of Particulate Loading, Sandia National Laboratory Report SAND-98-8549C, 1998.

32. Ha, S. Y., Park, H. B., and Lee, Y. M. Macromol., 32, 2394, 1999.

33. Harper, J. R., and Bauman, T. M., *Silicone Foams, Chapter 14*, in Polymeric Foams, Klempner, D., and Frisch, K. C., Ed., Hanser (Munich), 1991.

34. Hubbell, J. H., and Seltzer, S. M., NISTIR 5632: Tables of X-Ray Mass Attenuation Coefficients and Mass Energy-Absorption Coefficients, National Institute of Standards and Technology at website address http://physics.nist.gov/PhysRefData/XrayMassCoef/, 1996.

35. Jost, W., Diffusion in Solids, Liquids, Gases, Academic Press (New York), 1952.

36. Kamiya, Y., Naito, Y., Hirose, T., and Mizoguchi, K., J. Polym. Sci.: Part B: Polym. Phys., Vol. 28, 1297, 1990.

37. Kampf, G., Characterization of Plastics by Physical Methods, Hanser (Germany), 1986.

38. Kinney, J. H., and Nichols, M. C., X-ray Tomographic Microscopy (XTM) using Synchrotron Radiation, Lawrence Livermore National Laboratory, UCRL-JC-109133, 1992.

39. Kirkpatrick, J. R., A Very Approximate Theory for Gas Transport in a Polymer Foam, Oak Ridge National Laboratory Report ORNL/TM-1999/204, December, 1999.

40. Kirkpatrick, J. R., Informal communications, Oak Ridge National Laboratory, 2001.

41. Kraynik, A. M., and Warren, W. E., *The Elastic Behavior of Low-Density Cellular Plastics*, in Low Density Cellular Plastics, Hilyard, N. C., and Cunningham, A., Ed., Chapman and Hall (London), 1994.

42. Kuo, A. C. M., *Poly(dimethylsiloxane)*, in Polymer Data Handbook, Mark, J. E., Ed. Oxford Univ. Press (New York), 1999.

43. Leckey, J. H., Radial Diffusion at Constant Mass Flow in a Hollow Cylinder, Draft Paper, 2000.

44. LeMay, J. D., Electronic Correspondence to Leckey, J. H., 1997.

45. Lewis, F. W. "Elastomers by Condensation Polymerization", in Polymer Chemistry of Synthetic Elastomers, Part II, ed. by Kennedy, J. P. and Tornqvist, Erik, Interscience Publishers (New York), 1969.

46. Lundstrom, J. E. Molecular Transport Through Thin Membranes, Ph.D. Dissertation, University of Kansas, 1969.

47. Lundstrom, J. E. and Bearman, R. J., J. Polym. Sci., Polym. Phys. Ed., Vol. 12, 97, 1974.

48. Lynch, W., Handbook of Silicone Rubber Fabrication, Van Nostrand Reinhold (New York), 1978.

49. Mason, E. A., and Malinauskas, A. P., Gas Transport in Porous Media: The Dusty-Gas Model, Elsevier (Amsterdam), 1983.

50. Maxwell, R. S., Balazs, B., Chien, A., and LeMay, J., Radiation Induced Structural and Motional Changes Occurring in Silica Filled Silicone Polymer Foams as Probed by Multinuclear NMR, U.S. Dept. of Energy, LLNL Report #UCRL-JC-135979, 1999.

51. Michaels, A. S., and Parker, R. B., Jr., J. Polym. Sci., Vol. 41, 53 (1959).

52. Moisan, J. Y., *Effects of Oxygen Permeation and Stabiliser Migration on Polymer Degradation*, in Polymer Permeability, Comyn, J., Ed., Elsevier Science (London), 1986.

53. Monaco, S. B., Davis, L. D., and Richardson, J. H., Chemiluminescence of Polysiloxane Cushions: Correlation with Physical Properties, U.S. Dept. of Energy, LLNL Report #UCRL-90342, 1984.

54. Monaco, S. B., Richardson, J. H., Breshears, J. D., Lanning, S. M, Bowman, J. E., Walkup, C. M., Ind. Eng. Chem. Prod. Res. Dev., Vol. 21, 4, 1982.

55. Montminy, M. D., Tannenbaum, A. R., and Macosko, C. W., Foams 2000 Technical Conference, Parsippany, N. J., 2000.

56. National Aeronautics and Space Administration, U. S. government, at web site address: http://roland.lerc.nasa.gov/~dglover/dictionary//k.html.

57. Neilsen, L. E., J. Macromol. Sci. (Chem..), A1, 5, 1967.

58. Paulus, M. J., Sari-Sarraf, H., Gleason, S. S., Bobrek, M., Hicks, J. S., Johnson, D. K., Behel, J. K., Thompson, L. H., and Allen, W. C. IEEE Trans. Nucl. Sci., 46, 3, 1999.

59. Pauly, S., *Permeability and Diffusion Data*, in Polymer Handbook, 3rd Edition, Ed. Brandrup, J., Immergut, E. H., Wiley (New York), 1989.

60. Pethrick, R. A., Polymer Yearbook 2, Harwood Academic (Chur), 1985.

61. Plaspec database, at web site address: http://www.plaspec.com, 2000.

62. Riley, M. O., Kolb, J. R., and Jessop, E. S., The Commercial Synthesis of M97KVB Gum, A Precursor to Cellular Silicone Cushions, Part I, U.S. Dept. of Energy, LLNL Report #UCRL-87584, 1982.

63. Rogers, C. E., *Permeability and Chemical Resistance (Chapter 9)*, in Engineering Design for Plastics, ed., Baer, E., Reinhold (New York), 1964.

64. Rogers, C. E., *Permeation of Gases and Vapours in Polymers (Chapter 2)* in Polymer Permeability, ed. Comyn, J., Elsevier (London), 1986.

65. Rusch, K. C., J. Appl. Polym. Sci., 13, 1969.

66. Satterfield, C. N., Mass Transfer in Heterogeneous Catalysts, M.I.T. Press (Cambridge), 1970.

67. Sax, J., and Ottino, J. M., Polym. Eng. & Sci., 23, 3, 1983.

68. Seymour, R. B., *The Role of Fillers and Reinforcements in Plastics Chemistry*, in Fillers and Reinforcements for Plastics, ed. Deanin, R., ACS (Wash., D. C.), 1974.

69. Shutov, F. A., Adv. Polym. Sci., Vol. 51, 155, 1983.

70. Smith, R. A., Paulus, M. J., Branning, J. M., and Phillips, P. J., J. Cell. Plast., accepted for publication, 2001.

71. Stannett, V., *Simple Gases (Chapter 2)*, in Diffusion in Polymers, Crank, J. and Park, G. S., Ed., Academic Press (London), 1968.

72. Stein, W. D. Transport and Diffusion across Cell Membranes, Academic Press (Orlando), 1986.

73. Struik, L. C. E., Physical Aging in Amorphous Polymers and Other Materials, Elsevier Scientific (Amsterdam), 1978.

74. Thompson, L. M., Unpublished data, Lockheed Martin Energy Systems, Y-12 Plant (2000).

75. van Amerongen, G. J., J. Polym. Sci., Vol. 2, 4, 381, 1947.

76. van Amerongen, G. J., Rubber Chem. and Tech., Vol. 35, 1-5, 1065, 1964.

77. Van Der Burg, M. W. D., Shulmeister, V., Van Der Geissen, and Marissen, R., J. Cellular Plastics, Vol. 33, 31, 1997.

78. Van Krevelen, D. W. Properties of Polymers - Their Correlation with Chemical Structure; Their Numerical Estimation and Prediction from Additive Group Contributions, 3rd Edition, Elsevier (Amsterdam), 1990.

79. Warrick, E. L., and Lauterbur, P. C., Industrial and Eng. Chem., Vol. 47, 3, 486, 1955.

80. Weast, R. C., Handbook of Chemistry and Physics, CRC Press (Florida), 1978.

81. Wynn, G. J. Imaging for Idiots at website address: http://www.teaching-biomed.man.ac.uk/student_projects/2000/mmmr7gjw/glossary.htm#H .

82. Ziegel, K. D., and Eirich, F. R., J. Polym. Sci.: Part A-2, 8, 2015, 1970.

APPENDICES

Appendix A: Figures

Figure 2.1 Optical micrograph of 0.615 g/cm^3 density polysiloxane foam at 100x magnification.

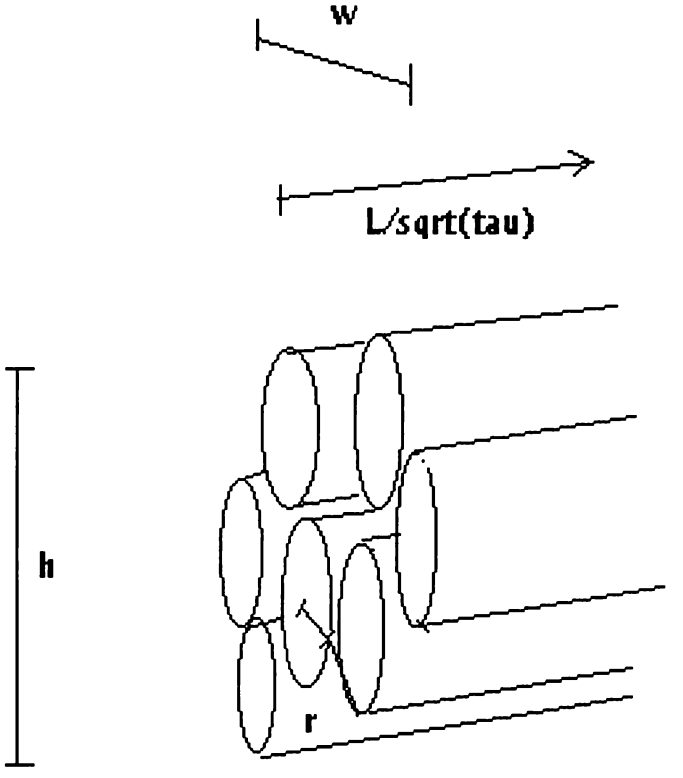

Figure 2.2. Sketch of "bundle of tubes" concept for open cell foam model. Number $\mathbf{N_t}$ of tubes of radius $\mathbf{r_t}$ in a block of foam with dimensions **w** x **h** x **L**. Tubes have length $\mathbf{L}/\sqrt{T}$, where T is the tortuosity constant which increases the effective path of flow, due to tube curvature.

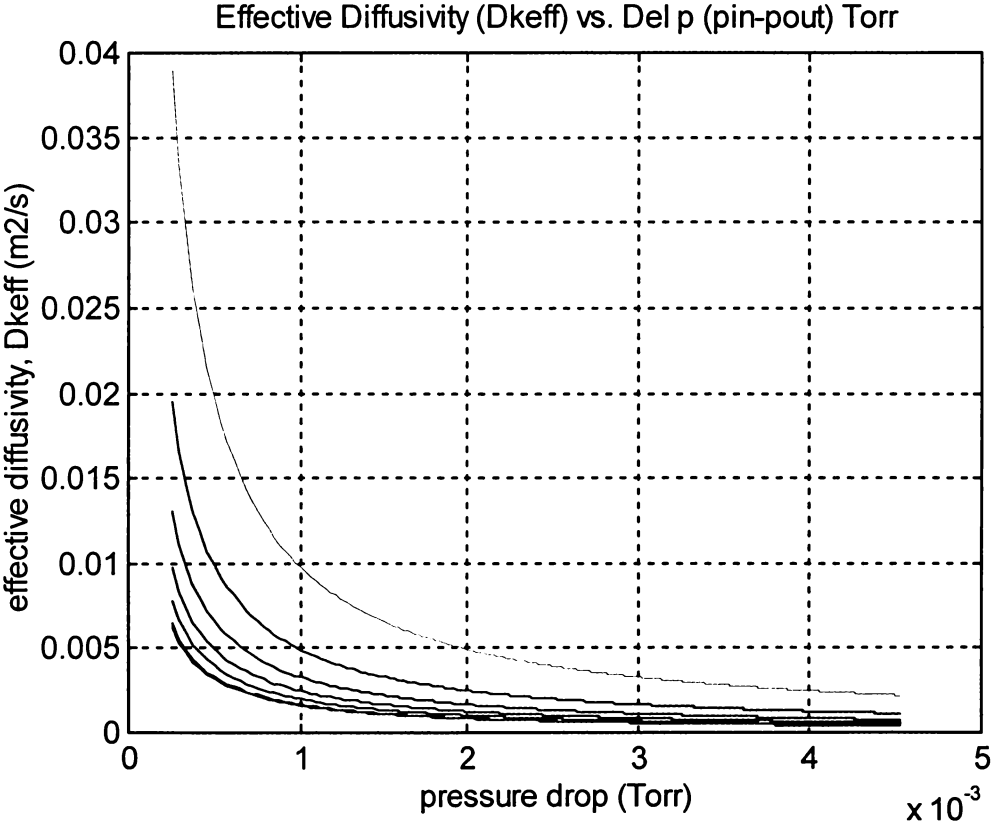

Figure 2.3. Theoretical equation for diffusivity through porous foam assuming a small pressure drop in the free molecular flow regime. The top line assumes no compression; each additional line represents a 10% incremental level of compression.

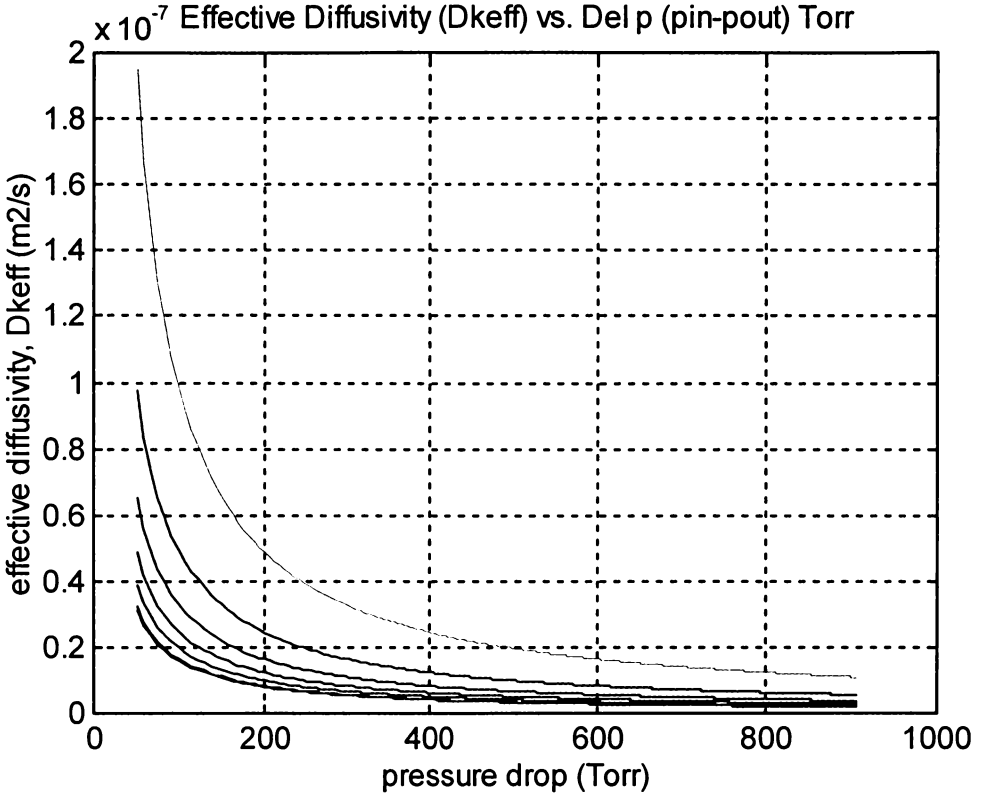

Figure 2.4. Theoretical equation for diffusivity through porous foam assuming a large pressure drop in the free molecular flow regime. The top line assumes no compression; each additional line represents a 10% incremental level of compression.

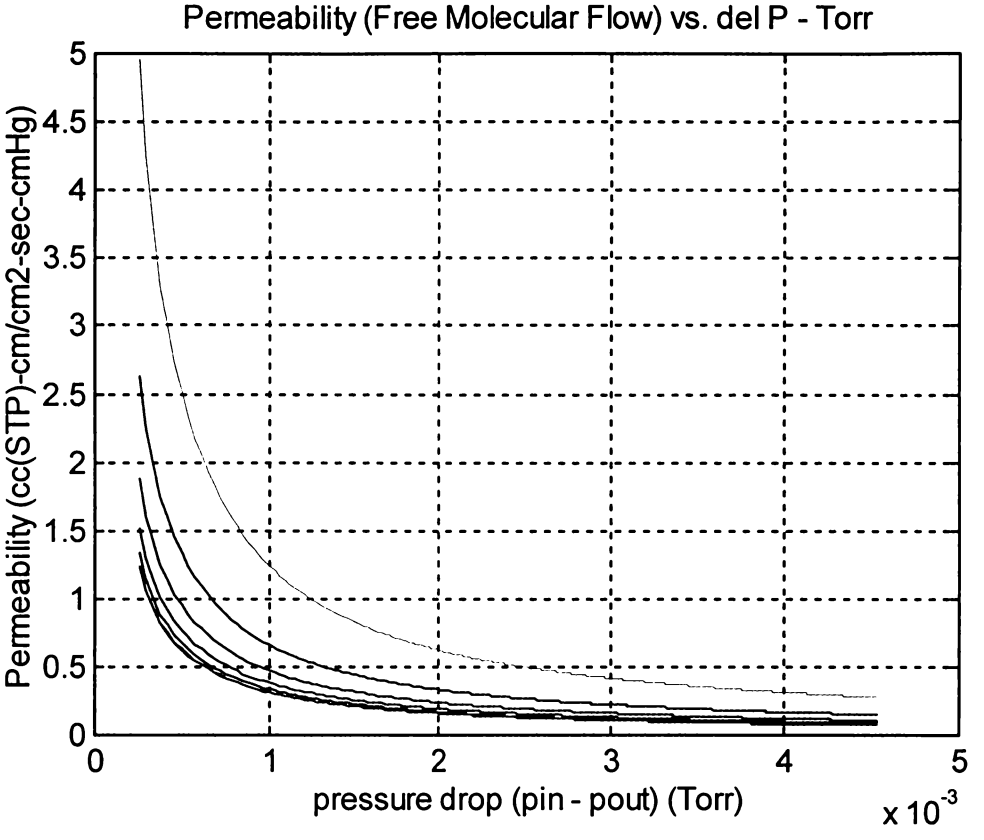

Figure 2.5. Theoretical equation for permeability through porous foam assuming a very small pressure drop in the free molecular flow regime. The top line assumes no compression; each additional line represents a 10% incremental level of compression.

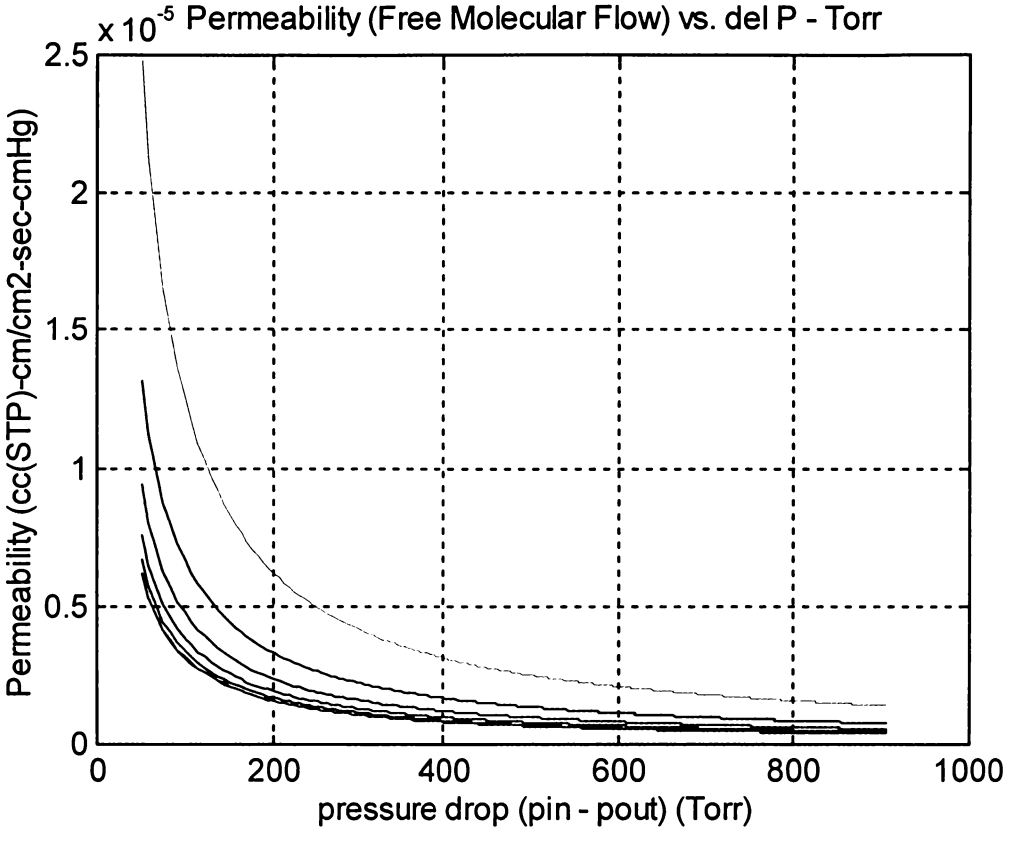

Figure 2.6. Theoretical equation for permeability through porous foam assuming a large pressure drop in the free molecular flow regime. The top line assumes no compression; each additional line represents a 10% incremental level of compression.

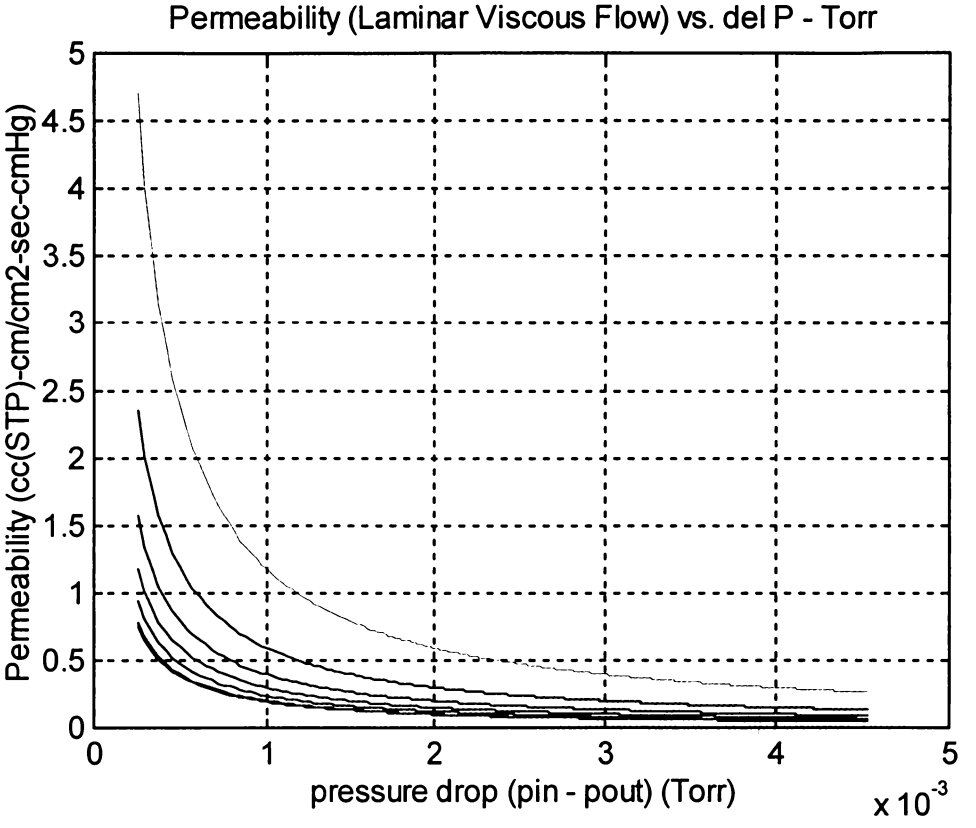

Figure 2.7. Theoretical equation for permeability through porous foam assuming a very small pressure drop in the laminar viscous flow regime. The top line assumes no compression; each additional line represents a 10% incremental level of compression.

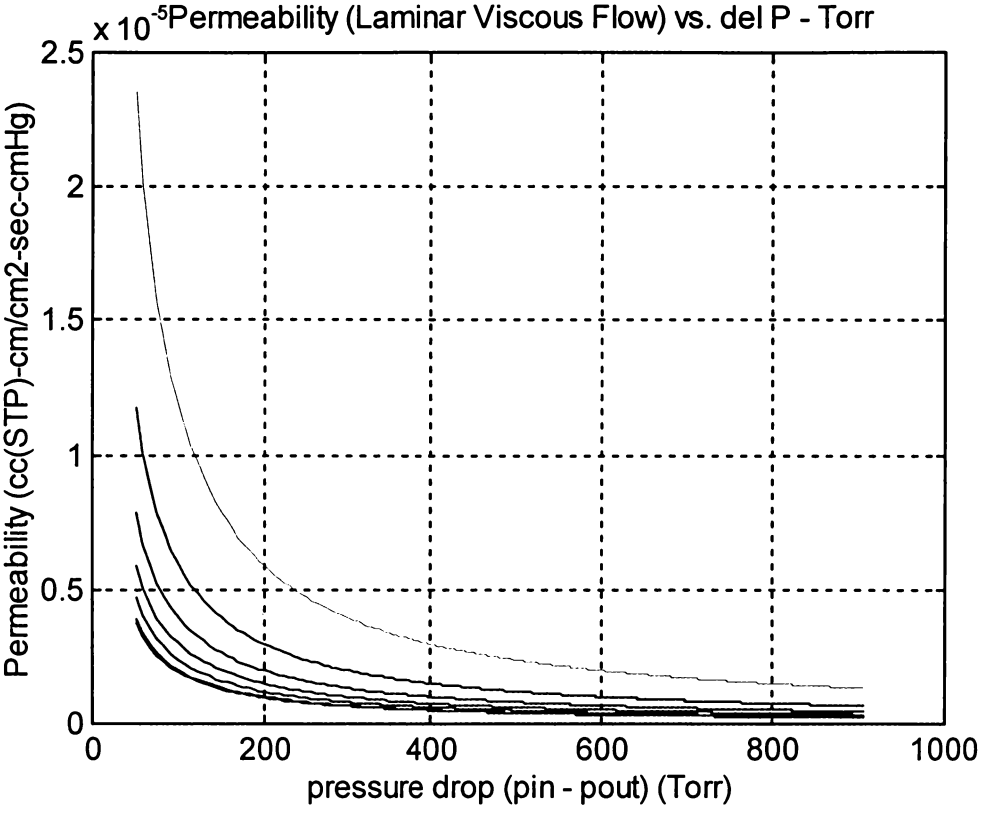

Figure 2.8. Theoretical equation for permeability through porous foam assuming a large pressure drop in the laminar viscous flow regime. The top line assumes no compression; each additional line represents a 10% incremental level of compression.

Determination of uncompressed or initial porosity n_0, where:

$$\text{porosity} = \frac{V_{void}}{V_{specimen}}$$

Let $V_{specimen} = 1\ cm^3$

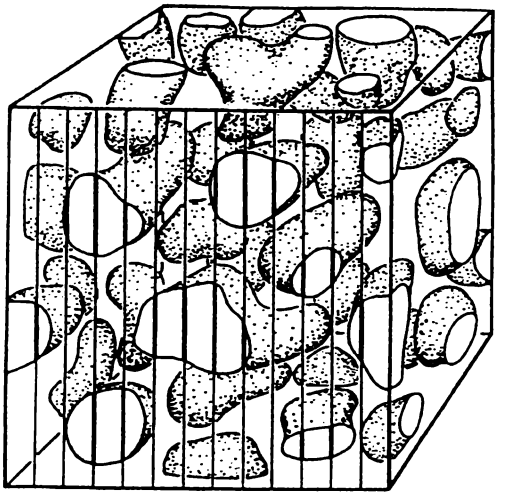

Foam volume has density = 0.615 g/cm^3 ∴ the solid polymer mass in $V_{specimen}$ is 0.615 g.

Since the solid polymer has a density of 1.19 g/cm^3,

$$V_{polymer} = 0.615g * \left(\frac{cm^3}{1.19g}\right) = 0.517cm^3.$$

This means that $V_{void} = 1 - V_{polymer} = 1 - 0.517 = 0.483\ cm^3$, hence:

$$\text{porosity} = \frac{V_{void}}{V_{specimen}} = \frac{0.483cm^3}{1.0cm^3} = 0.483.$$

Figure 2.9. Example volume containing a dispersed void phase, the content of which can be determined by cross-sectional lengths shown. *Source: Kampf, G., Characterization of Plastics by Physical Methods, Hanser (Germany), 1986.* Definition of porosity.

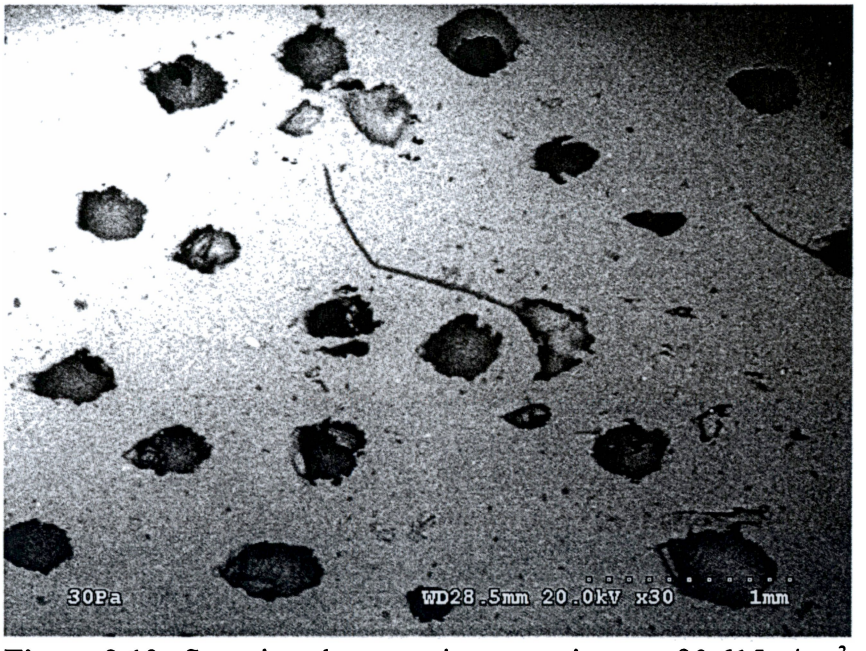

Figure 2.10. Scanning electron microscope image of 0.615 g/cm^3 density polysiloxane foam specimen surface at 30x magnification.

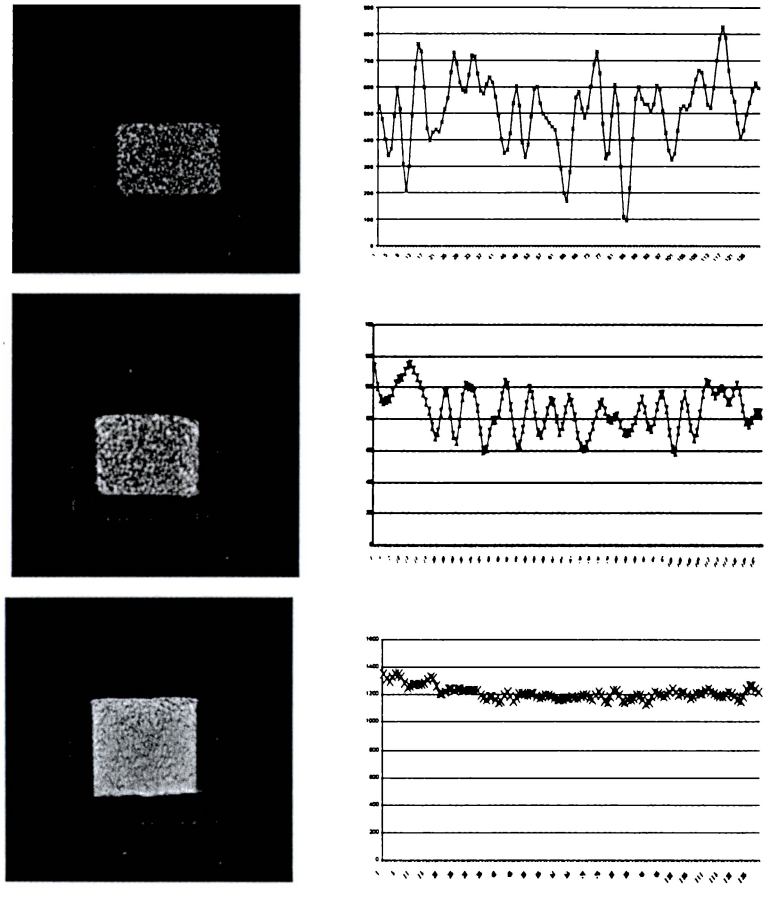

Figure 2.11. At left: x-ray images of 0%, 30%, and 60% compressed foam specimens across midsection. At right: respective grayscale variation plots of average CT number as a function of pixel number. Specimen width of 1.27 inches equates to 128 pixels . Note that grayscale plots include data for specimen only, and not the specimen holder (seen as a u-shape in the x-ray images).

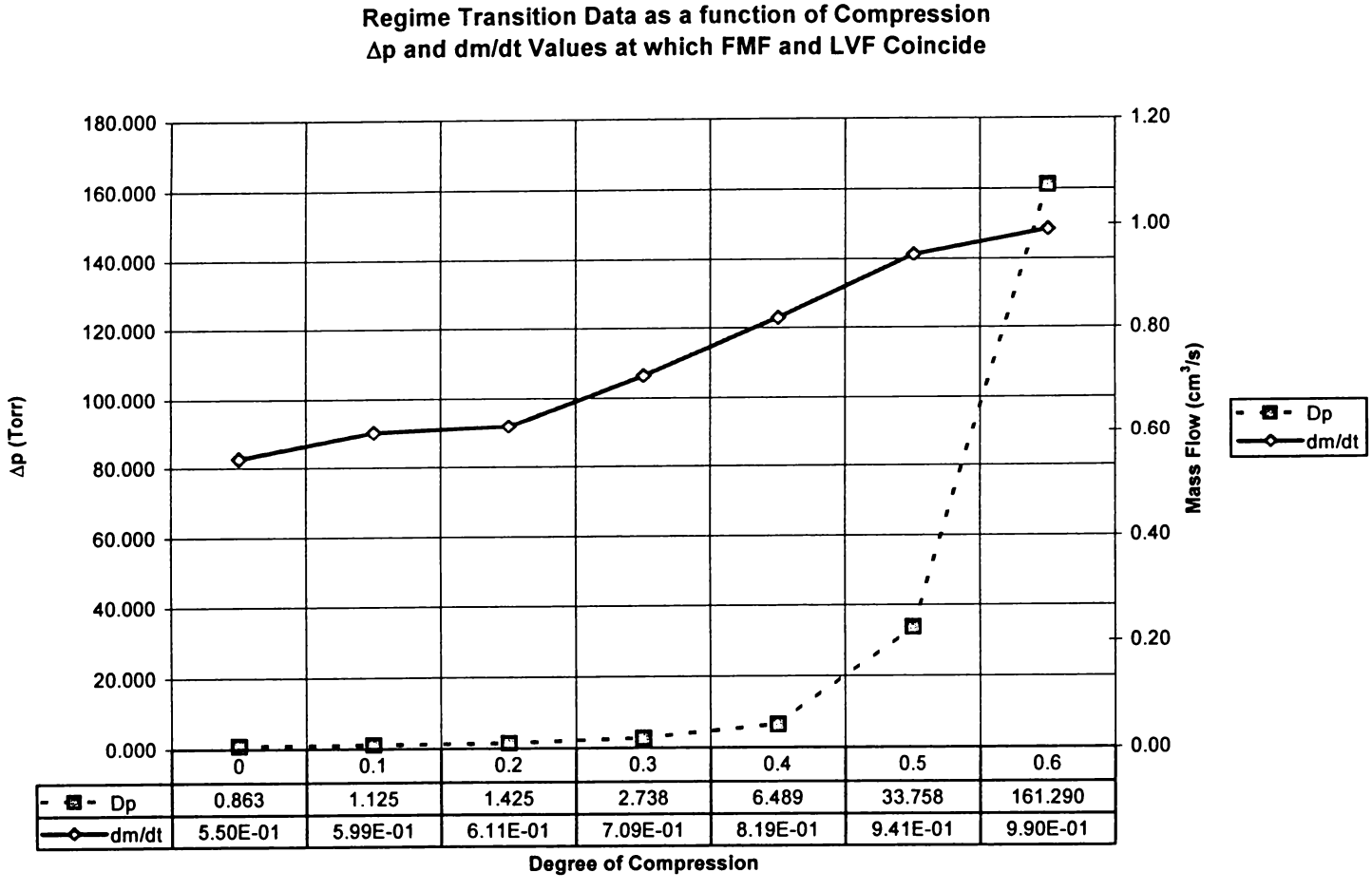

Figure 3.1. Theoretical transition values for mass flow rate, dm/dt, and pressure drop, Δp, at various foam compression levels.

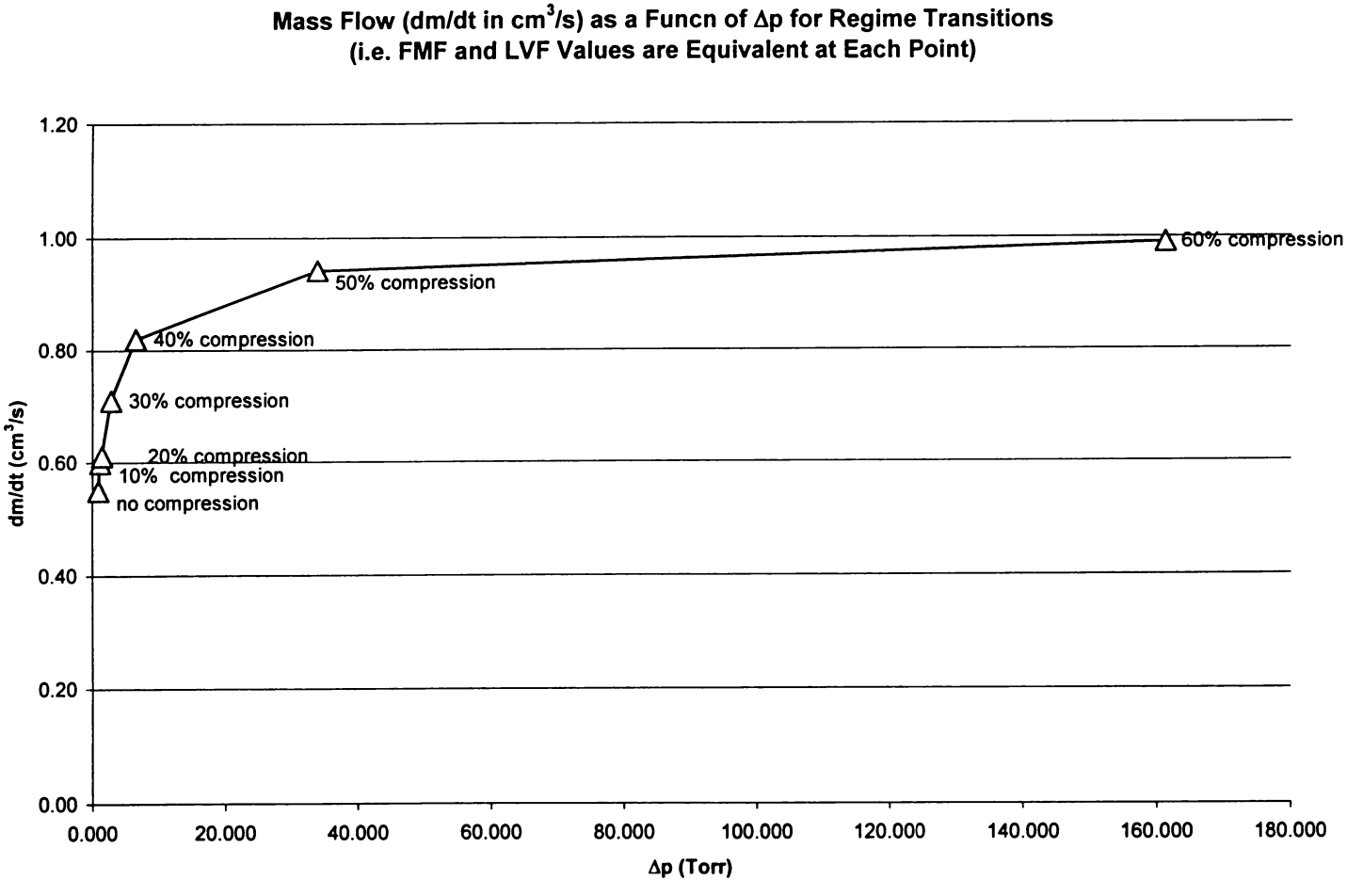

Figure 3.2. Theoretical regime transition curve describing compression levels at Δp-dm/dt regime crossover points.

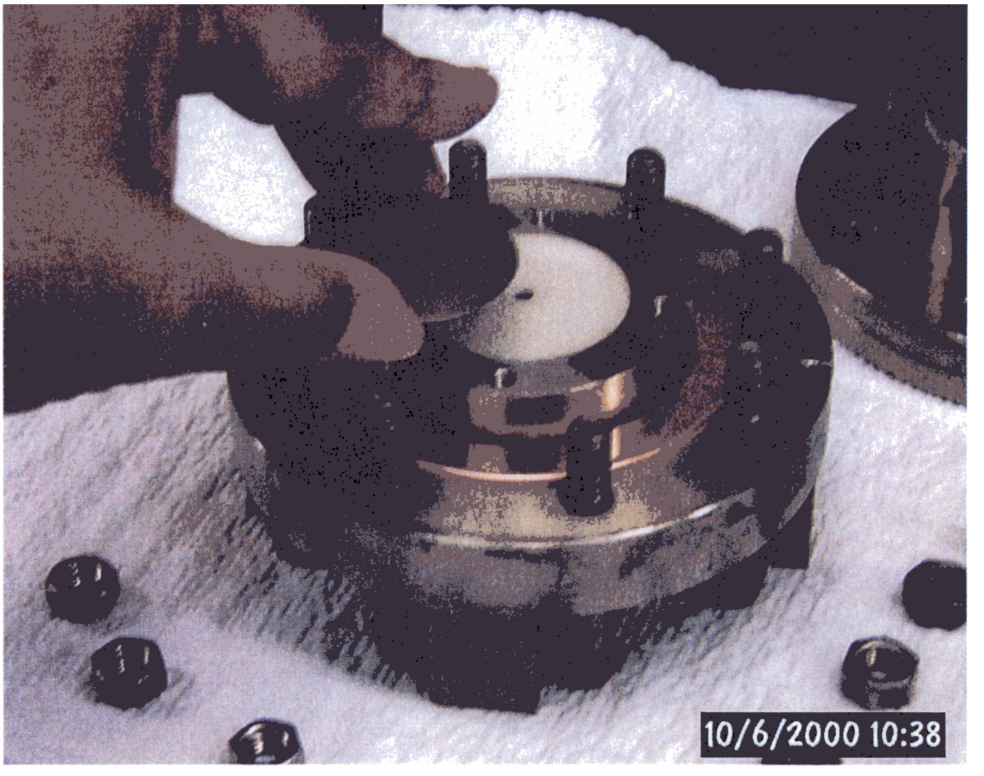

Figure 3.3. Specimen chamber with compression shim being placed on foam specimen.

SKETCH of GAS FLOW SYSTEM

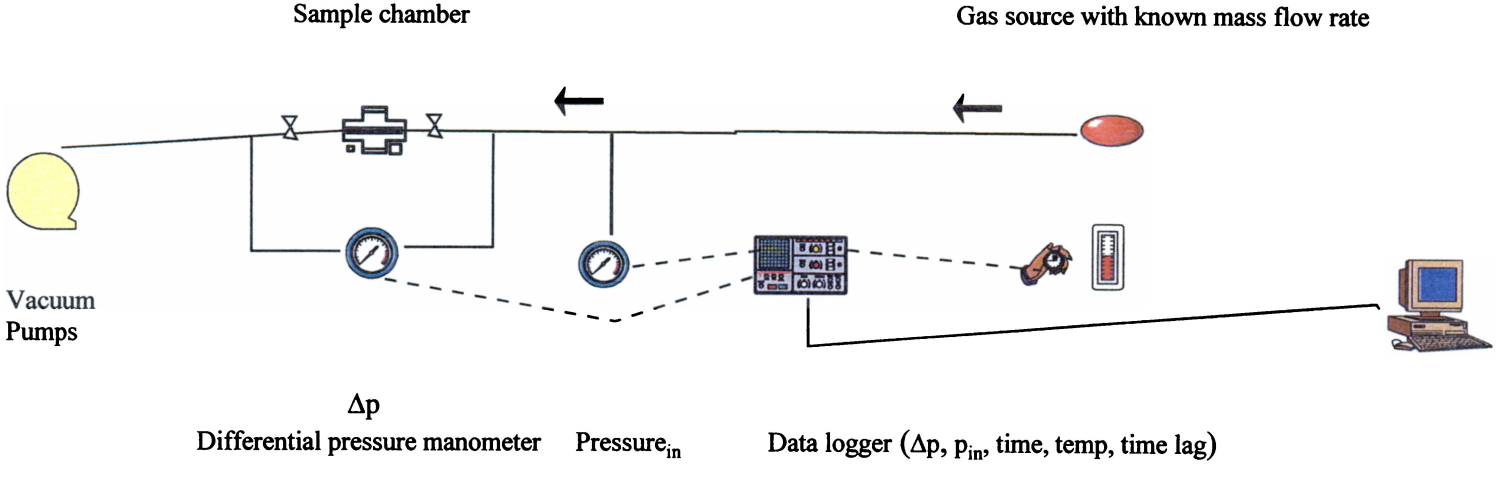

Figure 3.4. Diagram of gas flow measurement system for determination of incoming gas pressure p_{in}, and pressure drop across the specimen Δp, as a function of mass flow rate dm/dt, and time. Temperature is also measured.

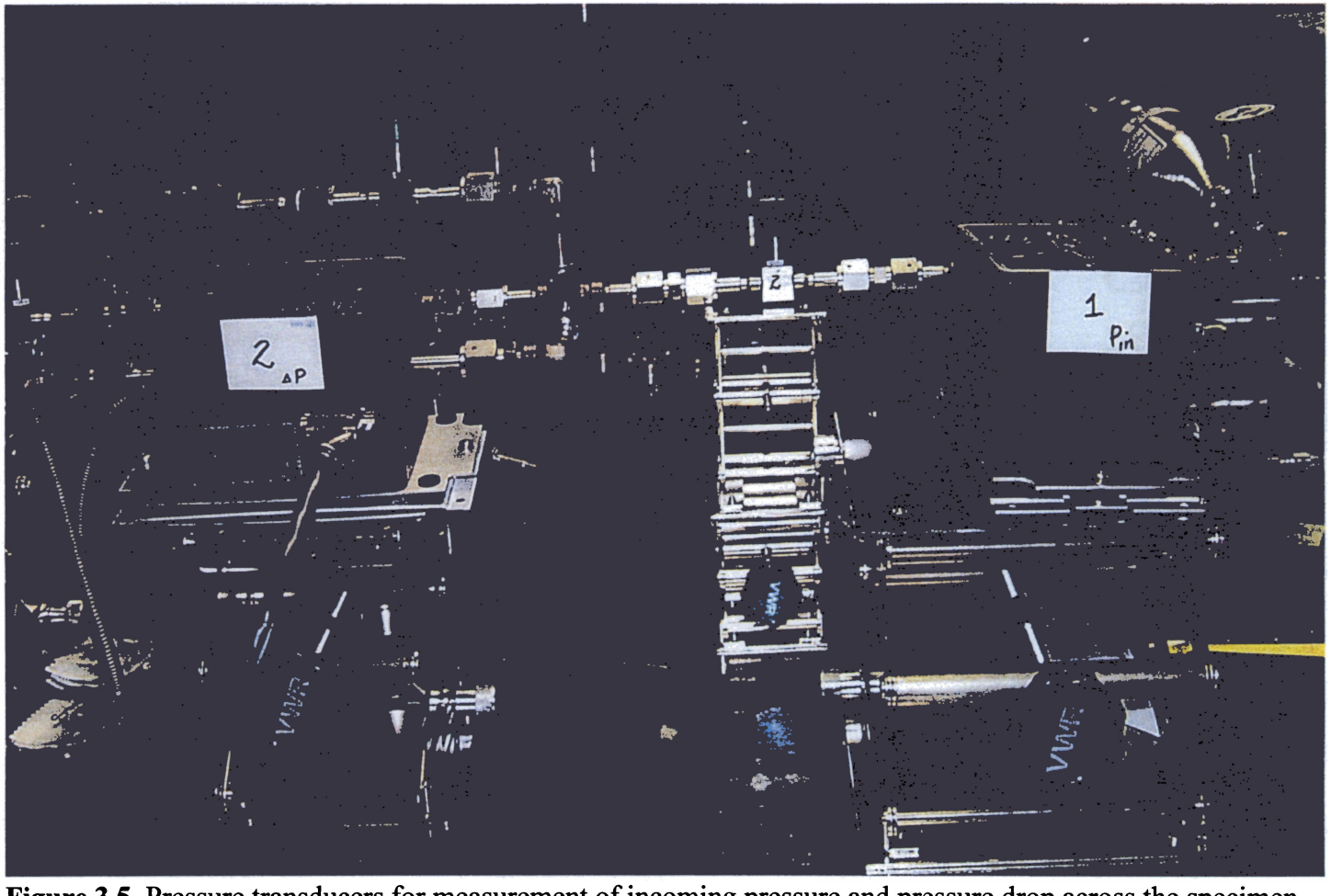

Figure 3.5. Pressure transducers for measurement of incoming pressure and pressure drop across the specimen. Gas source is a calibrated leak, seen in upper right-hand corner of photograph.

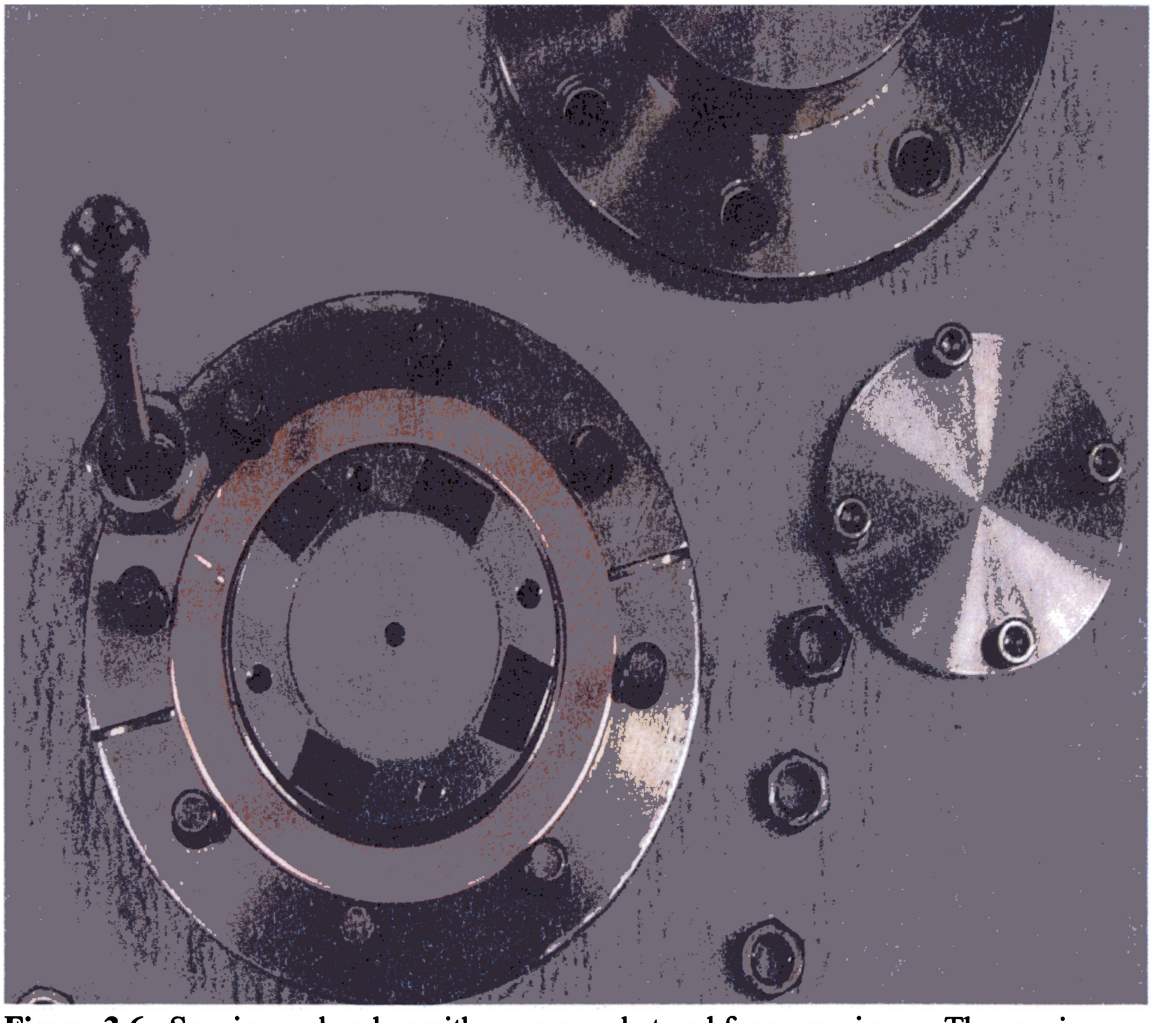

Figure 3.6. Specimen chamber with copper gasket and foam specimen. The specimen cover bolts in four locations and chamber bolts in eight locations. Gas flows radially from the center of the specimen outward.

Gas Transport Experiment Datasheet

Date _____ Time_____ Filename(s)_____

Gas Type _____ M#_____ Program Net Name_____

Gas Flow Rate_____(circle units) cm^3/s torr-lit/s kg/s mol/s sccm H_2 sccm N_2

Specimen ID_____in_____cm/mm Resin _____

Specimen OD_____in_____cm/mm Resin Density ρ_____g/cm^3

Specimen Thickness_____in_____cm/mm Foam Density ρ_0_____g/cm^3

Shim Thickness_____in_____cm/mm Porosity n_0 _____

Compression % _____ Compressed Density ρ_1_____g/cm^3

Baratron Range p_{in} _____ Compressed Porosity n_1_____

Baratron Range Δp _____ Test Points _____

Comments _____

time	p_{in} Torr	$p_{in} - p_{out}$ Δp (Torr)	p_{out} Torr	p_{HV} Torr	p_{pump} Torr	Notes

Figure 3.7. Sample data sheet for collection of experimental information.

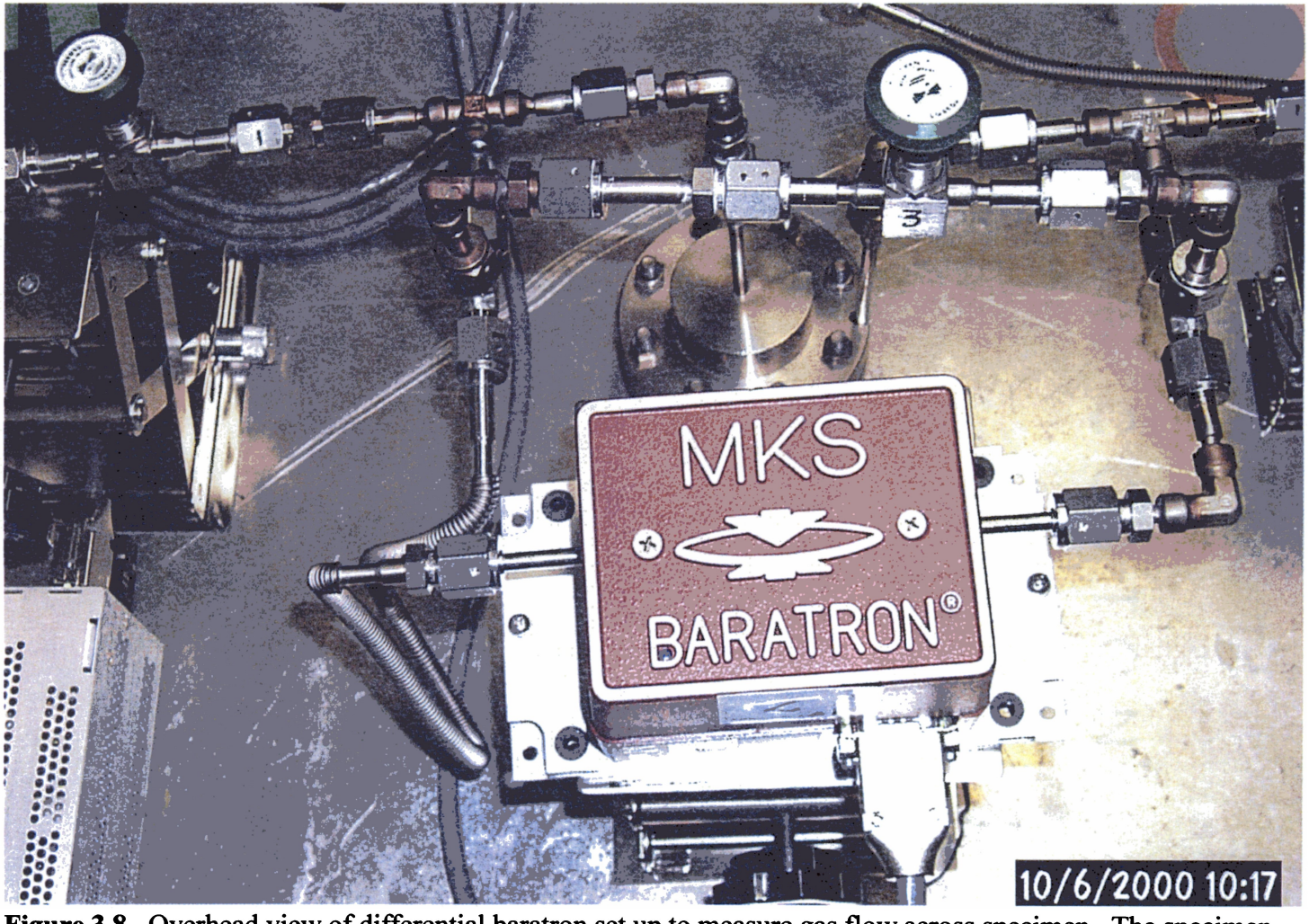

Figure 3.8. Overhead view of differential baratron set up to measure gas flow across specimen. The specimen chamber is seen behind the pressure gage. Valve #3 across upstream and downstream arms of gage, and Valve #4 to vacuum pumps are also visible in this photograph.

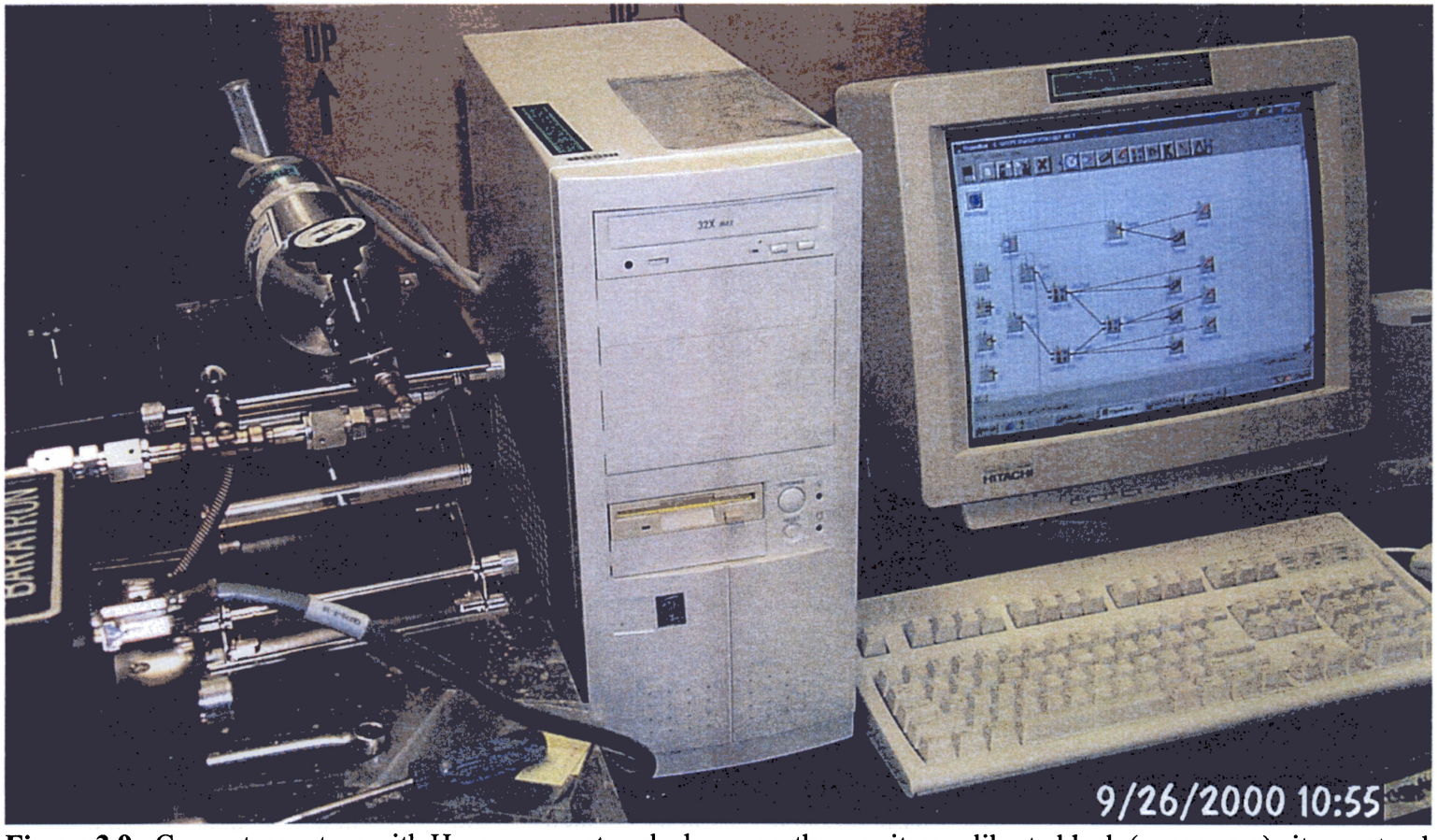

Figure 3.9. Computer system with Hyperware network shown on the monitor; calibrated leak (gas source) sits on stand to left of computer.

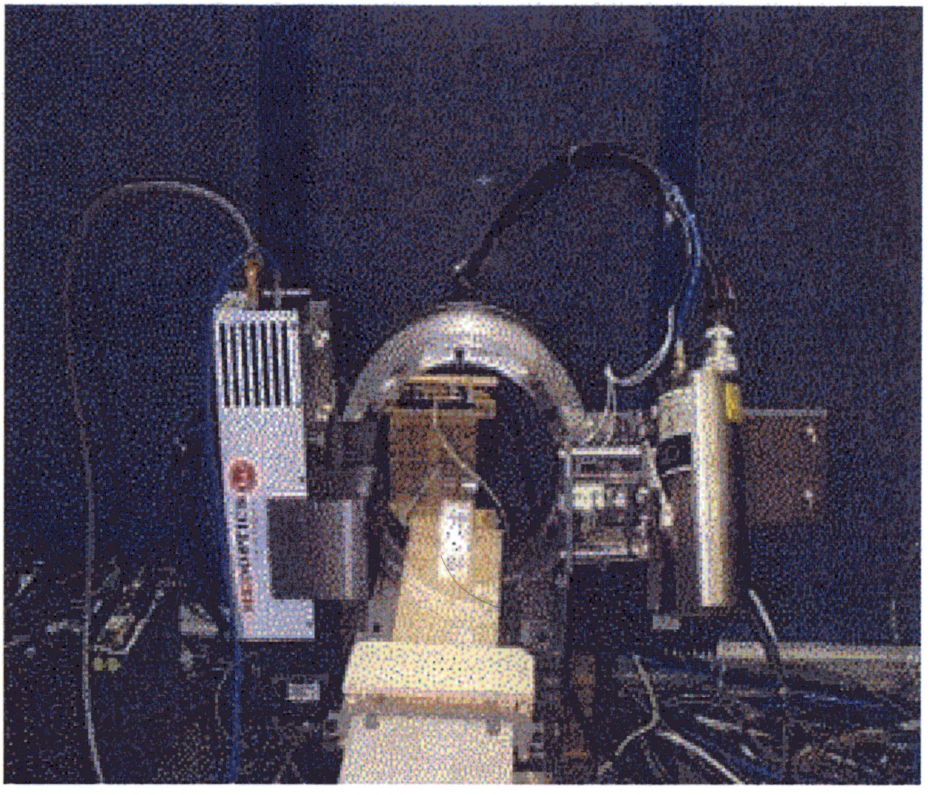

Figure 3.10. Photograph of MicroCAT x-ray analyzer.
Source: Oak Ridge National Laboratory website address http://www.ic.ornl.gov/rd-groups/msd/Projects/Microcat_Web/main_datacq.htm .

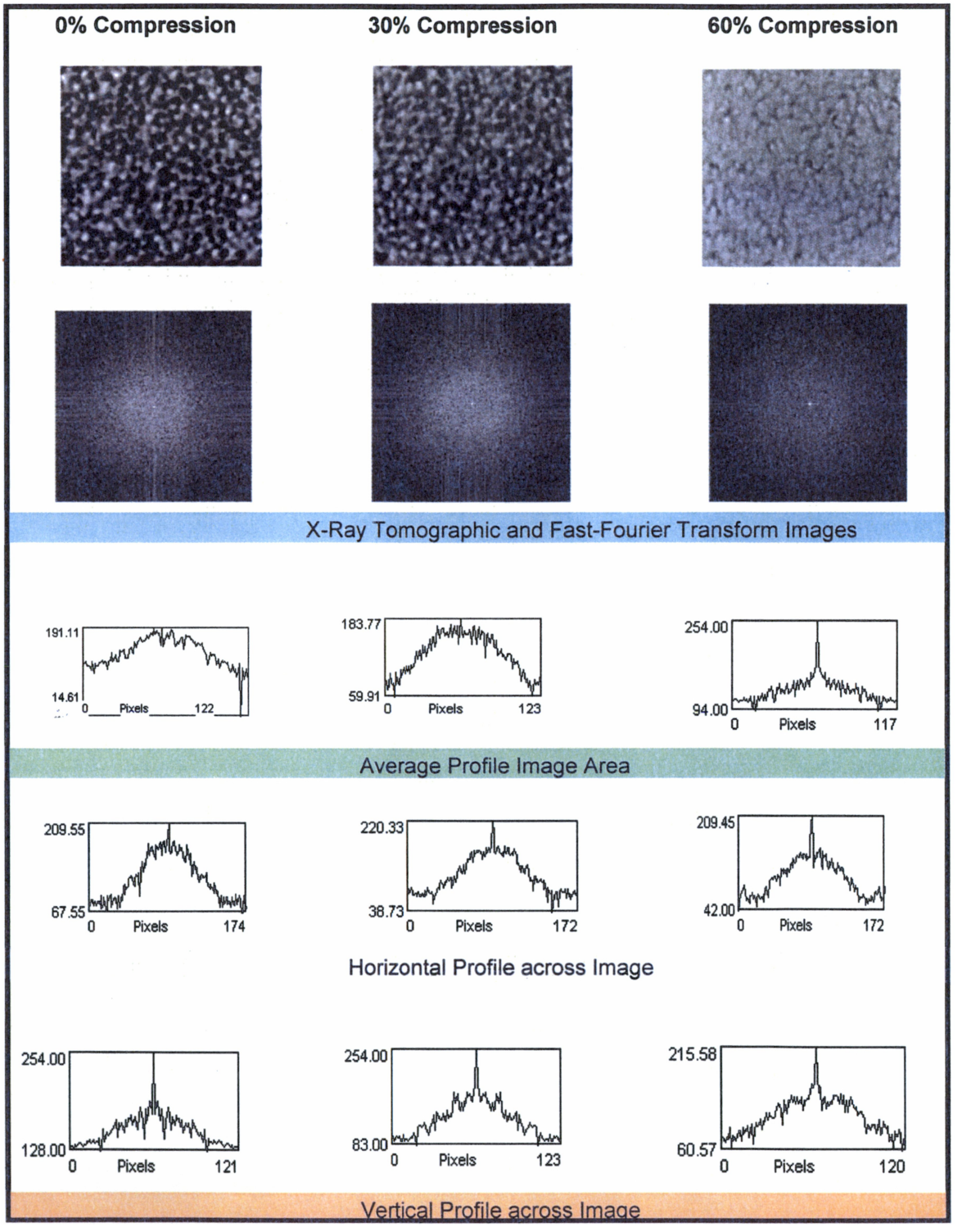

Figure 3.11. X-Ray Tomography Profiles of Fourier Transform Images of Compressed Polydimethylsiloxane Foam (0.615 g/cm^3 Density; Initial Porosity of 0.483).

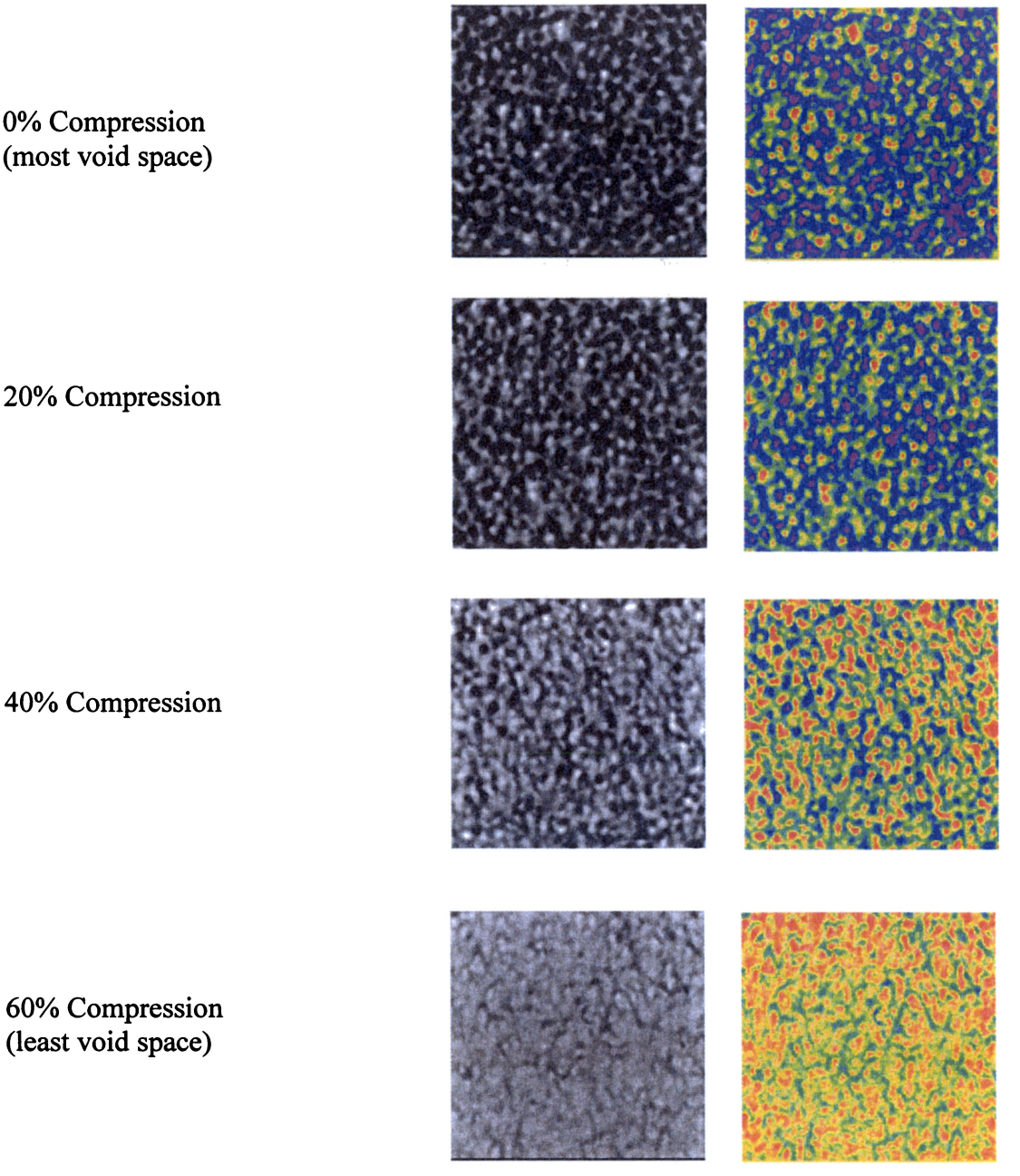

Figure 3.12. Sample of x-ray tomography images from compressed polysiloxane foam specimens. Black and white images are cross-sections through samples, where lighter shading of gray indicates high attenuation (polymer). Color images are 32-color software enhanced, with purple/blue shades indicating void space and red where attenuation is highest.

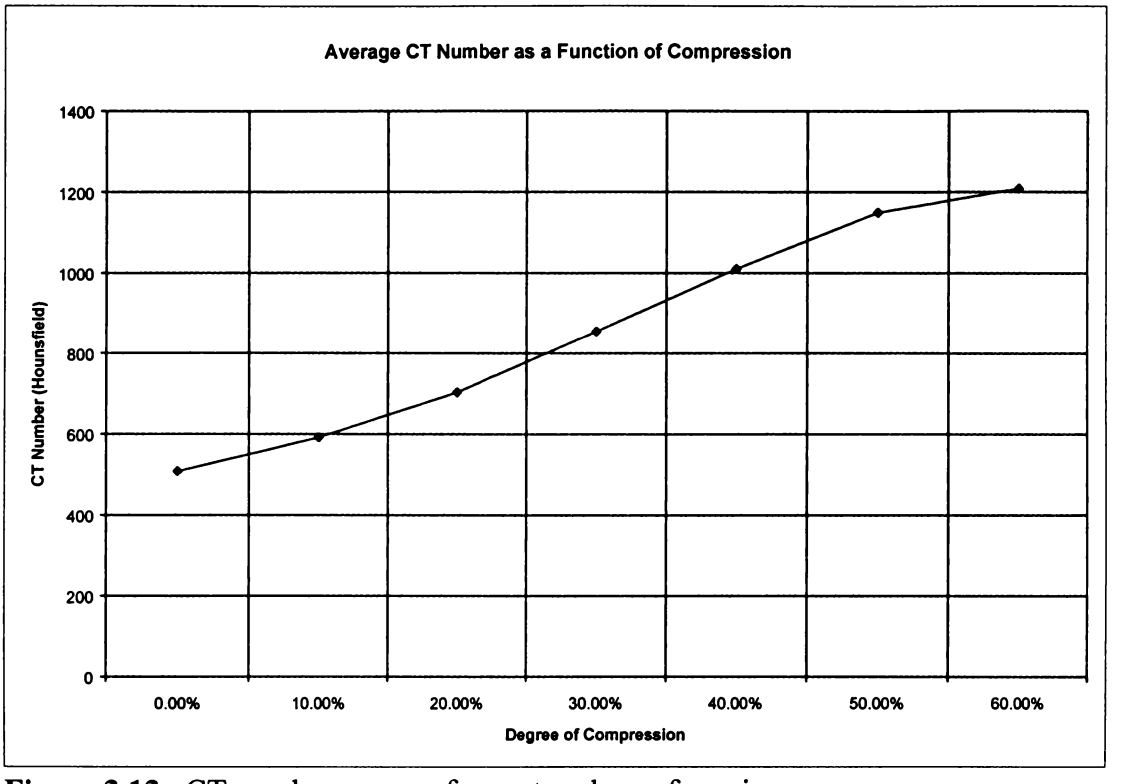

Figure 3.13. CT number average for center plane of specimens.

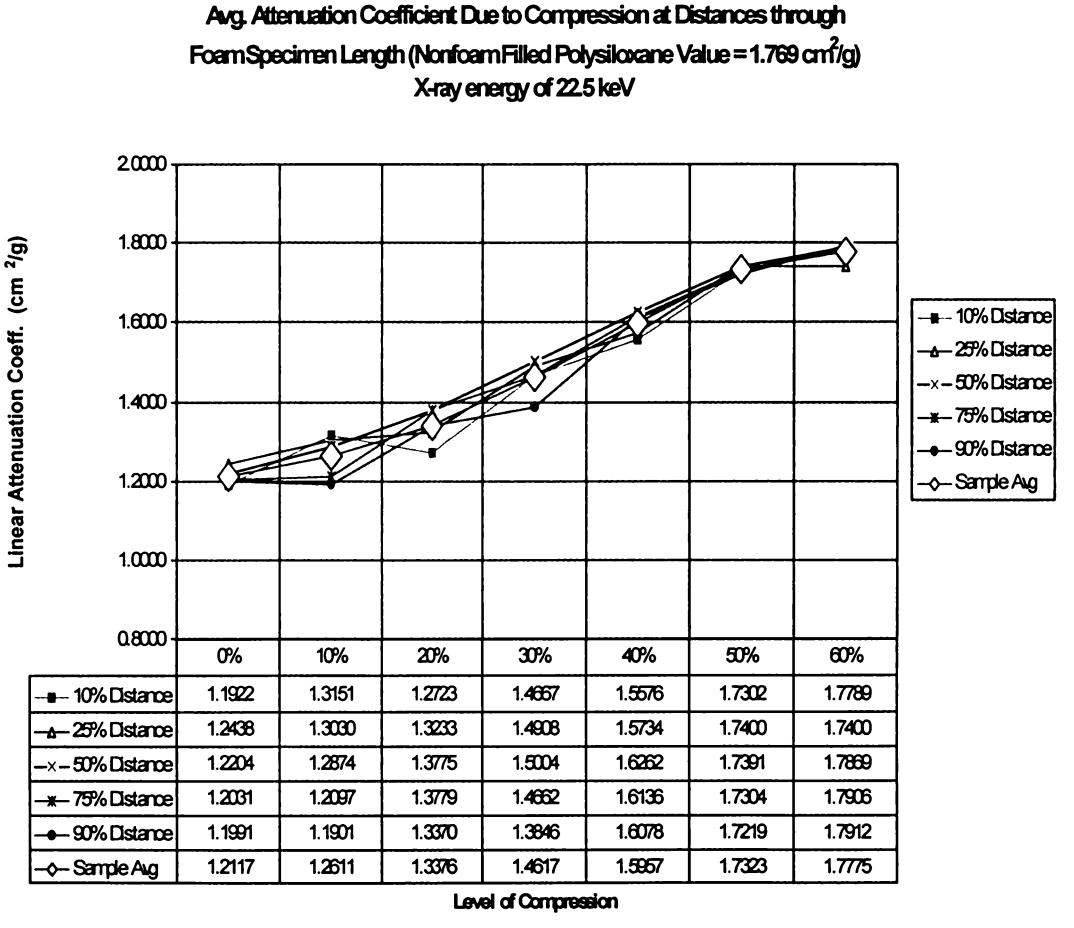

	0%	10%	20%	30%	40%	50%	60%
10% Distance	1.1922	1.3151	1.2723	1.4657	1.5576	1.7302	1.7789
25% Distance	1.2438	1.3030	1.3233	1.4908	1.5734	1.7400	1.7400
50% Distance	1.2204	1.2874	1.3775	1.5004	1.6262	1.7391	1.7869
75% Distance	1.2031	1.2097	1.3779	1.4662	1.6136	1.7304	1.7906
90% Distance	1.1991	1.1901	1.3370	1.3846	1.6078	1.7219	1.7912
Sample Avg	1.2117	1.2611	1.3376	1.4617	1.5957	1.7323	1.7775

Figure 3.14. Positional X-ray mass attenuation data at compressions from 0 to 60 percent.

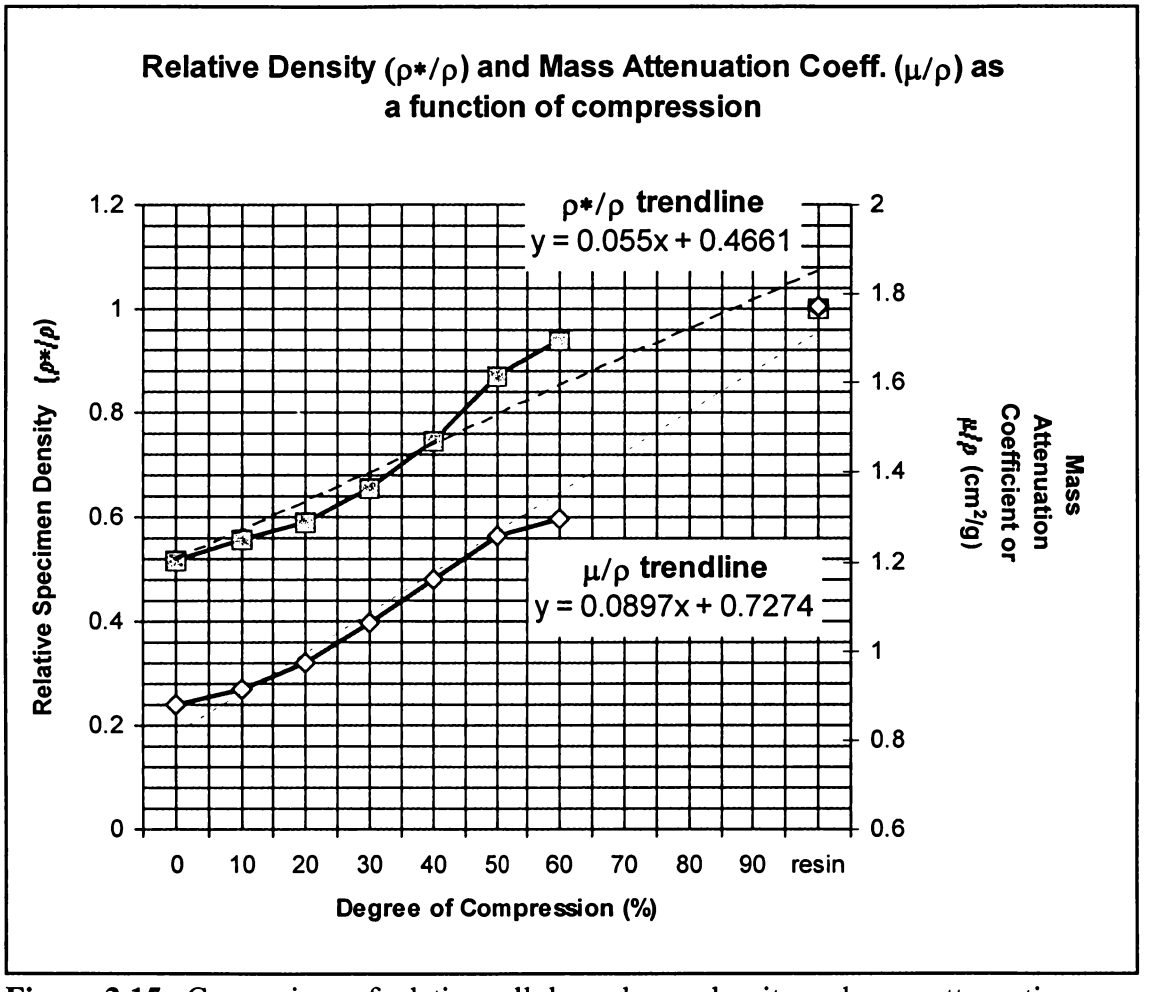

Figure 3.15. Comparison of relative cellular polymer density and mass attenuation coefficient for 22.5 keV x-rays, as foam is compressed. Straight lines project values for solid polymer as the 100% compressed foam.

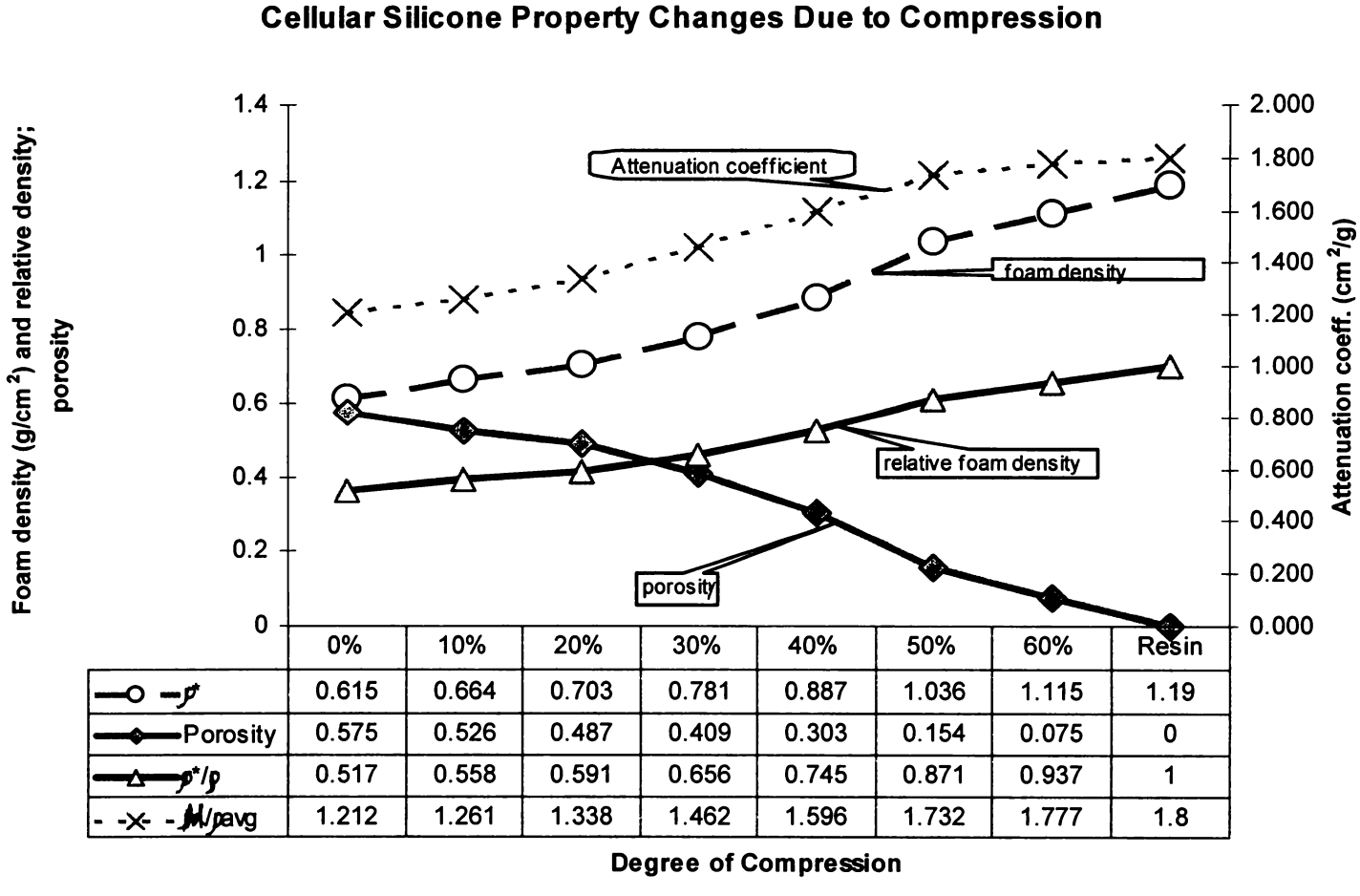

	0%	10%	20%	30%	40%	50%	60%	Resin
—○— ρ*	0.615	0.664	0.703	0.781	0.887	1.036	1.115	1.19
—◆— Porosity	0.575	0.526	0.487	0.409	0.303	0.154	0.075	0
—△— ρ*/ρ	0.517	0.558	0.591	0.656	0.745	0.871	0.937	1
- -×- - μ/ρavg	1.212	1.261	1.338	1.462	1.596	1.732	1.777	1.8

Figure 3.16. Summary of cellular foam characteristics with mechanical compression, including foam density, ρ*, relative foam density, ρ*/ρ and porosity (left abscissa); mass attenuation of 22.5 keV x-rays (right abscissa).

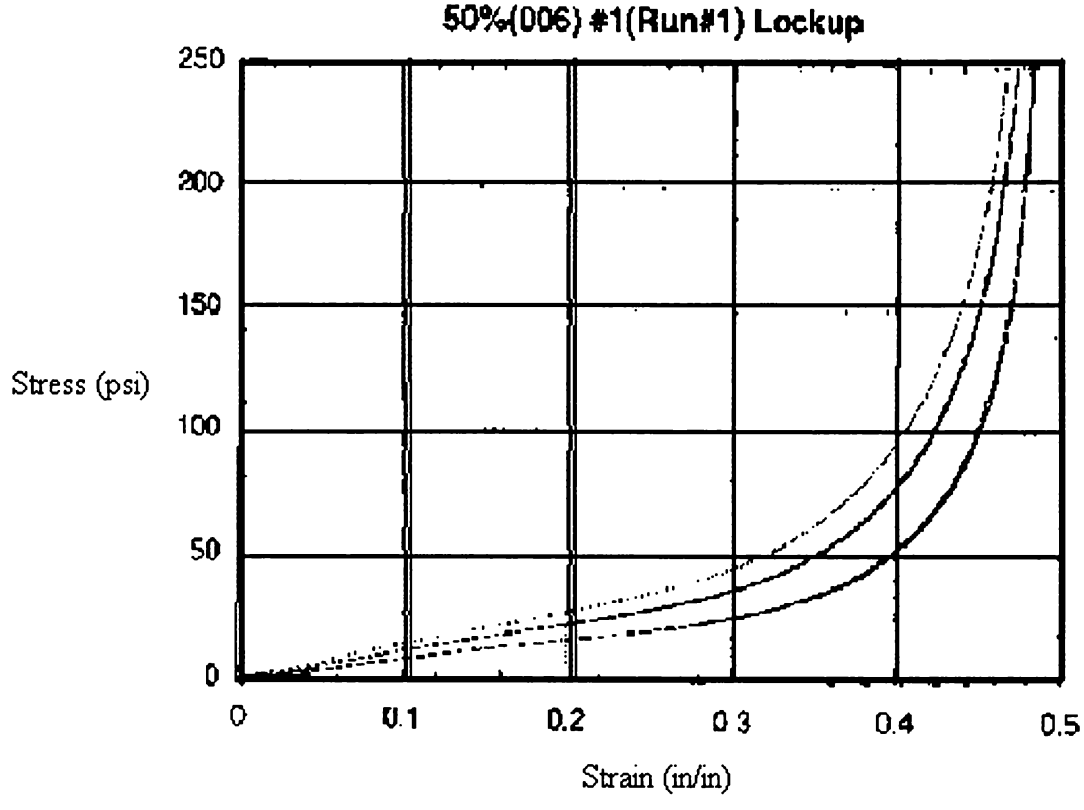

Figure 3.17. Experimental curve for compressive properties of 50% porosity polysiloxane foam. *Source: S. DeTeresa, Lawrence Livermore National Laboratory, 2001.*

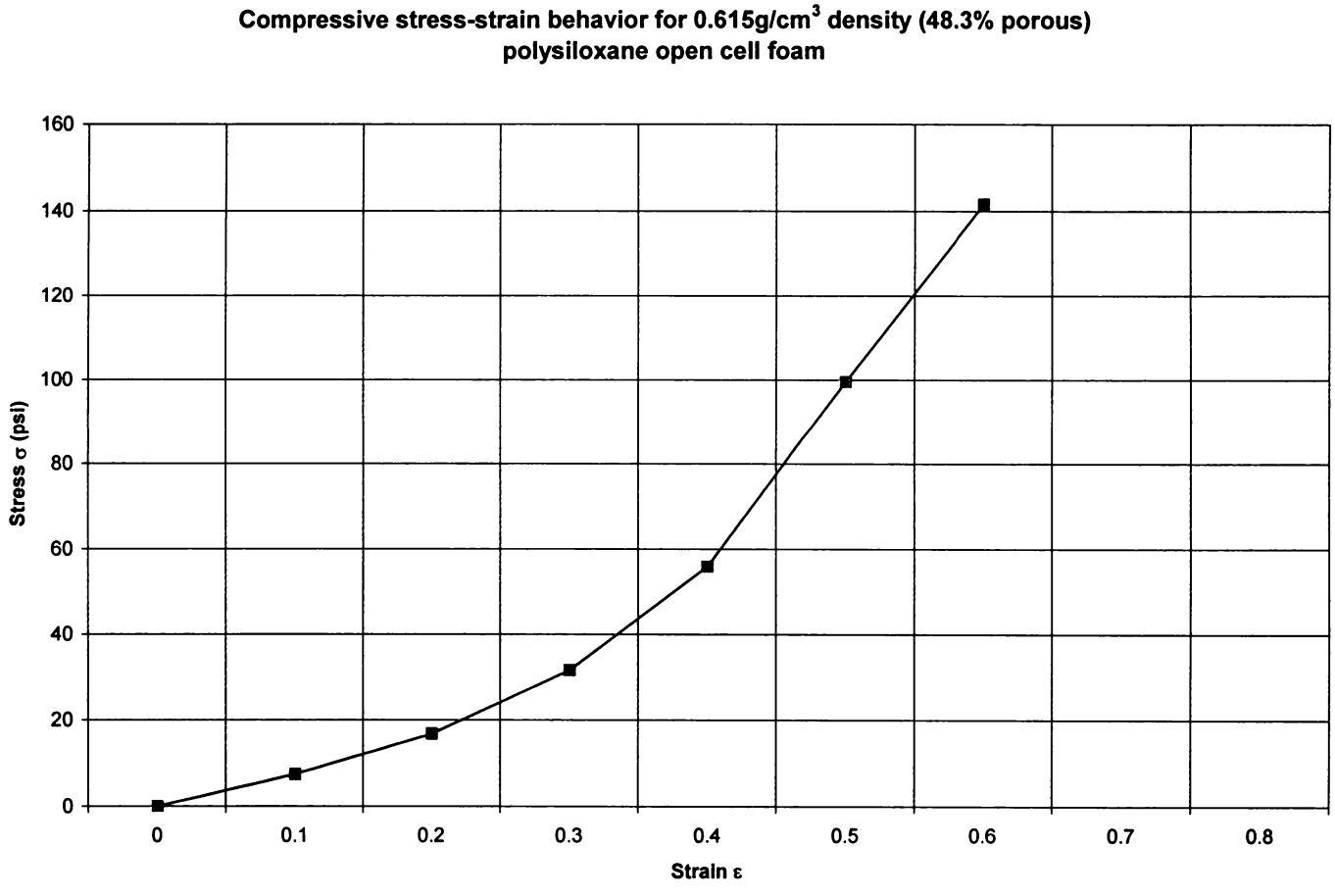

Figure 3.18. Calculated stress-strain curve for compression using tomography data.

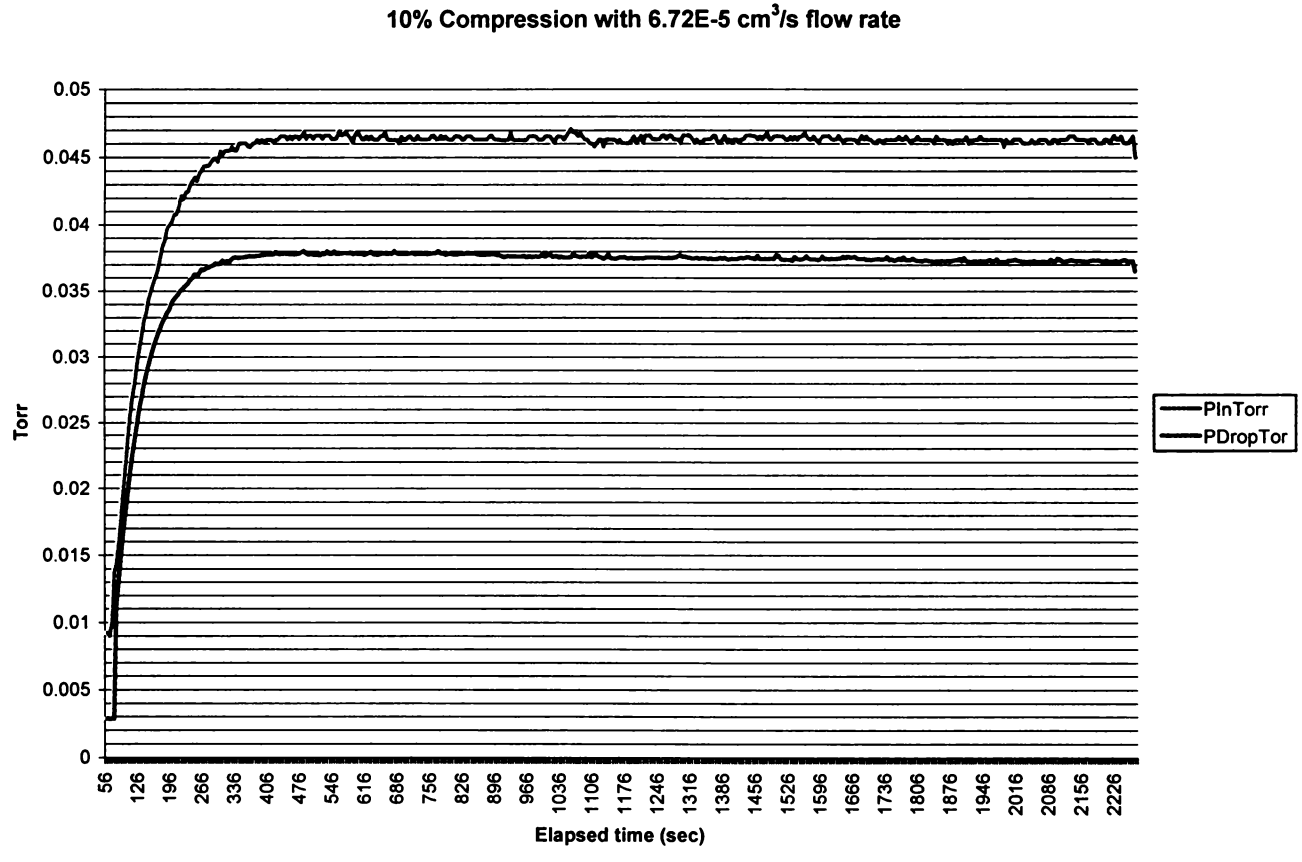

Figure 3.19. Typical data collection plot for gas flow through compressed polysiloxane foam. Note approach to steady-state pressure values for incoming pressure and pressure differential across specimen, $\Delta p = p_{in} - p_{out}$.

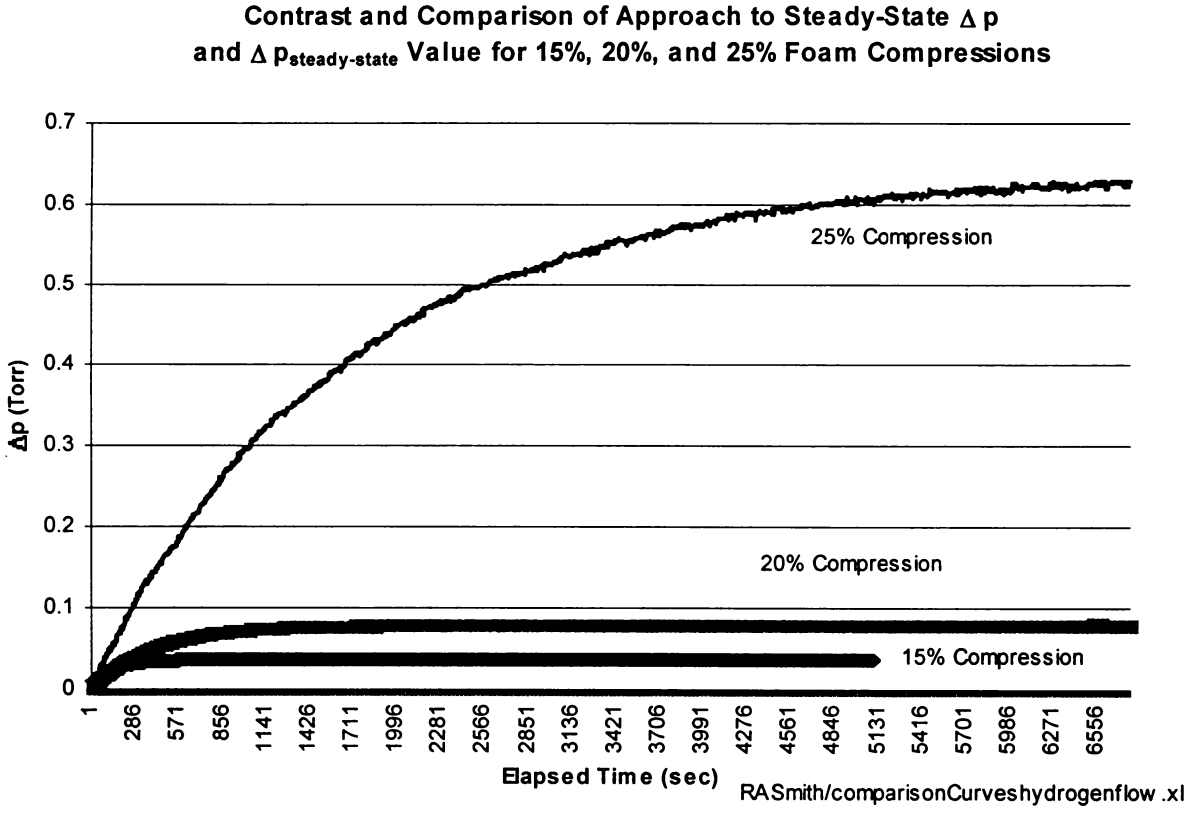

Figure 3.20. Comparison of Δp curves as a function of foam compression.

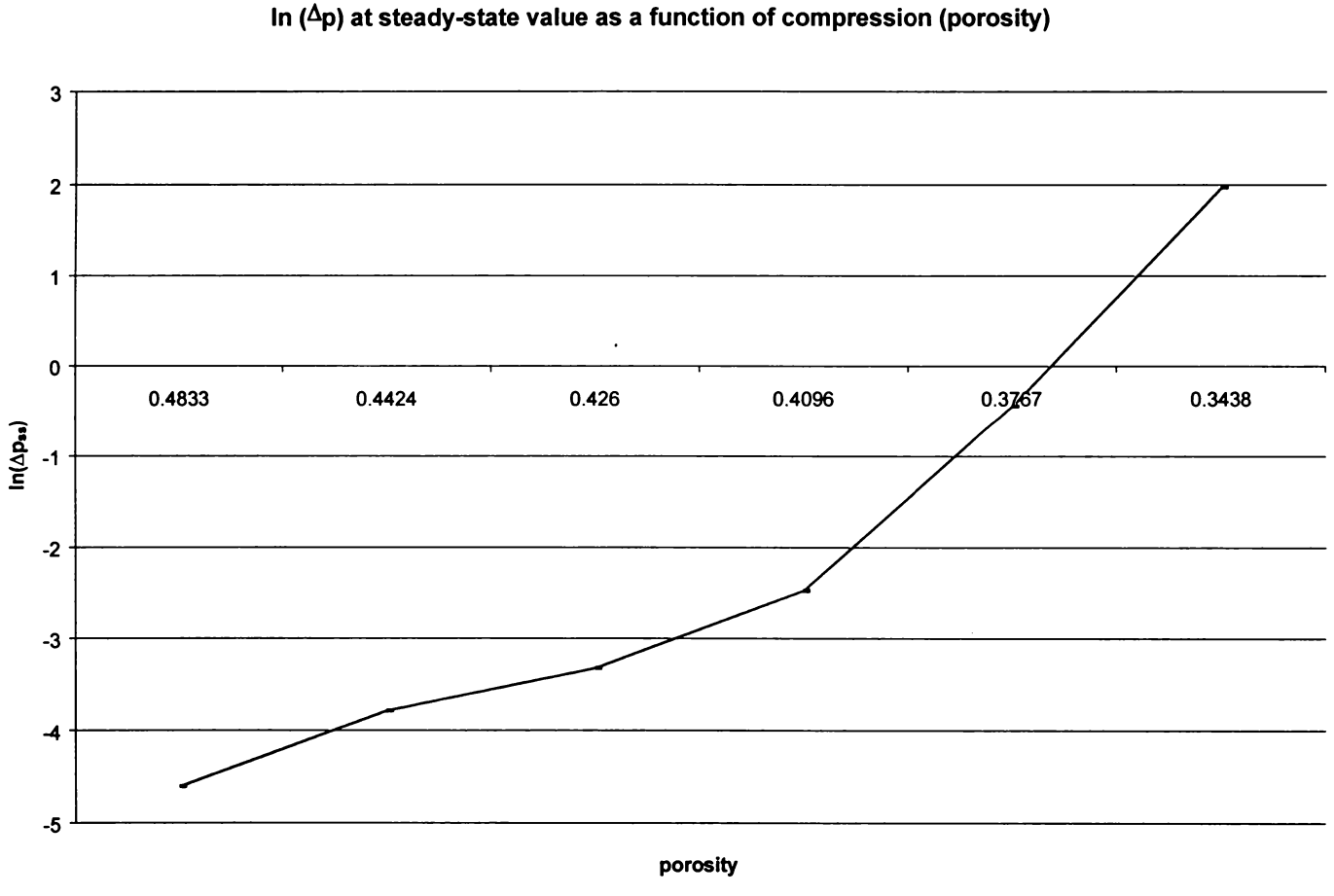

Figure 3.21. Logarithmic plot of steady-state pressure drop (Δp_{ss}) at each foam porosity. Each porosity value is directly due to compression.

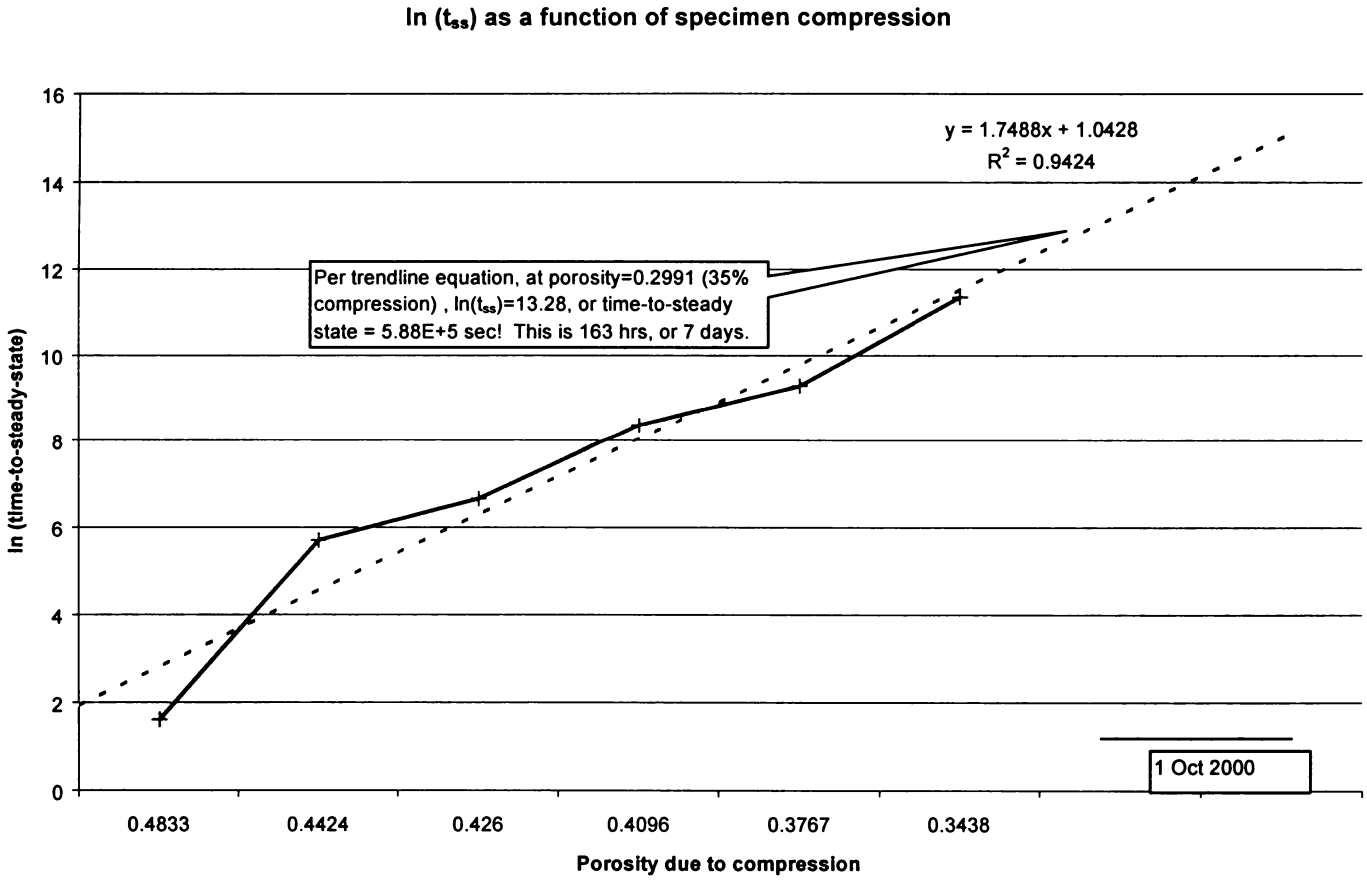

Figure 3.22. Logarithmic plot of time-to-reach-steady-state pressure drop (t_{ss}) at each foam porosity. Each porosity value is directly due to compression. Regression analysis trendline predicts t_{ss} at further compressions, using a linear equation fit for data collected.

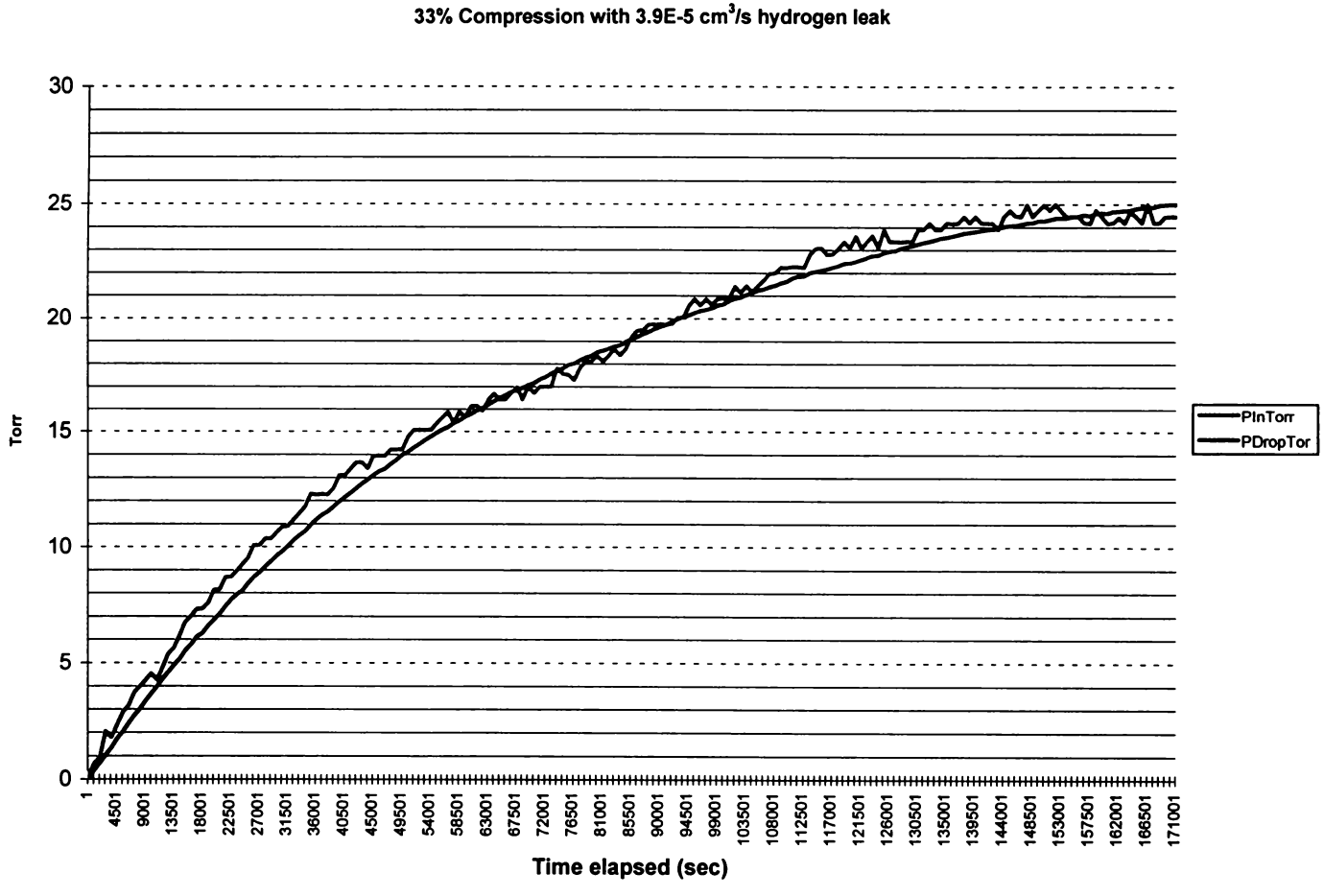

Figure 3.23. Pressure data from 33% compressed foam specimen. Note lengthened approach to steady-state values for p_{in} and Δp (test was ended after two days).

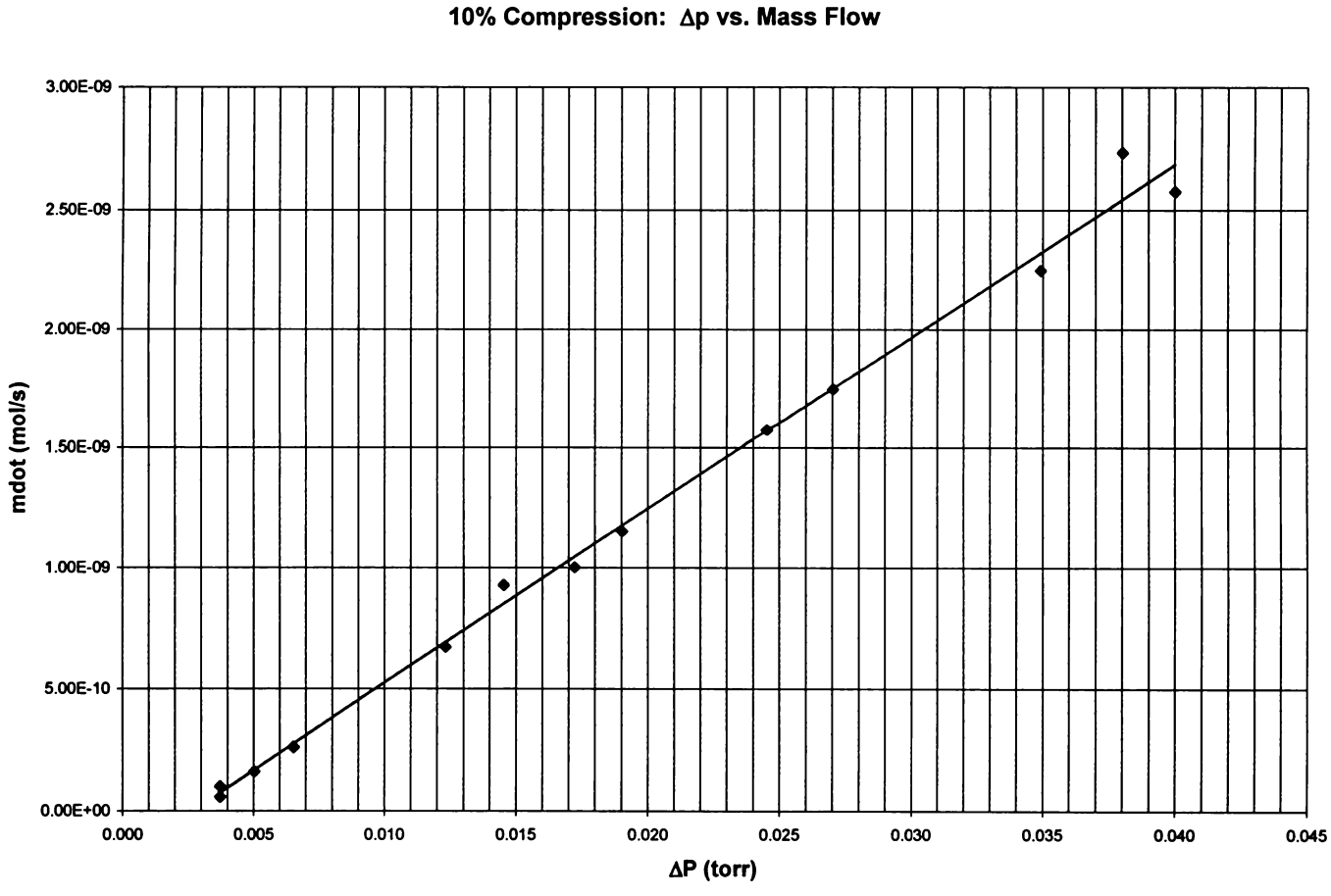

Figure 3.24. Plot of mass flow rates, dm/dt vs. plateau or steady-state Δp values for 10% compressed polysiloxane foam.

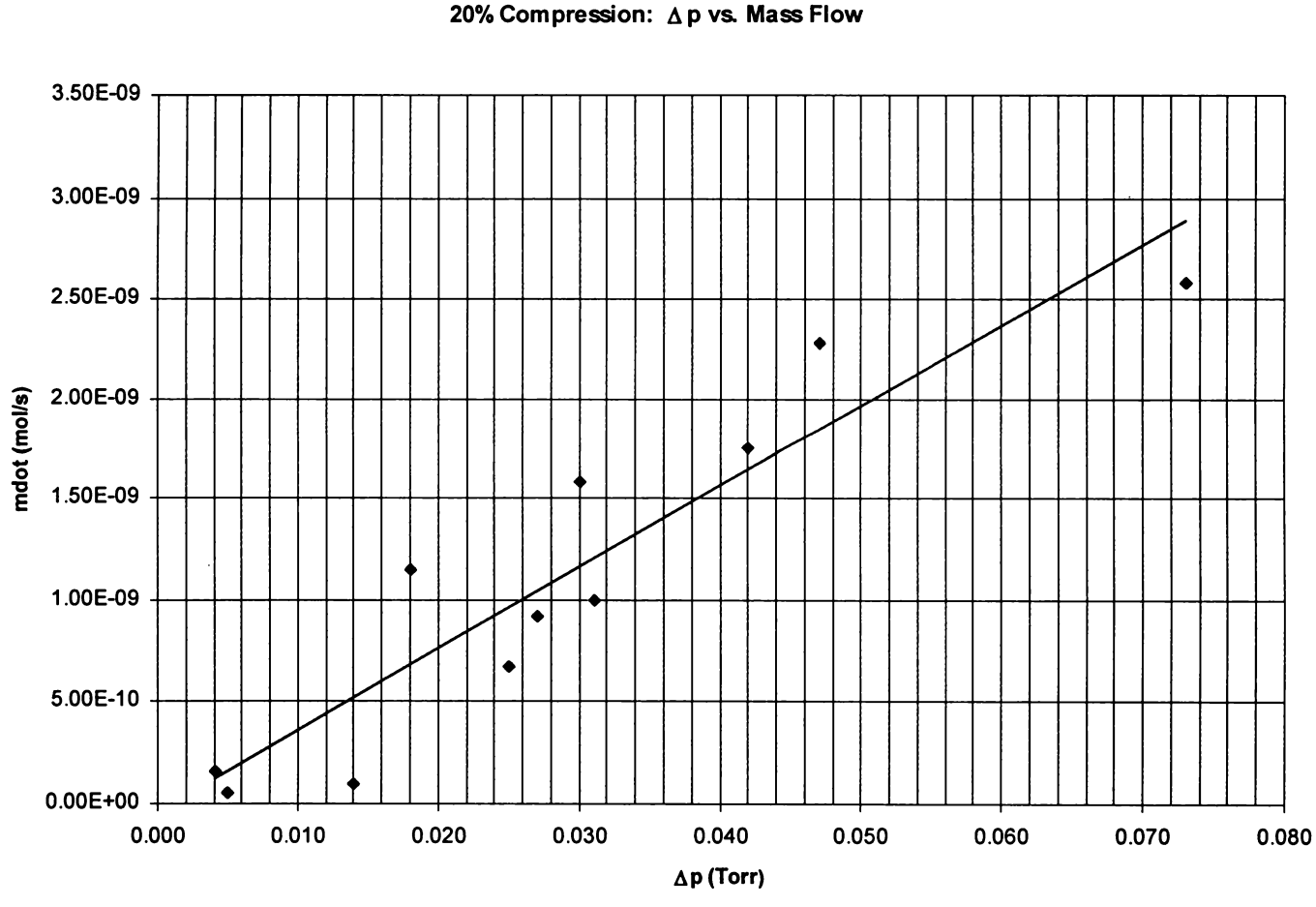

Figure 3.25. Plot of mass flow rates, dm/dt vs. plateau or steady-state Δp values for 20% compressed polysiloxane foam.

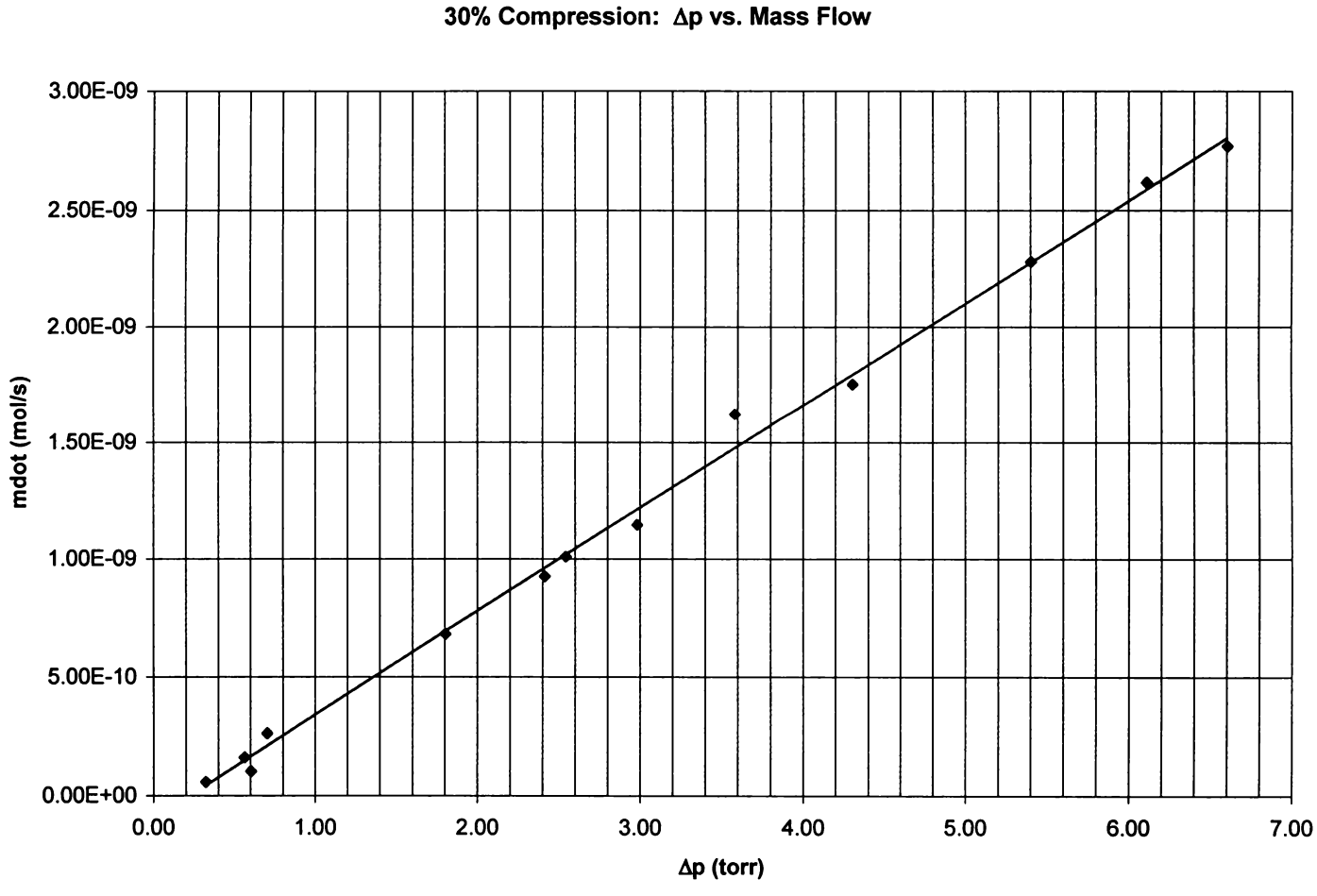

Figure 3.26. Plot of mass flow rates, dm/dt vs. plateau or steady-state Δp values for 30% compressed polysiloxane foam.

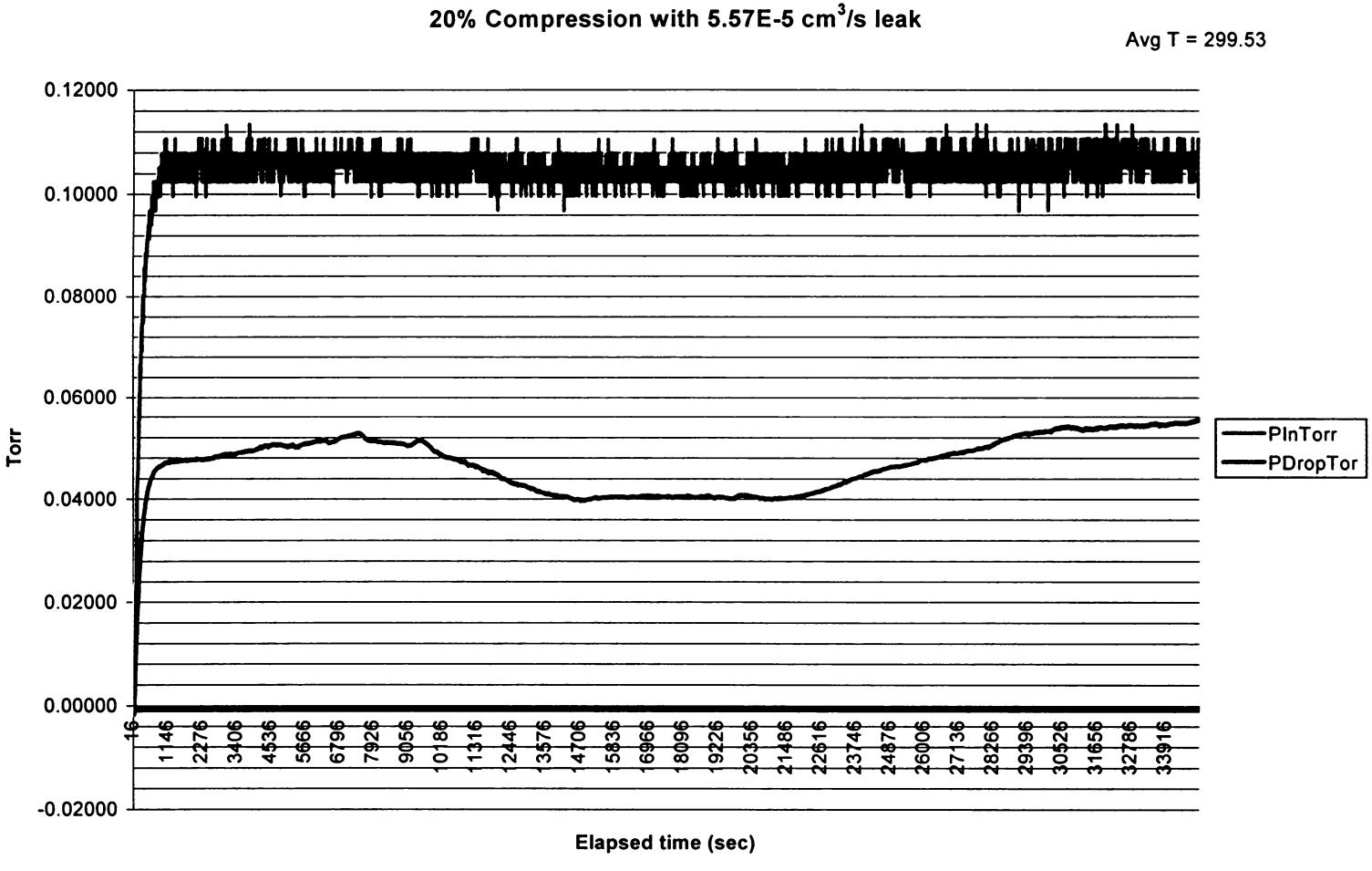

Figure 3.27. Results for flow through 20% compressed polysiloxane foam where Δp at steady-state showed distinct variations due to laboratory temperature changes.

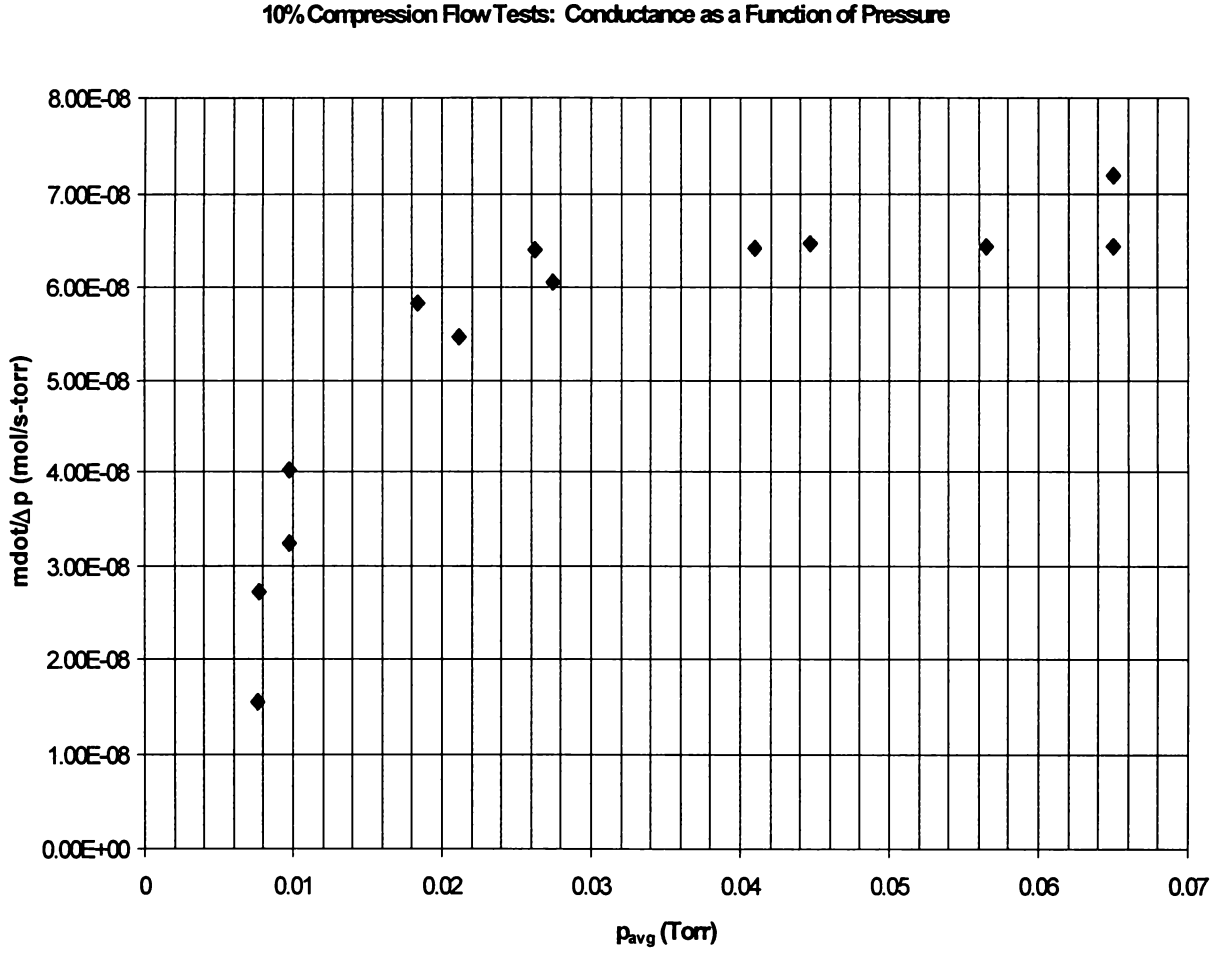

Figure 3.28. Plot of conductance vs. average pressure for 10% compressed foam specimens. Conductance is the ratio of mass flow rate to steady-state pressure drop value.

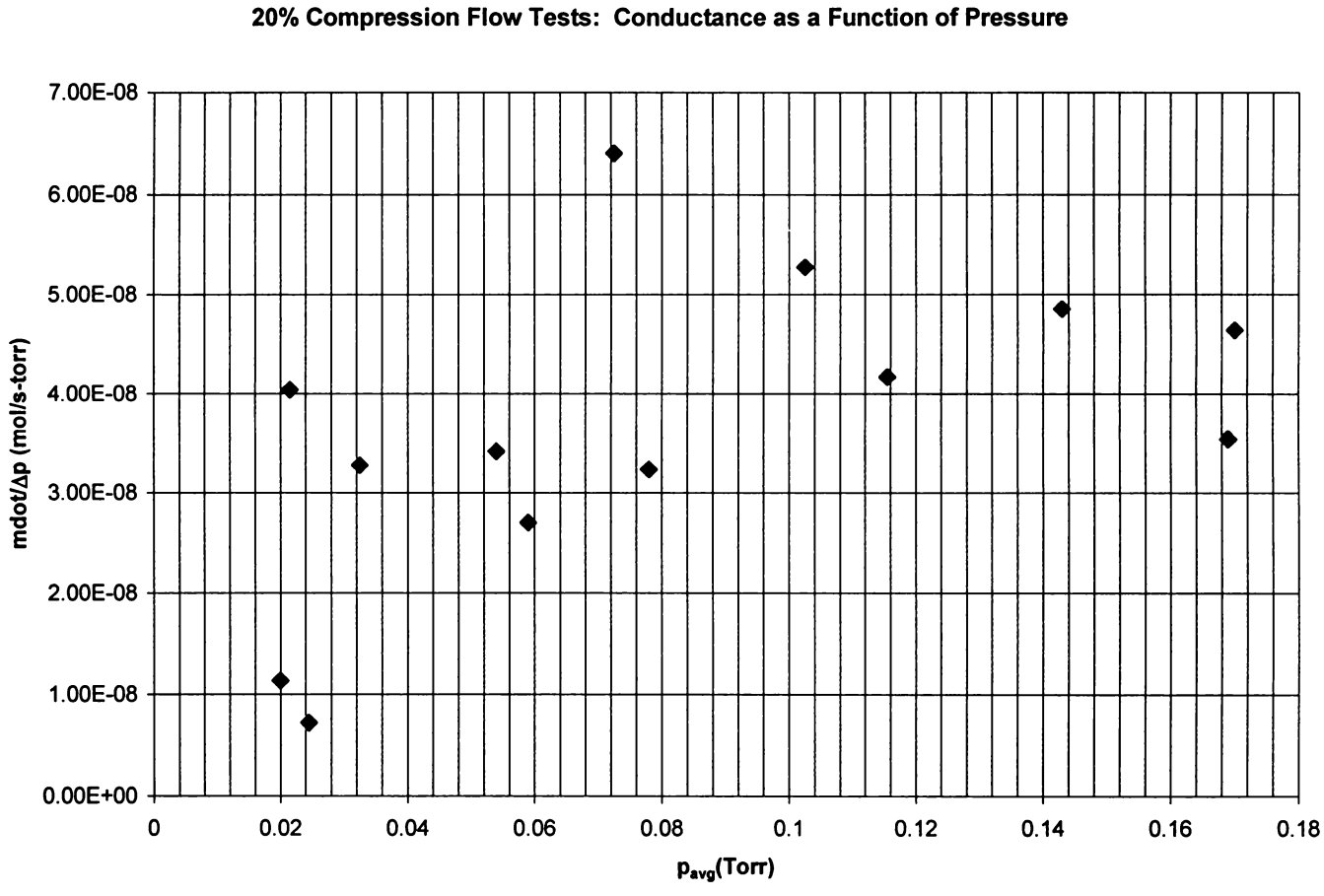

Figure 3.29. Plot of conductance vs. average pressure for 20% compressed foam specimens. Conductance is the ratio of mass flow rate to steady-state pressure drop value. Note wide variances due to temperature effects for this level of foam compression.

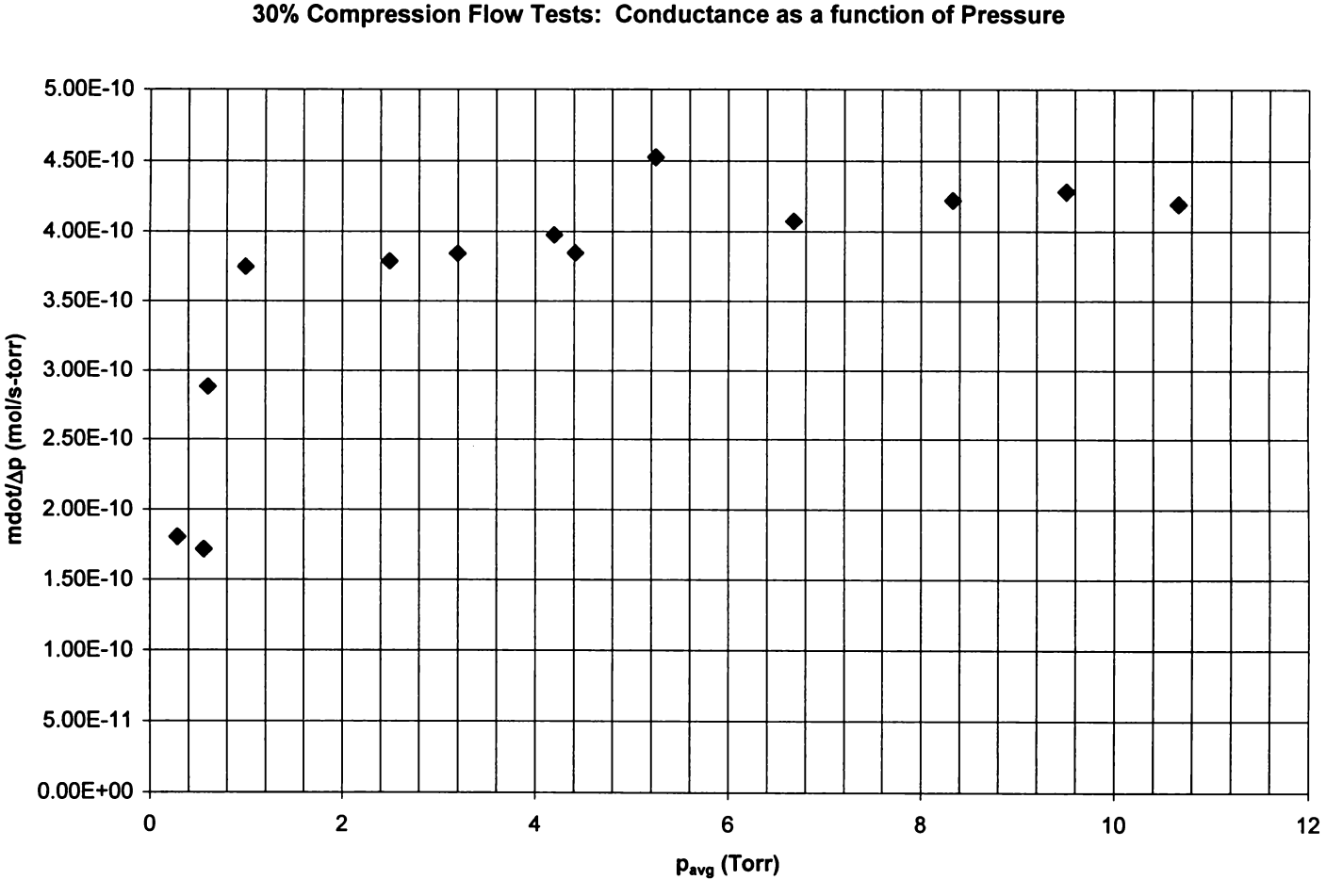

Figure 3.30. Plot of conductance vs. average pressure for 30% compressed foam specimens. Conductance is the ratio of mass flow rate to steady-state pressure drop value.

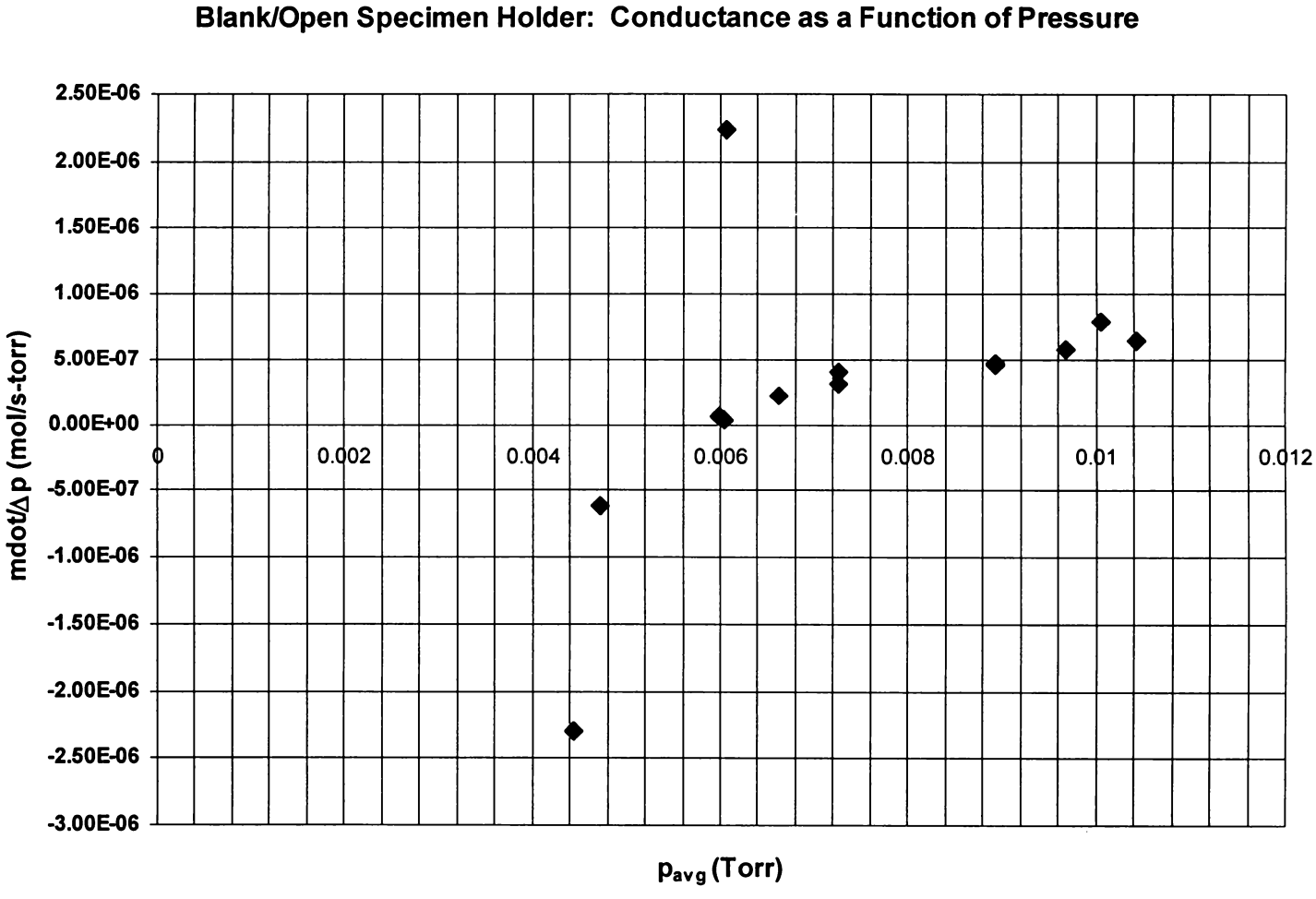

Figure 3.31. Plot of conductance vs. average pressure for an empty specimen container.

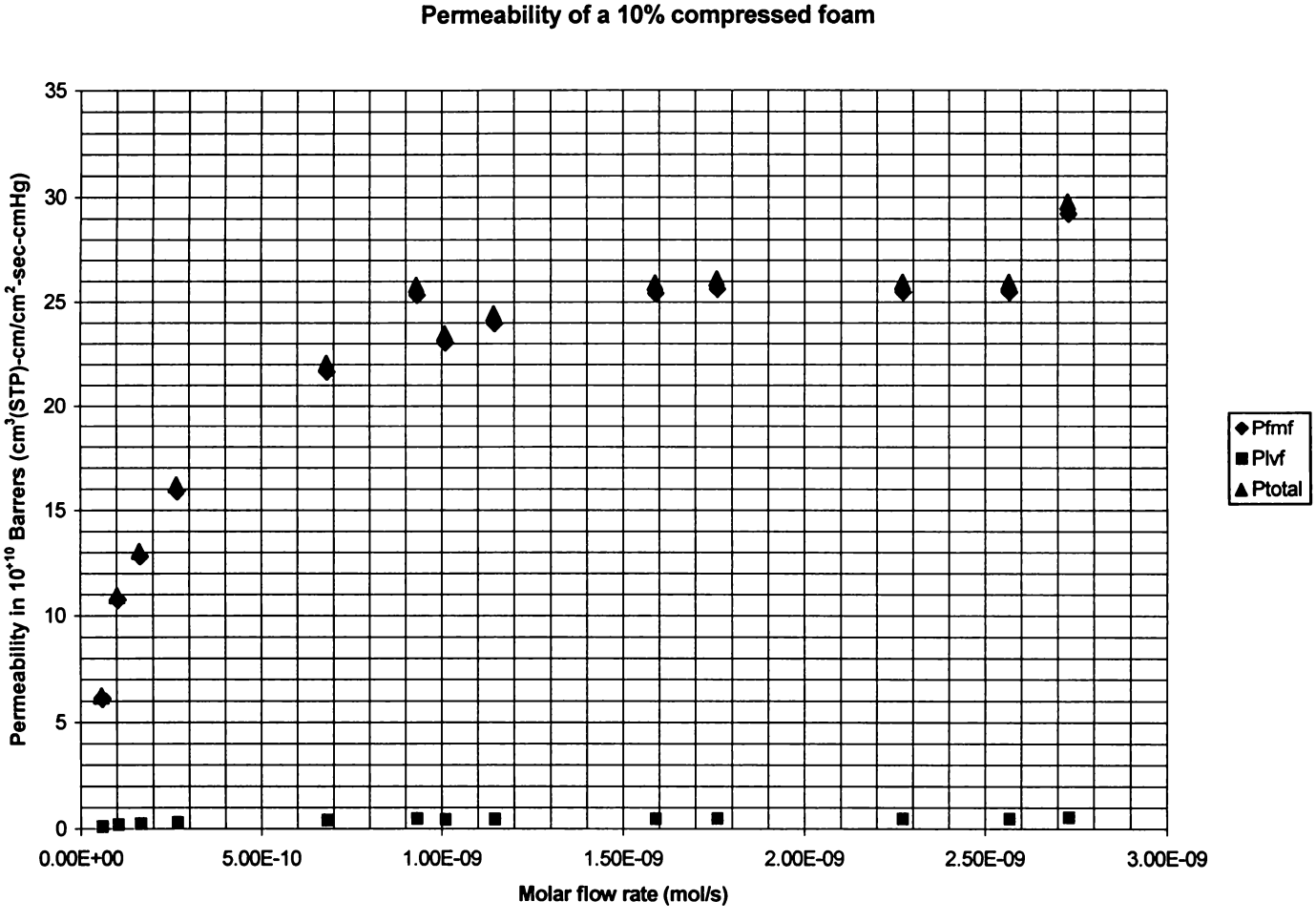

Figure 3.32. Permeability of a 10% compressed polysiloxane foam as a function of gas flow rate. Dominant flow regime is of the free molecular type.

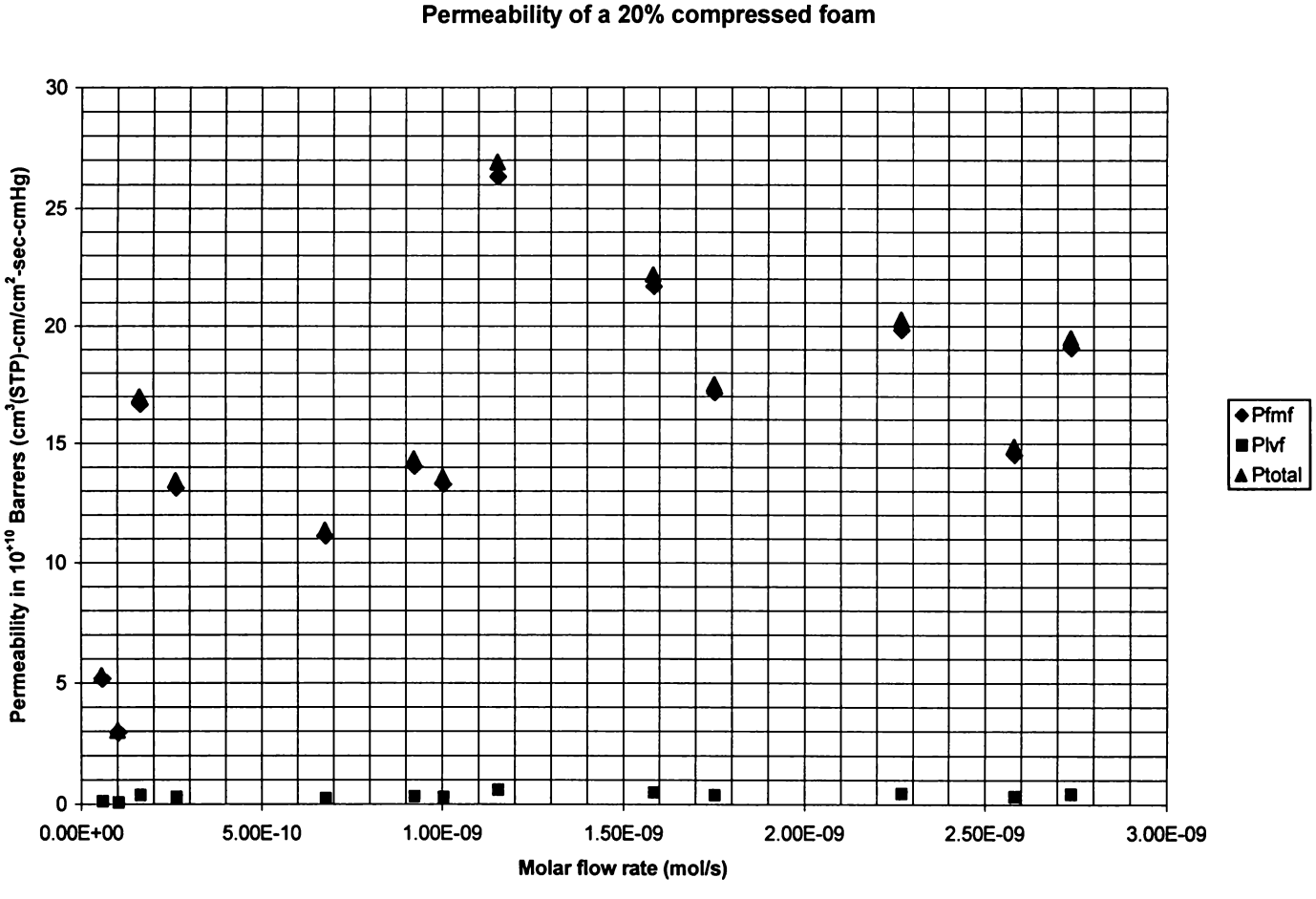

Figure 3.33. Permeability of a 20% compressed polysiloxane foam as a function of gas flow rate. Dominant flow regime is of the free molecular type.

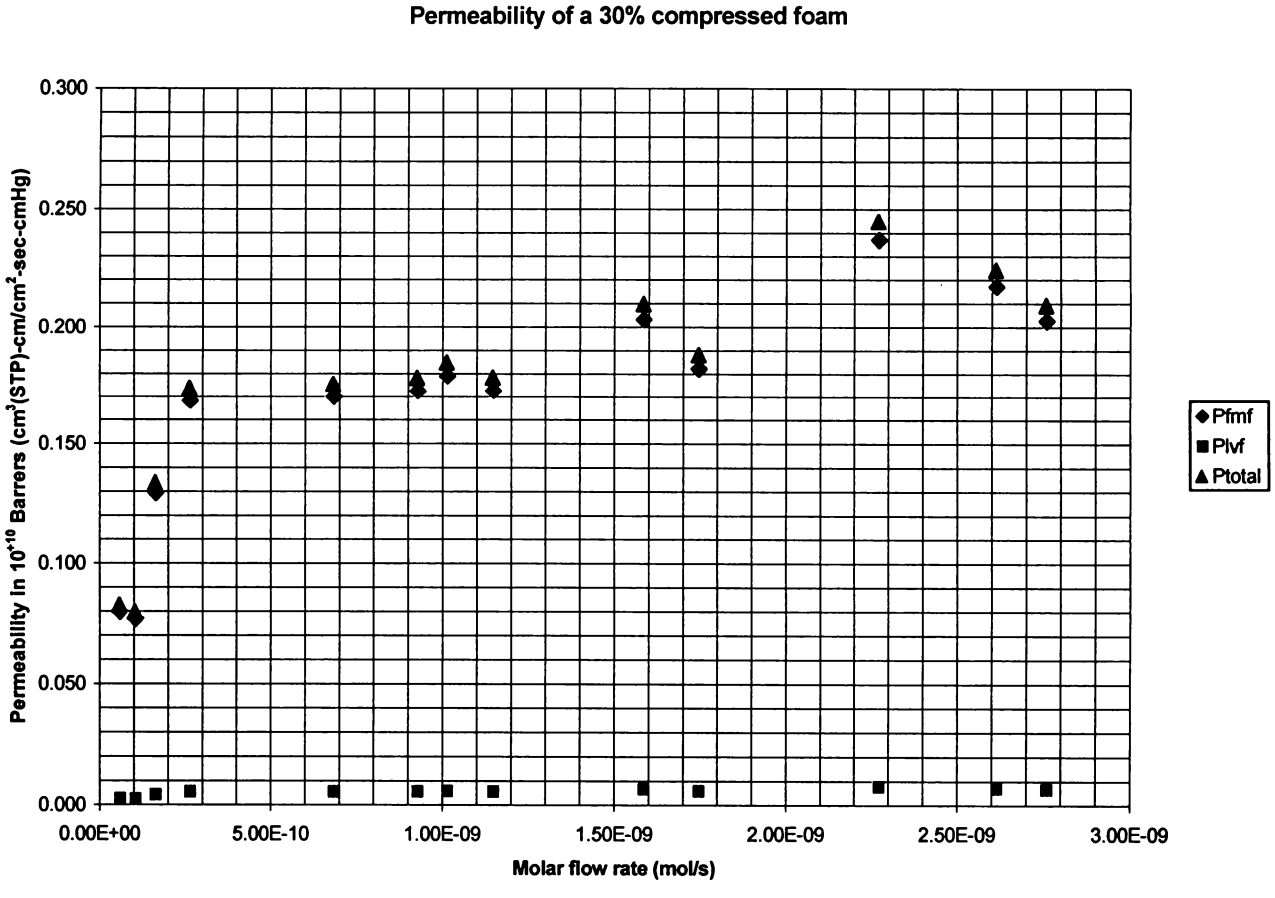

Figure 3.34. Permeability of a 30% compressed polysiloxane foam as a function of gas flow rate. Dominant flow regime is of the free molecular type.

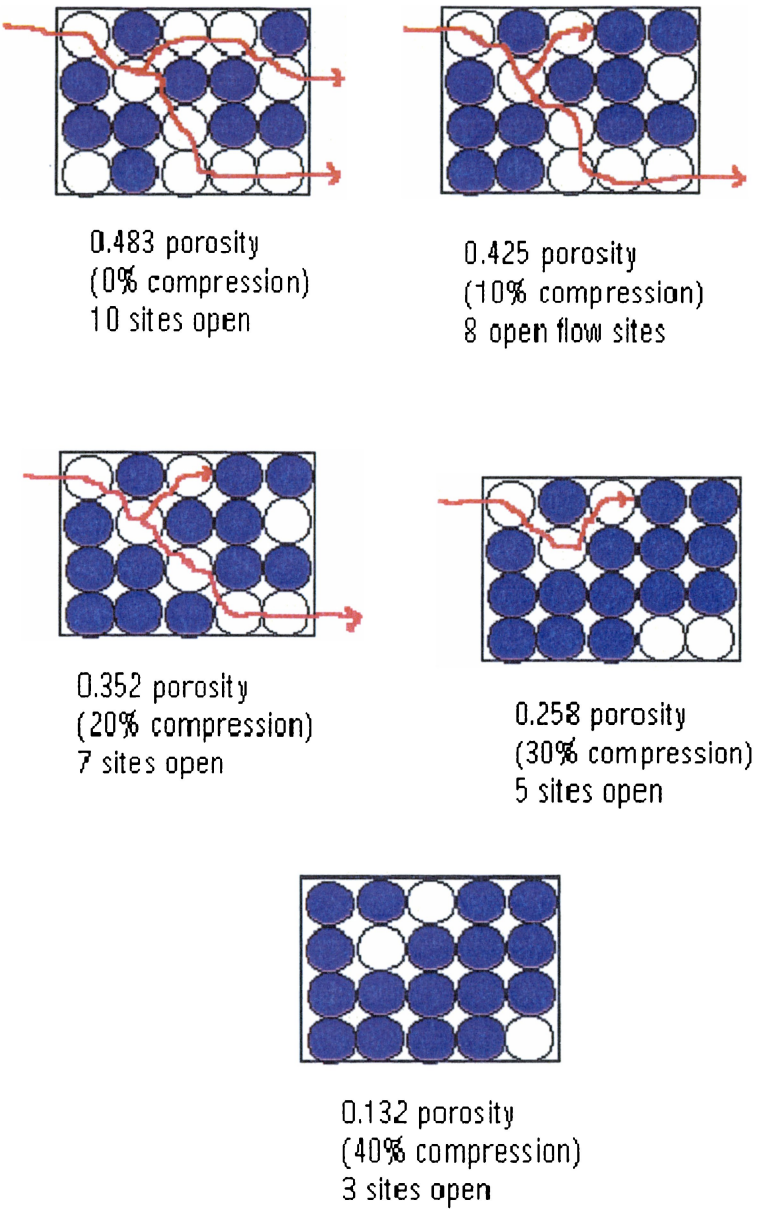

Figure 3.35. Example 20-site percolation model demonstrating the flow path changes as accessible sites are obstructed by foam compression.

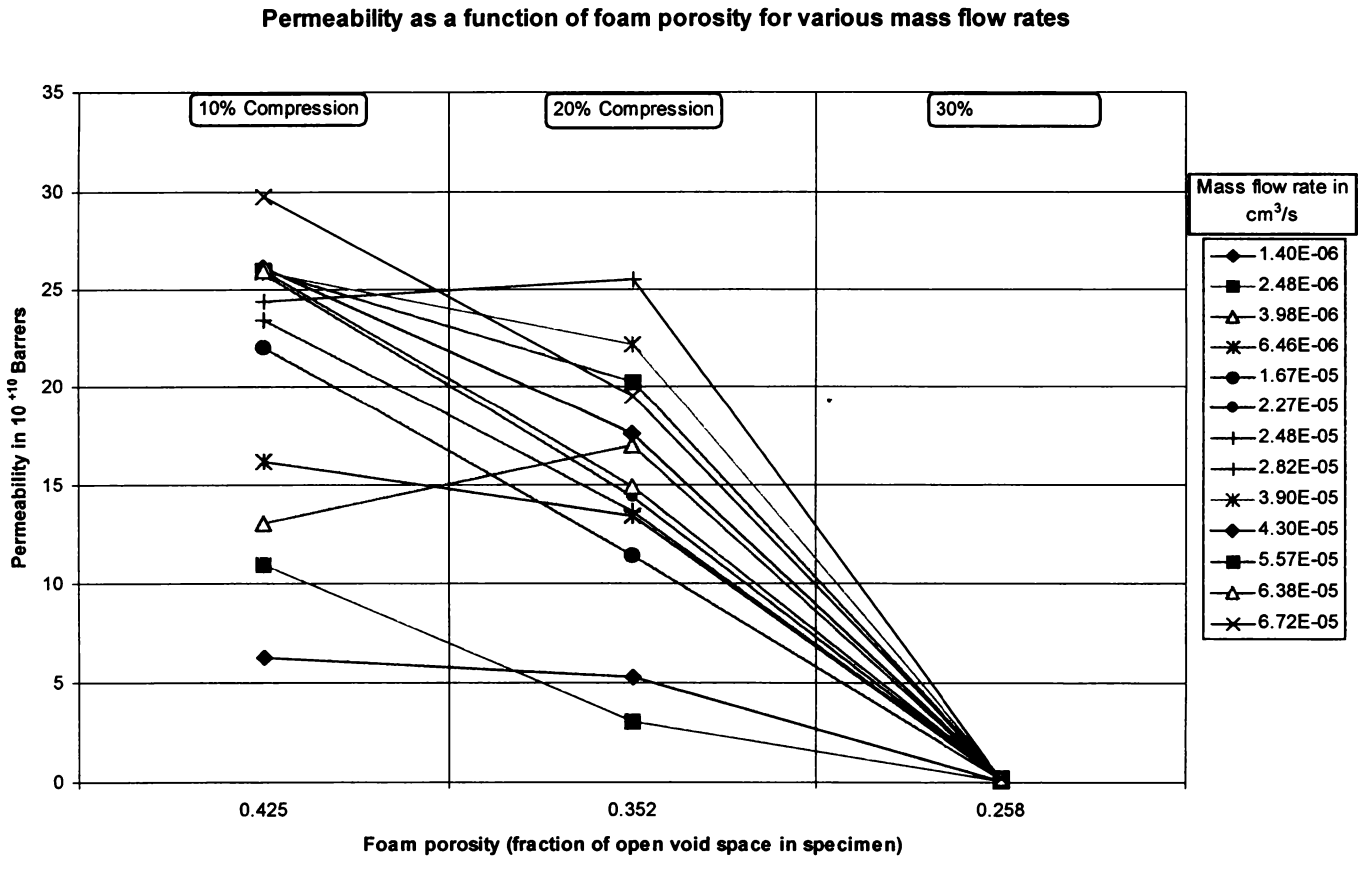

Figure 3.36. Permeability as foam is compressed, reducing void space available for gas flow. Percolation behavior is indicated, as well as a critical threshold void volume below which flow through specimen is obstructed.

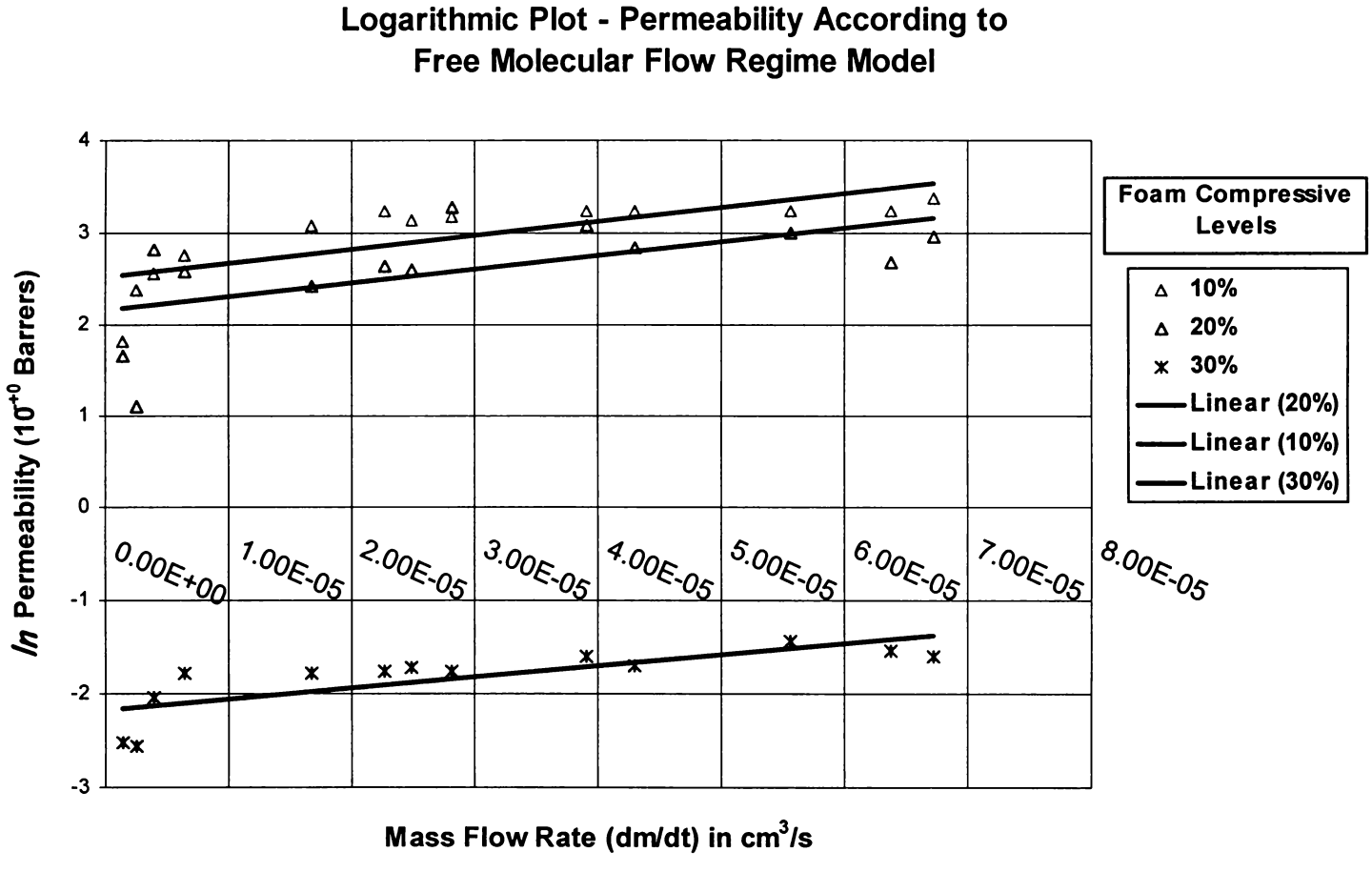

Figure 3.37. Logarithmic plot of permeability vs. mass flow rate, for three foam compressions. The 30% compressed foam shows a dramatic reduction in permeability.

Side view of 20% compressed foam

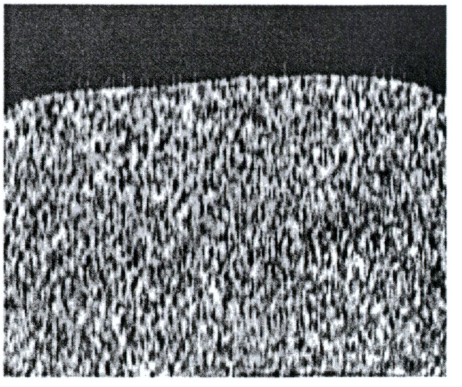

Side view of 40% compressed foam

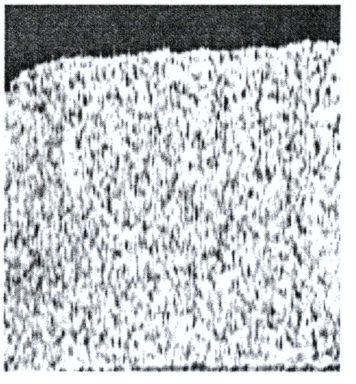

Side view of 60% compressed foam

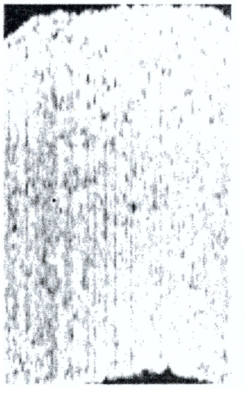

Figure 3.38. Side view of tomography stacks of image slices for various polysiloxane foam compressions. Deformation of voids can be observed as compression is increased. The total specimen length decreases as sample is loaded in the compressive direction (horizontal to the images).

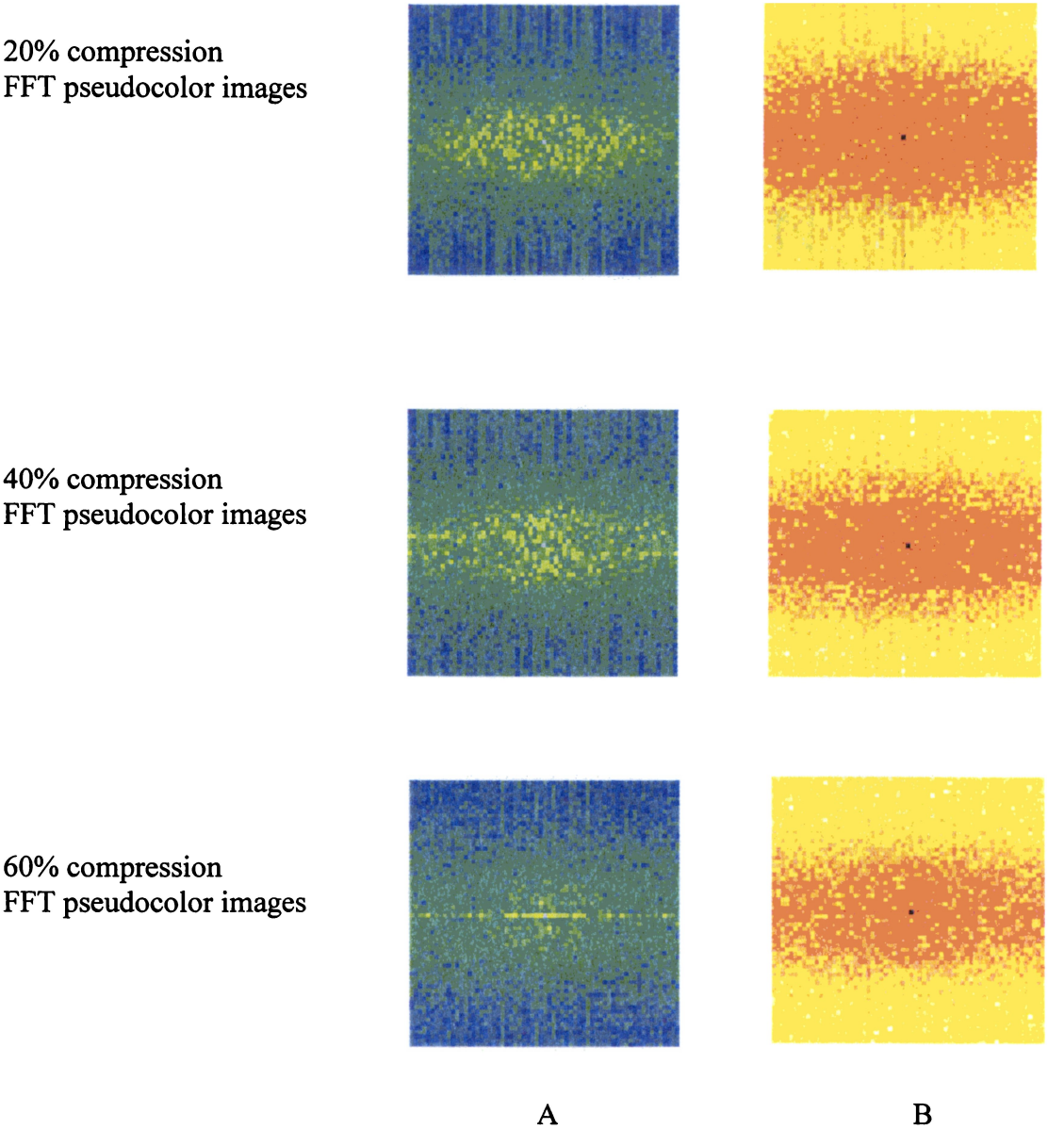

Figure 3.39. Fast Fourier Transform images of specimen side views using the Scion Image program A) 20-color palette and B) Fire-1 palette.

Appendix B: Tables

Table 2.1. Permeability Data for Hydrogen and Nitrogen Gases Through Filled Silicone Polymer. P expressed in cm^3 (STP) cm/cm^2 x s x Pa; S expressed in cm^3/cm^3 x Pa; D expressed in cm^2/s. *Source: Pauly, S. Permeability and Diffusion Data, in Polymer Handbook, 3rd Edition, Ed. Brandrup, J., Immergut, E. H., Wiley (New York), 1989.*

Permeant:	H_2			N_2		
	D	S	P	D	S	P
PDMS	$4.7x10^{-6}$	$7.3x10^{-5}$	$3.5x10^{-11}$	$8.5x10^{-6}$	$2.0x10^{-6}$	$1.7x10^{-11}$

Table 3.1. Average grayscale data expressed in CT numbers at distances across the specimen length, and as compression occurs. Initial specimen length was 1.5 inches.

	Location within Specimen Length					Avg
Level of Compression	**10%**	**25%**	**50%**	**75%**	**90%**	
0%	472.5560938	536.375938	507.4473438	486.0132	481.1003125	496.6986
10%	624.3491406	609.462031	590.1263281	494.2132	470.0132031	557.6328
20%	571.4813281	634.459297	701.464375	701.9291	651.4527344	652.1574
30%	811.6425	841.378281	853.2873438	811.0061	710.1775781	805.4984
40%	923.9655469	943.456797	1008.630551	993.0676	985.8633594	970.9968
50%	1137.154844	1149.20719	1148.063594	1137.395	1126.802266	1139.725
60%	1197.263672	1149.20719	1207.081016	1211.671	1212.409453	1195.526

Compression direction ⇒

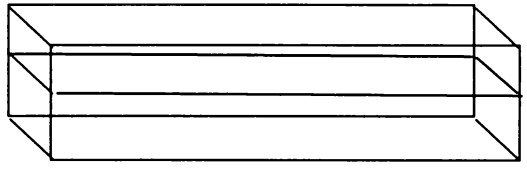

Specimen of length 1.5 inches inside of acrylic holder.

Table 3.2 Specimen dimensions at uniaxial compressive states, C, for tomographic test specimen.

C	Shim Length		Specimen Length		Specimen Width		Specimen Height		Specimen Volume		Specimen Density		Porosity
	in	cm	in	cm	in	cm	in	cm	in^3	cm^3	lb/in^3	g/cm^3	
0%	0	0	1.50	3.81	0.5	1.27	0.307	0.871	0.257	4.215	0.022	0.615	0.575
10%	0.15	0.38	1.35	3.43	0.5	1.27	0.353	0.897	0.238	3.906	0.024	0.664	0.526
20%	0.30	0.76	1.20	3.05	0.5	1.27	0.375	0.953	0.225	3.689	0.025	0.703	0.487
30%	0.45	1.14	1.05	2.67	0.5	1.27	0.386	0.980	0.203	3.319	0.028	0.781	0.409
40%	0.60	1.52	0.90	2.29	0.5	1.27	0.396	1.01	0.178	2.921	0.032	0.887	0.303
50%	0.75	1.91	0.75	1.91	0.5	1.27	0.407	1.03	0.153	2.502	0.037	1.036	0.154
60%	0.90	2.29	0.60	1.52	0.5	1.27	0.473	1.20	0.142	2.325	0.040	1.115	0.075

Table 3.3. Data summary for polysiloxane foam as a function of compression.

Level of Compression	Foam Density ρ^*	Porosity	Relative density ρ^*/ρ	X-ray Attenuation Coefficient @ 22keV μ/ρ_{avg} (cm^2/g)
0%	0.615	0.483	0.517	0.8807
10%	0.664	0.442	0.558	0.9160
20%	0.703	0.410	0.591	0.9723
30%	0.781	0.344	0.656	1.0622
40%	0.887	0.254	0.745	1.1597
50%	1.036	0.130	0.871	1.2588
60%	1.115	0.063	0.937	1.2974
Resin	ρ = 1.19	0	1.000	1.769

Table 3.4. Mechanical properties of polysiloxane foam of 48% porosity.

ε_z	φ or ρ^*/ρ	C	E_f (psi)	$\Psi(\varepsilon)$	σ (psi)	area (in^2)	F (lb)
0	0.517	0.277	76.074	0.831	0.000	0.154	0.000
0.1	0.558	0.318	87.468	0.849	7.429	0.177	1.311
0.2	0.591	0.354	97.310	0.863	16.797	0.188	3.149
0.3	0.656	0.431	118.508	0.889	31.594	0.193	6.098
0.4	0.745	0.551	151.609	0.921	55.845	0.198	11.057
0.5	0.871	0.753	207.048	0.962	99.597	0.204	20.268
0.6	0.937	0.874	240.344	0.982	141.603	0.237	33.489

Table 3.5. Summary of flow experiment results for 0%, 10%, 15%, 20%, 25%, and 30% foam compressions and mass flow rate of 3.9×10^{-5} cm^3.

		Initial specimen height h:	0.0394 in (1.0 mm)				
Compression	0	10	15	20	25	30	35
Porosity	0.4832	0.4424	0.426	0.4096	0.3768	0.344	0.299
Actual %compression	0.00%	10.16%	15.24%	20.32%	25.40%	30.48%	35.56%
Shims (in)	0	0.004	0.006	0.008	0.01	0.012	0.014
Actual porosity n_1	.483	.425	.389	.352	.305	.258	.195
Avg. Temp °C	26.9824	27.3661	26.9935	26.5472	27.0571	24.6444	23.2
Avg. Temp K	299.982	300.366	299.993	299.547	300.057	297.644	296.2
Data Collection Rate (sec)	1	1	5	5	5	15	30
Data Collection Rate (min)	0.01667	0.01667	0.08333	0.08333	0.08333	0.25	0.5
Δp_{ss} (Torr)	**-0.03254**	**0.0227**	**0.0358**	**0.0786**	**0.646**	**7.14**	**>118**
Time to steady-state (sec)	0	300	776	4301	10836	85501	259200
Time to steady-state (min)	0	5	12.9333	71.6833	180.6	1425.02	4320
Time used for initial count	181	192	251	626	3251	11086	
Δp of initial count (Torr)	-0.029	0.0203	0.03	0.061	0.51302	5.7192	
Eqn of initial line (where x = time in sec and y = Δp)	NA - need new data	9E-05x + 0.0112	0.0004x + 0.0112	0.0005x + 0.009	0.0009x + 0.0872	0.0028x + 0.832	
	$R^2 = 0.8276$	$R^2 = 0.9855$	$R^2 = 0.9633$	$R^2 = 0.9617$	$R^2 = 0.954$	$R^2 = 0.9618$	
Polynomial fit eqn (where x = time in sec and y = Δp)	NA - need new data	$-4E-07x^2$ + 0.0001x + 0.0108	$-6E-06x^2$ + 0.0007x + 0.0084	-3E-06x2 + 0.0008x + 0.0013	-1E-06x2 + 0.0016x + 0.0177	-1E-06x2 + 0.0049x + 0.1311	
	$R^2 = 0.8872$	$R^2 = 0.9959$	$R^2 = 0.9997$	$R^2 = 0.9994$	$R^2 = 0.9989$	$R^2 = 0.9994$	greater than
80% of $\Delta p_{steady-state}$	**-0.02603**	**0.01816**	**0.02864**	**0.06288**	**0.5168**	**5.712**	**94.4**
time (sec) at 80% Δp_{s-s}	31	83	206	671	3266	29521	
	p_{out} at steady-state	-0.03215	-0.07169	-0.08702	-0.64985	-7.0916	0

Table 3.6. Data summary for 10% foam compression tests.

	Master Data Sheet - 10% Compression Data				R_{atm} =	0.082057	lit-atm/°K-mol
	Excel		Volumetric	Molar	Leak		
	Filename	Avg. T	flow rate	flow rate	M-No(s).	P_{in} zero	Plot range
			cm^3/s	mol/s			Line #
1	10%m799	298.39	1.42E-06	5.799E-11	116799	0.005381	2 - 2431
2	10%m846	300.75	2.48E-06	1.005E-10	116846	0.004542	2 - 466
3	10%m847	299.66	3.98E-06	1.619E-10	116847	0.0051	2 - 455
4	10846847	301.67	6.46E-06	2.627E-10	116846+116847	0.005376	2 - 498
5	10%m823	302.54	1.67E-05	6.746E-10	116823	0.004823	2 - 565
6	10%r041	298.09	2.27E-05	9.144E-10	248041	0.005935	2 - 437
7	10%m845	301.79	2.48E-05	1.001E-09	116845	0.005925	2 - 303
8	10%m824	298.56	2.82E-05	1.151E-09	116824	0.007313	2 - 244
9	10%m797	301.93	3.90E-05	1.574E-09	116797	0.006478	2 - 515
10	10797847	299.74	4.30E-05	1.748E-09	116797+116847	0.007036	2 - 416
11	10797823	302.16	5.57E-05	2.246E-09	116797+116823	0.007307	2 - 548
12	1R797845	302.06	6.38E-05	2.574E-09	116797+116845	0.008143	2 - 533
13	10797824	298.67	6.72E-05	2.742E-09	116797+116824	0.009243	2 - 443
				Approx.		*Approx.*	
	Steady-state range	$t_{steady-state}$	t_{end}	$\Delta p_{steady-state}$	Δp_{avg}	$p_{insteady-state}$	p_{inavg}
	Line #	sec	sec	Torr	Torr	Torr	Torr
1	57 - 2431	296	12166	0.0037	0.0037	0.0057	0.0058
2	49 - 466	271	2,356	0.0037	0.0037	0.0058	0.0058
3	57 - 455	326	2,316	0.0050	0.0049	0.0072	0.0072
4	63 - 498	341	2,516	0.0065	0.0065	0.0090	0.0091
5	78 - 565	406	2836	0.0123	0.0120	0.0150	0.0149
6	62 - 437	341	2,216	0.0145	0.0140	0.0190	0.0185
7	78 - 303	391	1,506	0.0172	0.0098	0.0230	0.0131
8	80 - 244	456	1,276	0.0190	0.0180	0.0222	0.0213
9	92 - 461	461	2,571	0.0245	0.0240	0.0287	0.0280
10	97 - 515	516	2,111	0.0270	0.0261	0.0311	0.0303
11	106 - 548	546	2,756	0.0349	0.0338	0.0390	0.0381
12	101 - 533	511	2,671	0.0400	0.0388	0.0450	0.0440
13	87 - 443	481	2,261	0.0370	0.0365	0.0460	0.0450

Table 3.7. Data summary for 20% foam compression tests.

	Master Data Sheet - 20% Compression Data				R_{atm} =	0.082057	lit-atm/°K-mol
	Excel		Vol. flow	Molar flow	Leak		Plot range
	Filename	Avg. T	rate, cm^3/s	rate, mol/s	M-No(s).	P_{in} zero	Line #
1	20%m799	300.52	1.42E-06	5.758E-11	116799	0.015409	2 - 1526
2	20%m846	299.67	2.48E-06	1.009E-10	116846	0.015409	2 - 1654
3	20%m847	300.01	3.98E-06	1.617E-10	116847	0.015391	2 - 3967
4	20846847	300.54	6.46E-06	2.619E-10	116846+116847	0.018159	2 - 1137
5	20%m823	301.20	1.67E-05	6.757E-10	116823	0.015391	2 - 1835
6	20%r041	300.07	2.27E-05	9.219E-10	248041	0.018159	2 - 11600
7	20%m845	301.63	2.27E-05	9.171E-10	248041	0.015409	2 - 7000
8	20%m824	298.28	2.48E-05	1.013E-09	116845	0.0154	2 - 2550
9	20%m797	300.45	2.82E-05	1.144E-09	116824	0.0096662	2 - 1628
10	20797847	299.27	3.90E-05	1.588E-09	116797	0.015409	2 - 7090
11	20797823	299.53	4.30E-05	1.749E-09	116797+116847	0.00165	2 - 7000
12	20797845	301.37	5.57E-05	2.252E-09	116797+116823	0.009867	2 - 3273
13	20797824	299.26	6.38E-05	2.598E-09	116797+116845	0.0181594	2 - 8026
	Steady-state.	$t_{steady-state}$	t_{end}	$\Delta p_{steady-state}$	Δp_{avg}	$p_{insteady-state}$	p_{inavg}
	range line #	sec	sec	Torr	Torr	Torr	Torr
1	88 - 1526	451	7641	0.0050	0.005	0.002	0.001
2	100 - 1654	500	8,276	---	0.014	0.002	-0.001
3	292 - 3967	1,461	19,836	0.0039	0.002	0.004	0.004
4	128 - 1137	641	5,686	0.0082	0.026	0.013	0.008
5	171 - 1835	926	9246	0.0250	0.017	0.031	0.014
6	422 - 11600	2,126	58,016	0.0270	0.023	0.025	0.043
7	340 - 7000	3,216	35,016	0.0310	0.032	0.047	0.047
8	187 - 2550	981	12,796	0.0180	0.016	0.048	0.048
9	330 - 1628	1,366	37,871	0.0300	0.029	0.072	0.072
10	260 - 7090	1,291	35,441	0.0420	0.031	0.079	0.077
11	326 - 7000	1,636	35,006	0.0470	0.047	0.104	0.105
12	306 - 3273	1,526	16,356	0.0730	0.072	0.117	0.035
13	2 - 1521	1,521	40,156	0.0590	0.059	0.125	0.127
	$\Delta p_{steady-state}$	$p_{insteady-state}$		Temp. correlation value			
1	0.020	0.034					
2	0.024	0.046					
3	0.933	-0.023					
4	0.049	-0.006					
5	0.103	0.025					
6	0.900	0.040					
7	-0.121	-0.049					
8	0.368	0.026					
9	0.894	0.196					
10	0.925	0.317					
11	0.919	0.327					
12	0.233	0.026					
13	0.965	0.544					

Table 3.8. Data summary for 30% foam compression tests.

	Master Data Sheet - 30% Compression Data				R_{atm} =	0.082057	lit-atm/°K-mol
	Excel	Avg. T	Vol. Flow	Molar flow	Leak	P_{in} zero	Plot range
	Filename		rate, cm^3/s	rate, mol/s	M-No(s).		Line #
1	31%m799	299.58	1.42E-06	5.776E-11	116799	0.010073	2 - 1078
2	31%m116	293.45	2.48E-06	1.030E-10	116846	0.01028	2 - 190
3	31%m847	300.48	3.98E-06	1.614E-10	116847	0.0094547	2 - 2980
4	31846847	300.22	6.46E-06	2.622E-10	116846+116847	0.292313	2 - 3859
5	31%m823	298.55	1.67E-05	6.817E-10	116823	0.0100772	2 - 1065
6	31%r041	298.73	2.27E-05	9.260E-10	248041	0.0010077	2 - 1402
7	31%m248	295.60	2.27E-05	9.358E-10	248041	0.0104966	2 - 1065
8	31%m845	298.78	2.48E-05	1.012E-09	116845	0.0098739	2 - 4140
9	31%m824	299.85	2.82E-05	1.146E-09	116824	0.009455	2 - 1166
10	31%m797	300.06	3.90E-05	1.584E-09	116797	0.009861	2 - 2673
11	31797847	298.98	4.30E-05	1.753E-09	116797+116847	0.0098696	2 - 3976
12	31797823	297.65	5.57E-05	2.281E-09	116797+116823	0.0100815	2 - 2869
13	3R797845	296.99	6.38E-05	2.618E-09	116797+116845	0.347611	2 - 1427
14	31797824	295.80	6.72E-05	2.769E-09	116797+116824	0.34763	2 - 3276
	Steady-st.	$t_{steady-state}$	t_{end}	$\Delta p_{steady-state}$	Δp_{avg}	$p_{insteady-state}$	p_{inavg}
	range line #	sec	sec	Torr	Torr	Torr	Torr
1	538 - 1078	32,221	64621	0.310	0.286	0.220	0.176
2	108 - 190	6,541	11,341	0.600	0.581	0.460	0.452
3	735 - 2980	44,000	178,741	0.560	0.534	0.400	0.396
4	691 - 3859	41,401	231,481	0.740	0.693	0.660	0.605
5	597 - 1065	35,761	63841	1.800	1.581	1.700	1.539
6	651 - 1402	39,000	84,061	2.400	2.180	2.400	2.150
7	586 - 1065	35,000	63,841	2.150	1.890	2.200	1.903
8	835 - 4140	50,000	248,341	2.700	2.532	2.800	2.575
9	601 - 1166	36,000	69,901	2.980	2.830	2.980	2.823
10	735 - 2673	44,000	160,321	3.900	3.780	4.070	3.940
11	868 - 3976	52,000	238,501	4.300	4.125	4.520	1.298
12	936 - 2869	56,000	172,081	5.400	5.383	5.630	5.132
13	816 - 1427	49,000	85,561	6.110	5.271	6.450	5.591
14	723 - 3276	43,321	196,501	6.700	6.132	7.080	6.558

Table 3.8. - continued. Data summary for 30% foam compression tests.

	Master Data Sheet - 30% Compression Data				R_{atm} =	0.082057	lit-atm/°K-mol
	$\Delta p_{steady\text{-}state}$	$p_{insteady\text{-}state}$	Temp. correlation values				
1	-0.117	0.172					
2	0.280	0.453					
3	0.770	0.590					
4	0.665	0.709					
5	-0.340	0.060					
6	-0.329	-0.019					
7	0.761	0.499					
8	0.896	0.869					
9	0.220	0.055					
10	0.936	0.931					
11	0.835	0.823					

Table 3.9. Summary of Polysiloxane Foam Volumetric Quantities.

V o i d V o l u m e

Calculations

NOTES: 0.01 cm shim volume 0.118 cm^3 σ_{H2} (H_2 diam.) 2.83E-10 m

No. of voids per cm^3 2689 specimen mass 0.718 g

Com-pres-sion	Total Specimen Volume (cm^3)	Polymer Volume, incl. f_v (cm^3)	Poly-mer Vol. Frac-tion ϕ_m	Total Void Volume (cm^3)	Volume per Void (cm^3)	Void Diam. (cm)	Void Radius (cm)	Void Radius (mm)	p_{min} (Torr)	mean free path ℓ(m)	Knudsen Number ℓ/d	foam density g/cm^3	porosity or $V_{void}/V_{specimen}$	x20 sites
0	1.168	0.6039	0.517	0.56414	1.796E-04	0.0700	0.0350	0.3500	0.001	0.0871899	124.547	0.615	0.483	10
10	1.050	0.6039	0.575	0.44614	1.421E-04	0.0647	0.0324	0.3237	0.006	0.0152965	23.628	0.684	0.425	8
20	0.932	0.6039	0.648	0.32814	1.045E-04	0.0584	0.0292	0.2922	0.017	0.0051288	8.777	0.770	0.352	7
30	0.814	0.6039	0.742	0.21014	6.691E-05	0.0504	0.0252	0.2519	0.120	0.0007266	1.442	0.882	0.258	5
40	0.696	0.6039	0.868	0.09214	2.934E-05	0.0383	0.0191	0.1913	0.454	0.0001920	0.502	1.032	0.132	3
50	0.578	0.6039	1.045	0.00000	0.00E+00	0.0000	0.0000	0.0000	2.9	0.0000301		1.242	0.000	0

Constituents of the Polymer Resin:

$[(CH_3)_2SiO]_x$	0.42282	cm^3
SiO_2, 26 v%	0.10512	cm^3
free volume, v_f	0.07592	cm^3
Total	0.60386	cm^3

Appendix C: X-Ray Mass Attenuation Coefficients and Mass Energy-Absorption Coefficients for Elements Silicon, Oxygen, Carbon and Hydrogen

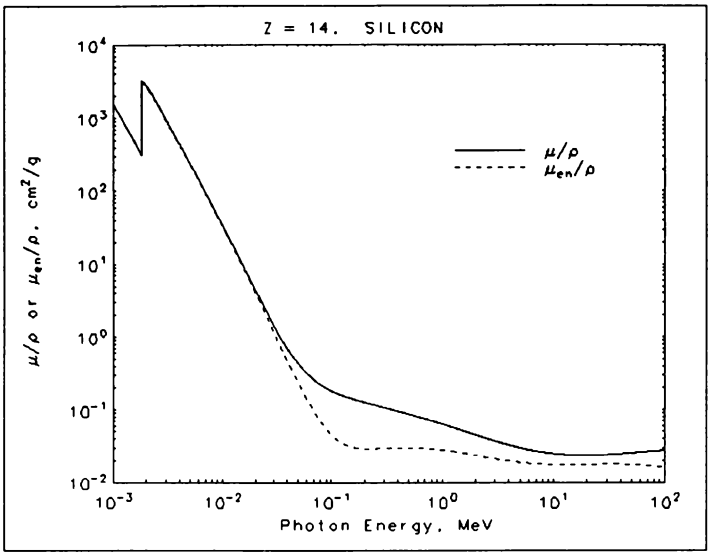
Z = 14. SILICON
μ/ρ
μen/ρ
μ/ρ or μen/ρ, cm²/g
Photon Energy, MeV

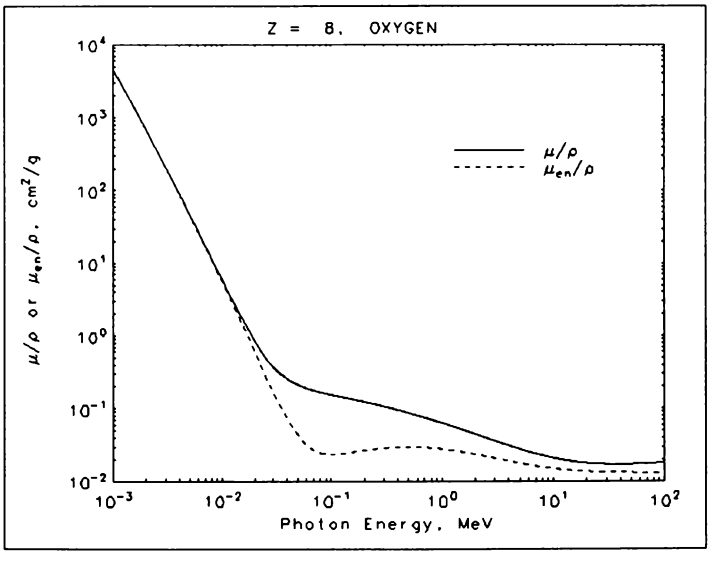
Z = 8. OXYGEN
μ/ρ
μen/ρ
μ/ρ or μen/ρ, cm²/g
Photon Energy, MeV

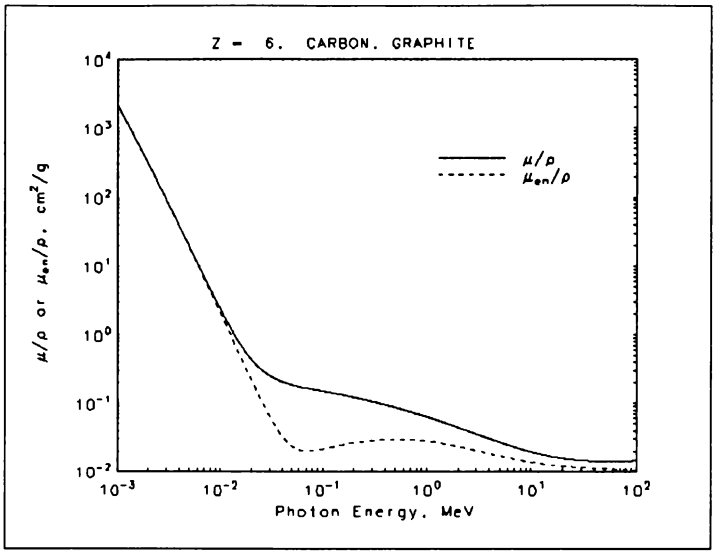
Z = 6. CARBON, GRAPHITE
μ/ρ
μen/ρ
μ/ρ or μen/ρ, cm²/g
Photon Energy, MeV

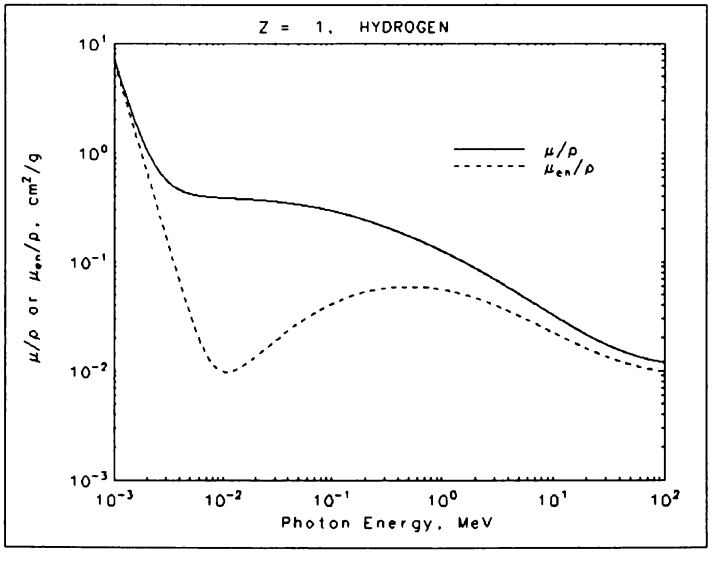
Z = 1. HYDROGEN
μ/ρ
μen/ρ
μ/ρ or μen/ρ, cm²/g
Photon Energy, MeV

Appendix D: Variable Descriptions in MATLAB and Program for Theoretical Gas Transport Properties

```
%Gas Transport Model - ALTERING pinT, poutT, and mdotTORR
%This program plots Dkeff, k1free, klv, Pfmf and Plvf as a function of delta p
("pdrop")for each compression
%path(path,'a:')

%TO determine k1free (effective permeability for free mol. flow under compression)
%TO determine klv (permeability for laminar viscous flow under compression)
%TO determine "chemical permeability" in fmf and lvf regimes

%MEASURE pin, pout, and mass flow rate
%OBTAIN value for mass flow rate in kg-atm/sec (using hydrogen density)
%CALCULATE Dkeff  -Eqn.B27
%Use Dkeff to determine k1free  -Eqn.B21

        p=1:7
        pcomp(p)=[.1; .2; .3; .4; .5; .6; .625]  %percent compression


rin=.0935               %inside hole radius (in.)
rout=.7625              %specimen diameter (in.)
%ratio=rin/rout
ratio=rout/rin

mdotVOL=3.9e-005        %mass flow rate (cc-atm/sec)
mdot=mdotVOL/1000%mass flow rate (lit-atm/sec)
%mdotTORR=1.40e-003     %mass flow rate (Torr-lit/sec)
%mdot=mdotTORR/760      %mass flow rate (lit-atm/sec)

Hrho=.081797            %hydrogen density at 298K (g/lit)
mdotm=mdot*Hrho/1000    %mass flow rate (kg/sec) [see PV calculations]

pinT=.005               %gas pressure going in (torr)

        n=linspace(1,10,1000)
         poutT=0.95*(pinT./n)

pin=pinT*133.322        %gas pressure going in (Pa)
pout=poutT*133.322      %gas pressure going out (Pa)
pdrop=pin-pout          %pressure drop across specimen radius (Pa) [recall
Pa=N/m2]

pdropT=pinT-poutT       %pressure drop across specimen radius (Torr)
```

```
pavg=pin+pdrop/2          %average pressure (Pa)
pavgT=pinT+pdropT/2       %average pressure (Torr)

R=8.31439                 %J/K-mol (same as kg-m2/(s2-K-mol))
T=298                     %degrees K
RT=(R*T*1000)/2           %RT product in m2/s2 since there are 2g/mol hydrogen
MW=.002                   %gas molecular weight in kg
mu=2.758e-6               %gas viscosity in kg/m-sec

%for p=pcomp
  hin=0.40*pcomp(p)       %specimen thickness (in.)
  h=hin*.0254             %specimen thickness in SI units (m)

for p=1:7
Dkeff=(mdotm*(log(ratio))*RT)./(pdrop.*2*pi*h(p));     %effective diffusivity (m2/s)
                                                       in fmf regime

figure(1)
plot(pdrop,Dkeff,'b-')
title('Effective Diffusivity (Dkeff) vs. Del p (pin-pout) Pa')
xlabel('pressure drop (Pa)'); ylabel('effective diffusivity, Dkeff (m2/s)')
grid
hold on

figure(2)
plot(pdropT,Dkeff,'b-')
title('Effective Diffusivity (Dkeff) vs. Del p (pin-pout) Torr')
xlabel('pressure drop (Torr)'); ylabel('effective diffusivity, Dkeff (m2/s)')
grid
hold on

tau=0.67                  %tortuosity
n0=0.60                   %initial porosity, i.e. no compression


n1=n0-(pcomp*n0)          %new porosity as compression occurs


k1free=(9*pi*Dkeff.^2)./(256*tau*RT*n1(p));     %effective permeability (m2)
                                                in fmf regime

k0=k1free.*((n0./n1(p)).^3).*((1-n1(p))./(1-n0)).^2;     %material permeability (m2)
                                                         in fmf regime
```

```
klv=(log(ratio)*mdotm*mu*RT)./((pdrop.*pavg.*2*pi*h(p)));      %permeability (m2)
                                                                in lvf regime

k0lv=klv.*((n0./n1(p)).^4).*((1-n1(p))./(1-n0)).^3;            %material permeability (m2)
                                                                in lvf regime


figure(3)
plot(pdrop,k1free,'b-')
title('Effective Permeability (k1free) vs. del P - Pa')
xlabel('pressure drop (pin - pout) (Pa)'); ylabel('effective permeability (m2)')
grid
hold on


figure(4)
plot(pdropT,k1free,'b-')
title('Effective Permeability (k1free) vs. del P - Torr')
xlabel('pressure drop (pin - pout) (Torr)'); ylabel('effective permeability (m2)')
grid
hold on

figure(5)
plot(pdrop,klv,'b-')
title('Effective Permeability (klv) vs. del P - Torr')
xlabel('pressure drop (pin - pout) (Torr)'); ylabel('effective permeability (m2)')
grid
hold on

figure(6)
plot(pdropT,klv,'b-')
title('Effective Permeability (klv) vs. del P - Torr')
xlabel('pressure drop (pin - pout) (Torr)'); ylabel('effective permeability (m2)')
grid
hold on

%Actual Permeability in cc(STP)-cm/cm2-sec-cmHg, or 10e+10 Barrers

Pfmf=sqrt((n0.*tau*k1free)./((1.0283e-11)*T*MW))        %"chemical" permeability in
fmf regime

Plvf=(klv.*pavg)./(T*mu*2.782e-5)          %"chemical" permeability in lvf regime
```

```
figure(7)
plot(pdropT,Pfmf,'b-')
title('Permeability (Free Molecular Flow) vs. del P - Torr')
xlabel('pressure drop (pin - pout) (Torr)'); ylabel('Permeability
(cc(STP)-cm/cm2-sec-cmHg)')
grid
hold on

figure(8)
plot(pdropT,Plvf,'b-')
title('Permeability (Laminar Viscous Flow) vs. del P - Torr')
xlabel('pressure drop (pin - pout) (Torr)'); ylabel('Permeability
(cc(STP)-cm/cm2-sec-cmHg)')
grid
hold on

        end             %pressure loop ended
            end             %compression loop ended
```

Appendix E: Procedure for Gas Flow Through Cellular Polymer Experiments

Schematic for Gas Flow through Cellular Polymer Experiments

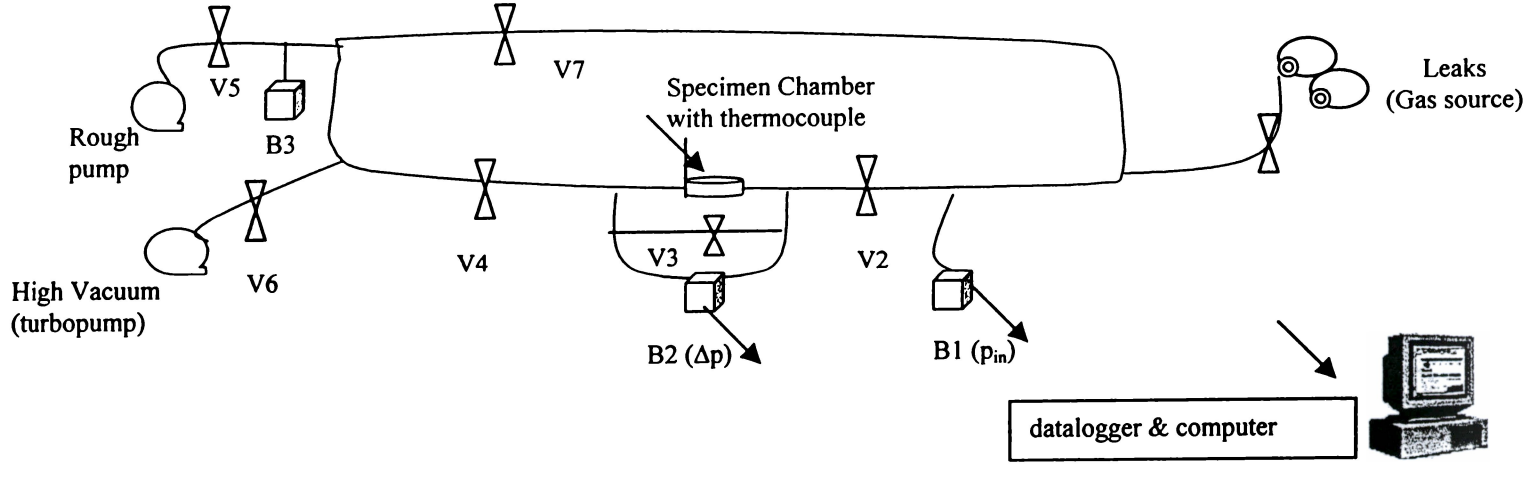

Procedure for Gas Flow through Cellular Polymer Experiments

1. Rough pump system. Close all valves; open V3 and V5 for initial pumpdown.
   Open V4 until $p_{pump} \cong 10^{-3}$ Torr; open V2, finally rough pumping the system down.

2. High vacuum system. Close V5; open V6.
   Pump down to $p_{HV} \cong 10^{-7}$ Torr.
   Indications: Baratrons B1 and B2 should show p_{in} and Δp of approximately 10^{-6} Torr.
   Close V3.

3. Pump off excess leak pressure. Close V2; open V1 and V7.
   Pump down calibrated leak until $P_{pump} = 10^{-3}$ Torr
   Close V7.

4. Start Hyperware program (see steps) to begin tracking data; next step will begin test.

5. Open V2

6. Measure time, temperature, p_{in}, Δp, and calculated p_{out} as programmed. ASIDE: Questions to be answered (once experiments are completed) are:
   A) How much time does it take for gas to go through the system?
   B) How does this time vary when specimen is in chamber?
   C) How does this time vary as compression on the specimens is increased?
   D) At steady-state, what are values of p_{in}, Δp, and p_{out}?
   E) What is result with a different incoming gas mass rate?
   F) Bottom line requirement: gas mass rate and specimen compression upon steady-state values of p_{in}, Δp, and p_{out}.

7. At end of test, close system. Close V1, V2, and V4. Open V3.

8. Change specimen set-up by removing specimen chamber. Disengage thermocouple; open bolts to system; open chamber bolts.

9. Place new specimen disk in chamber with appropriate number of shims to obtain desired level of compression (see table). Replace chamber bolts; replace specimen bolts. Mark used specimen with a number and reserve. Record number.

10. Rough system down (mainly specimen chamber and system across B2). Close V6; open V4 and V5; pump down to $p_{pump} \cong 10^{-3}$ Torr.

11. High vacuum system. Close V5; open V6. Pump down to $p_{HV} \cong 10^{-6}$ Torr. Open V2 and ensure that $p_{HV} \cong 10^{-6}$ Torr still; close V3.

12. Pump off excess pressure on leak. Close V2; open V1 and V7. Pump down to $p_{pump} \cong 10^{-3}$ Torr. Close V7.

13. Start Hyperware program (see steps) to begin tracking data; next step will begin test.

14. Open V2. Repeat from Step 6 above.

Note: Only if a few moments have passed after closing V7 shall V2 be opened, to minimize chance for leak excess pressure to rebuild.

Hyperware Collection and Storage of Data

NOTE: "Home" as written below designates the main menu of the Hyperware program picturing the Omega datalogger and a PC with a cable between them. The icon looks like a small datalogger.

Open Shortcut to Hyperlog program

Open Net
File
Open Program Net
Filename "loflo.net" (or appropriate *.net file); OK
Go back Home

Open Hypertrack Real-Time Display (will see 5 red probe icons)
Drag down disk
Drag down table
Doubleclick on disk
Give dataset to be collected a filename "whatever.xls"
Drag connectors from each probe to the disk
Drag connectors from each probe to the table
Save file under name "whatever.prb"
Go back Home

Doubleclick on connector between datalogger and PC icons
Connect; OK

Drag NET icon from PC to datalogger
OK to "Upload file to datalogger?"

Real-time data tracking is initiated by clicking on the Probe icon
Click on green flag

Start data collection by datalogger by clicking on the purple ENABLE

To stop real-time tracking of data, click on the red STOP sign

To stop datalogger from recording data, go Home. Click on the purple STOP
Click disconnect; OK.

Immediately open whatever.xls spreadsheet using Excel software and save file on a floppy disk to ensure data preservation.

VITA

Rosanne A. Smith is a staff member in the Technology Development division of the BWXT Y-12, L.L.C. Complex in Oak Ridge, Tennessee. She conducts applied research in the area of gas flow, diffusion, and permeation through polymeric materials. Ms. Smith is completing a Ph.D. in Polymer Engineering at the University of Tennessee, Knoxville.

Her education includes a B. S degree in chemistry from Howard University in Washington, D. C. and an M. S. degree in chemistry from the University of California, Irvine. Ms. Smith also holds an M. S. degree in materials engineering from George Washington University through its Joint Institute of Aeronautical Sciences at NASA/Langley Research Center in Virginia.

Ms. Smith has extensive project management experience in the areas of manufacturing, metrology, and assembly engineering. She has also managed training, quality assurance, and human resource functions.

Rosanne Smith was born and raised on the south side of Chicago, Illinois and now resides in Knoxville, Tennessee with her family. They include husband and two sons. She is current president of an investment club and is active in the Oak Ridge Alumnae Chapter of Delta Sigma Theta Sorority, Inc. and the Knoxville Chapter of Jack and Jill, Inc.